N° d'ordre : 40968

THÈSE

UNIVERSITE DES SCIENCES ET TECHNOLOGIES DE LILLE
ECOLE DOCTORALE SCIENCES POUR L'INGENIEUR

pour obtenir le titre de

DOCTEUR DE L'UNIVERSITE
Spécialité: Micro et nano technologies,
Acoustique et Télécommunication

par

Sergio Ivan CARRILLO GUERRERO

Electronic structure and optical properties of heterogeneous nanocrystals: theory and modeling

Structure électronique et propriétés optiques de nanocristaux hétérogènes: théorie et modélisation

Thèse dirigée par **C. DELERUE**

Soutenue le 11 Décembre 2012 devant la commision d'examen.

Membres du jury:

L. MAGAUD	Rapporteur
B. MASENELLI	Rapporteur
F. CLERI	Examinateur
F. MICHELINI	Examinateur

Abstract

The main objective of this work is to give a description of the electronic structure and optical properties of semiconductor quantum dots (nanocrystals) containing heterojunctions, i.e. nano-junctions between two semiconductors. These nanostructures have interesting optical properties which are very promising for applications in photonics and photovoltaics. The theoretical description of the effects of the interface demands special attention. We start describing the calculations of the electronic structure of bulk semiconductors using semi-empirical tight-binding, and we show how to apply this technique to semiconductor quantum dots. We develop expressions to connect the discrete levels of energy in a quantum dot and the transitions in optical absorption spectra. The bulk tight-binding parameters are used for the calculation of the electronic structure of quantum dots of single compounds, analyzing the effect of the size variation of the quantum dots. The effectiveness of this method is demonstrated, in particular we obtain good values for the bandgap versus size compared to experiments. We apply this method to calculate the electronic structure of PbSe/CdSe core/shell quantum dots, after an analysis of the different types of interfaces that can appear in this system, and we discuss the issues related to the determination of the band offsets. The results of these calculations validate the assumption of the role of the shell as a potential barrier for the electron and the hole. The electronic structures are used in the last chapter to simulate the absorption spectra of PbSe, CdSe and PbSe/CdSe quantum dots. We give theoretical support to recent experiments in transient absorption spectroscopy, revealing groups of new transitions originated by photo-induced intraband absorption. Our calculations shed light on the nature of these optical transitions which can be of interest for applications in photonics.

Keywords : Semiconductor nanocrystals - Optical properties, Quantum dots, Electronic structure, Heterojunctions, Excitons, Selenides, Photonics.

Résumé

L'objectif de ce travail est de décrire la structure électronique et les propriétés optiques de botes quantiques de semiconducteurs (nanocristaux) contenant des hétéro-jonctions, c'est-à-dire des nano-jonctions entre deux semiconducteurs. Ces nanostructures ont des propriétés optiques très intéressantes pour les applications photoniques et photovoltaïques. La description théorique des effets liés à l'interface demande un traitement particulier. Nous commenons par décrire la structure électronique des semiconducteurs massifs en liaisons fortes et nous montrons comment on peut appliquer cette théorie aux nanocristaux. La méthodologie de calcul des spectres optiques en partant de la structure électronique est présentée. Les paramètres de liaisons fortes sont utilisés pour calculer l'évolution de la structure électronique des botes quantiques en fonction de leur taille. Le bon accord théorie/expérience obtenu pour la variation de la bande interdite en fonction de la taille valide notre approche théorique. Nous appliquons ensuite ces techniques à des nanocristaux coeur/coquille PbSe/CdSe, après analyse des interfaces présentes dans ces systèmes et discussion des valeurs des discontinuités de bandes. Nos calculs justifient l'hypothèse que CdSe agit comme une barrière de potentiel pour l'électron et le trou. Nous simulons les spectres d'absorption optique des nanocristaux de PbSe, CdSe et PbSe/CdSe. Nos travaux confirment l'existence de transitions optiques intra-bandes photo-induites observées récemment dans des expériences de type pompe-sonde. Ces transitions intra-bandes photo-induites, révélées et étudiées pour la première fois, sont très intéressantes pour des applications en photonique.

Mots-clés : Nanocristaux semiconducteurs – Propriétés optiques, Points quantiques, Structure électronique, Hétérojonctions, Excitons, Séléniures, Photonique.

Acknowledgements

This thesis makes part of the EU Seventh Framework Program Herodot, which gave financial support in its entirety. I would like to acknowledge also the financial support from the *Université Catholique de Lille* during the last months.

The development of this work took place at the *Institute d'Electronique de microeléctronique et de Nanotechnologie* (IEMN) and its department ISEN, within the Electronic Structure team, coordinated by Monsieur Christophe DELERUE. I express my most sincere gratitude to him for accepting me as part of the team as well as for his labor as thesis director. His knowledge, patience and permanent availability made possible this work. He gave me also the opportunity to work with the *TB_Sim* platform, which has behind the astonishing work of Monsieur Yann Michel NIQUET from the CEA in Grenoble.

I also thank all the members of the jury for the great interest about this work. Madame Laurence MAGAUD and Monsieur Bruno MASENELLI, for accepting to be the rapporteurs. The examiners, Madame Fabienne MICHELINI and Monsieur Fabrizio CLERI, to whom I also thank for presiding the jury.

I would like to thank also Monsieur Ludger WIRTZ, who was determinant at the beginning of this work as co-director, and helped me to get into the topic. I appreciate the exchange with Monsieur Bruno GRANDIDIER and my colleague as PhD student Than-Hai NGUYEN, which made also part of the project Herodot. From other nodes of the network, I also thank the collaboration and exchange with Monsieur Zeger HENS and his PhD student Bram DE GEYTER, from *Ghent University/IMEC* in Belgium, as well as with Monsieur Arjan HOUTEPEN and his work team from *Delft University* in the Netherlands.

There are people inside the physics group that made this time in Lille still better: Florence, Isabelle, Didier, Alejandro, Efterpi, Jing, Arnaud.

Thanks also to my friends in the distance or not so far, and finally, but no less important, my family and specially my parents, always there reminding me that there was just distance that separated us.

Contents

Introduction

The development of nanomaterials suitable for applications in photonics represents one of the most promising research topics due to its current and possible future impact in the technological progress. For example, colloidal nanocrystals of direct-gap semiconductors (III-V or II-VI) integrated on silicon technology could be very useful to overcome well-known limitations of Si in photonics due to its indirect gap. Semiconductor nanocrystals are also intensively studied for applications in photovoltaics because they could provide easily tunable and processable materials [1, 2].

The European ITN project Herodot (Heterogeneous quantum rod and quantum dot nanomaterials) in which I was involved was a collective effort to study the electro-optical properties of heterostructures based on colloidal quantum dots. An important variety of nanocrystals made from II-VI (Zn and Cd chalcogenides), IV-VI (Pb chalcogenides) and III-V (InP, InAs) semiconductor compounds can be prepared by bottom-up chemical synthesis, usually in the form of suspensions. Using these methods, it is possible to control quite accurately the shape and the surface chemistry of the particles [3]. The electrons, holes and excitons undergo strong confinement in the usual size ranges for these nanocrystals, with diameters for spherical shapes between 1 and 10 nm. The electronic structure of the nanocrystals is then described by discrete levels, with a size-dependent optical gap which can be significantly larger than the one for the bulk compound. The nanocrystals then act as quantum dots for the electrons. The typical size dependence of the energy levels is illustrated in Fig. 1 which also shows that suspensions of CdSe quantum dots under UV excitation emit light from the blue to the red for diameters varying from 2 to 6 nm. A general introduction to the effects of quantum confinement on semiconductor nanocrystals is presented in Chapter 1.

The hetero-nanocrystals which have motivated this work are colloidal particles composed of

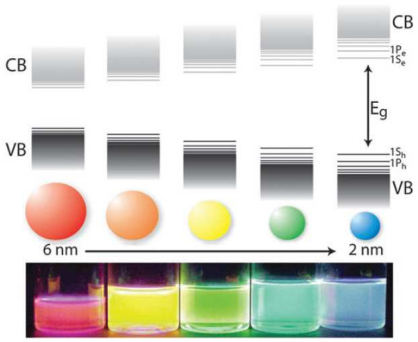

Figure 1: Representation of the quantum confinement effect on the energy level structure of a semiconductor material. The lower panel shows colloidal suspensions of CdSe nanocrystals of different sizes under UV excitation.[3].

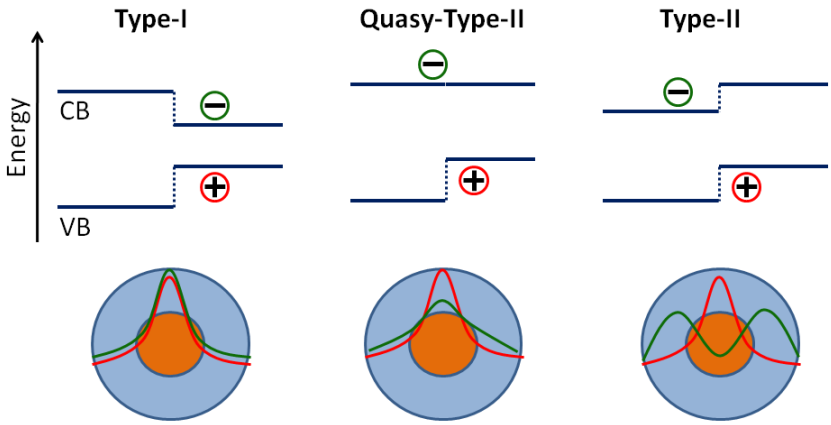

Figure 2: Band alignments at heterojunctions. The type-I corresponds to the case where the electron (-) and the hole (+) are confined in the same region, for this case, the core which has the narrowest gap (in the three schemes the core is on the right). In the type-II the staggered band alignment results in the spatial separation of the electron and the hole. The quasi-type-II shows the localization of only one of the carriers in one component (in this case the hole in the core) and the delocalization of the other carrier.

two types of semiconductor compounds. An example is the passivation of the surface of colloidal nanocrystals with a shell of a second compound, often with a higher bandgap. These hetero-nanocrystals are usually synthesized starting from a suspension of semiconductor nanocrystals, the cores, then adding precursors for the second semiconductor to grow the shell. Core/shell nanocrystals can have spherical or more complex shapes depending on the materials and the preparation conditions. A brief presentation of these nanocrystals and the methods of synthesis is given in Chapter 3.

At the interfaces in hetero-nano-structures, the electronic structure exhibits some discontinuity. In the case of core/shell nanocrystals, depending on the difference between the bulk bandgaps, there are essentially three possible band-alignments, illustrated in Fig. 2. In the type-I alignment, the electron and the hole are confined together in the same part of the hetero-nanocrystal creating a direct exciton. The most common situation is when the confinement occurs in the core, as the carriers are protected from interaction with the surface and the environment. The type-II is characterized by a spatial separation of the electron and the hole in different sides of the heterojunction, which is described as a spatially indirect exciton. In the last case (displayed in the center of Fig. 2), the quasi-type-II, one carrier is confined in one of the components, while the other one is delocalized over the whole nanocrystal.

In this thesis, we have studied the electronic structure and the optical properties of nanocrystals either made from a single compound or containing a nano-heterojunction. We start introducing in the Chapter 1 the selected methods for the calculation of the electronic structure and optical properties of quantum dots (hereafter, the terms “quantum dots” and “nanocrystals” will be used indistinctly). We present some results on the bulk band structure, in particular to justify the choice of our methodologies.

Calculations of the electronic structure of quantum dots of individual compounds are presented in Chapter 2. We evaluate the effects of the nanocrystal size on the energy levels. We show that we are able to deal with nanocrystals with sizes varying from 1 to 15 nm. Comparisons with experiments are presented, in particular for PbSe nanocrystals which presently receive considerable attention.

With those results in mind, in Chapter 3, we apply similar methods to calculate the electronic structure of more complex PbSe/CdSe quantum dots. The objective was to consider the effects of the geometry and of the nature of the interfaces, and to compare with the case of pure PbSe nanocrystals.

In Chapter 4, we start from the results of the electronic structure calculations of the two previous chapters to simulate the intraband optical spectra which have been recently measured in transient absorption experiments performed by our collaborators within the European project. Our calculations help to identify new intraband transitions which have never been studied so far. The cases of PbSe and PbSe/CdSe nanocrystals are compared. Predictions are also made on photo-induced absorption spectra of CdSe nanocrystals.

Chapter 1

Methodology

This chapter will give a general description of the methods that were used for the analysis of electronic structure and consequent optical properties of nanostructures. *Ab initio* methods, such as the local-density approximation (LDA) in the density-functional theory (DFT), give valuable information for the construction of the Hamiltonian when this is unknown, in small clusters ($\ll 1000$ atoms) with well defined symmetry conditions. When the dimensions of the structure become larger, as it is the case of the nanostructures studied in this work, the computational resources required by these methods are extremely huge. Moreover, some important features of the band structure can not be calculated with accuracy, like the band-gap of semiconductors, except using GW approach, which is limited to systems containing a small number of atoms (at maximum a few dozens, see [4]).

Semi-empirical approaches, such as $\mathbf{k}\cdot\mathbf{p}$, empirical pseudopotential or tight-binding are useful to approximate the single-particle Hamiltonian. Some adjustments from *ab initio* methods can be needed, but in general, this methods can be applied to larger systems than the methods mentioned above, and the estimation of the bandgap is usually better with these methods. The general description of the two types of methods is presented in section 1.1, and the semi-empirical tight-binding method is developed in section 1.2, showing some examples of the band structure calculations for bulk materials in section 1.2.2.

Quantum confinement induces changes in the electronic structure of semiconductors compared to the bulk material. The increase of the width of the bandgap and the change from bands of energy to discrete energy levels are the effects to be presented in section 1.3.

The section 1.4 summarizes the construction of macroscopic optical properties as the absorption coefficient for ensembles of quantum dots, based on the discrete energy levels of these nanostructures.

1.1 Types of Methods

Simulation of electronic properties in nanostructures deals with the problem of approaching a realistic description and solution of the potentials involved. In that picture, we consider a semiconductor nanostructure composed by N atoms, occupying the positions $\mathbf{R}_i$ $(i = 1, 2, \ldots, N)$. We assume that the electronic band structure[1] can be described by a single-particle Hamiltonian $\mathcal{H}$, such that:

[1] When atoms are brought together to form a solid, the outer orbitals of the atoms overlap and interact strongly with each other, then the discrete atomic energy levels split into bands.

$$\mathcal{H}|\Psi\rangle = \epsilon|\Psi\rangle. \tag{1.1}$$

The Hamiltonian $\mathcal{H}$ includes the "mean" effect of electronic interactions. Here we are interested in some number of eigenvalues ϵ_i and eigenstates ψ_i, both in the occupied bands (hereafter called *valence bands*) and in the unoccupied bands (hereafter called *conduction bands*). In conventional semiconductors, there is a gap of energy between the lowest unoccupied molecular orbital, i.e. the bottom of the conduction band and the highest occupied molecular orbital, i.e. the top of the valence band.

In *ab initio* methods based on the DFT, for example, in the local-density approximation (LDA), $\mathcal{H}$ is built from the electronic density in the ground state and then the auto-coherent calculation of *all* occupied states ψ_i^h is needed. The time needed for the calculation is proportional to N^3. As a consequence, LDA can only be applied to small clusters ($\ll 1000$ atoms taking into account the symmetries) and is not adapted to the study of optical properties or transport properties in actual nanostructures. Moreover, LDA underestimates the forbidden band (bandgap) of semiconductors, even if it is possible to apply simple and systematic corrections.

A second group of methods corresponds to the cases where the Hamiltonian can be well approximated by means of the one-particle Hamiltonian $\mathcal{H}_0$ of the corresponding bulk material inside the nanostructure. Semi-empirical methods such as $\mathbf{k}\cdot\mathbf{p}$, effective mass approximation (EMA), empirical pseudopotential (PP) or tight-binding (TB) propose different approximations for $\mathcal{H}_0$, either in the first Brillouin zone (PP, TB) or in the neighborhood of specific $\boldsymbol{k}$ points ($\mathbf{k}\cdot\mathbf{p}$, EMA). All of them are constructed using parameters such as effective masses, pseudopotentials, and hopping integrals, that are adjusted to experimental data or *ab initio* band structures with the ad hoc correction for the forbidden band. The parameters are then transferred to the nanostructures ($\mathcal{H} = \mathcal{H}_0$) over which are applied the appropiate boundary conditions. Depending on the kind of information to be obtained from the calculation, only a few desired states or the whole ensemble are calculated. Semi-empirical methods permit to study the electronic band structure of quantum confined systems larger than those which are possible with *ab initio*. The quality of the description of the band structure of the bulk material and the pertinence in the application of boundary conditions applied to the nanostructures are the two essential criteria to judge a semi-empirical method.

In this work the main interest is to describe the optical properties, and one of the methods that yields good results, in particular that is able to reproduce correctly the value of the bandgap measured in experiments for bulk semiconductors, is the semi-empirical TB. A more complete description of the method is presented in the next section.

1.2 Semi-empirical Tight-Binding

The TB method can be seen as an approximation derived from the linear combination of atomic orbitals (LCAO introduced originally by Bloch in 1928), and the most generalized and simplified form comes from its two center approximation, discussed in the work of Slater and Koster in 1954[5].

The starting point is the Schrödinger's equation 1.1. The wave function eigenstate of $\mathcal{H}$ is written as a combination of localized orbitals centered on each atom

$$\Psi = \sum_{i,\alpha} c_{i\alpha}\psi_{i\alpha}, \tag{1.2}$$

where $\psi_{i\alpha}$ is the α^{th} orbital of atom i, centered at position $\mathbf{R}_i$. If the whole set of orbitals is complete, the exact wave function of the whole system can be given by 1.2. The orbitals $\psi_{i\alpha}$ are not independent as for any given atom the complete set of orbitals forms a base for the Hilbert space. The eigenvalues equation can be also written as

$$\mathcal{H}\Psi = \epsilon S\Psi, \tag{1.3}$$

where Ψ is now the vector of the $n = Nm$ coefficients $c_{i\alpha}$. The $n \times n$ matrix elements for the Hamiltonian $\mathcal{H}$ are of two types:

$$H_{i\alpha,i\alpha} = \langle\psi_{i\alpha}|H|\psi_{i\alpha}\rangle = E_{i\alpha}, \tag{1.4a}$$
$$H_{i\alpha,j\beta} = \langle\psi_{i\alpha}|H|\psi_{j\beta}\rangle\,; \tag{1.4b}$$

Eq. 1.4a represents the energy of the α orbital of i_{th} atom. S corresponds to the overlap matrix

$$S_{i\alpha,j\beta} = \langle\psi_{i\alpha}|\psi_{j\beta}\rangle\,. \tag{1.5}$$

The sum in 1.2 is usually truncated over α, as the description gets restricted to a reduced number of orbitals. Under these conditions the energy levels of the whole system are given by the secular equation

$$det|\mathcal{H} - \epsilon S| = 0. \tag{1.6}$$

The minimal basis set includes orbitals belonging to the outer shell of the free atom. The valence bands and lower conduction bands of conventional semiconductors are usually described by the hybridation of the s orbital and the three p orbitals from the anion's and cation's outer atomic shell. If it is needed the basis can be extended to include five d orbitals, or a complementary s orbital, which is going to be noted as s^*. The orbitals in TB model can differ from the real orbitals of isolated atoms (only the orbital angular symmetry s, p, d is imposed). Due to localization of the orbitals, the integrals $H_{i\alpha,j\beta}$ and $S_{i\alpha,j\beta}$ decrease quickly with the distance between atoms i and j. In consequence, the range of the model is limited to first, second or third neighbors ($H_{i\alpha,j\beta} = S_{i\alpha,j\beta} = 0$ out of this range), then H and S are sparse matrices. In TB, the interatomic overlaps are neglected, i.e. the overlap matrix is equal to the unit matrix I, so it is possible to write the secular equation 1.6 as

$$det|\mathcal{H} - \epsilon I| = 0. \tag{1.7}$$

Notation of the Parameters

The notation employed for the parameters used in this work is similar to the one of Slater-Koster[5]. In a sp^3 basis (with the considerations for symmetry in the two-center approximation), the independent matrix terms obtained are:

$$H_{\alpha,\beta}(i,j) = H_{ss\sigma}(i,j), H_{sp\sigma}(i,j), H_{sp\sigma}(j,i), H_{pp\sigma}(i,j), H_{pp\pi}(i,j), \tag{1.8}$$

where σ represents a p orbital along axis ij and π a p orbital perpendicular to the same axis (Fig. 1.1).

Spin-orbit coupling is taken into account between orbitals of the same atom using the corresponding base with spin. Thus for the sp^3 basis, with the states of spin up $\uparrow$ and down $\downarrow$ there

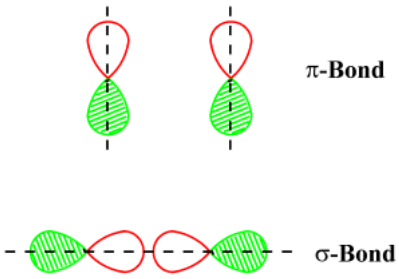

Figure 1.1: The corresponding TB Hamiltonian terms for these p bonds are $H_{pp\pi}(i,j)$ and $H_{pp\sigma}(i,j)$.

are eight orbitals per atom ($|s\uparrow\rangle, |s\downarrow\rangle$, and the analogous for each p). The spin-orbit coupling Hamiltonian for each atom is written:

$$H_i^{SO} = \frac{\Delta_i}{3}\boldsymbol{\lambda}_i \cdot \boldsymbol{\sigma}_i. \tag{1.9}$$

This expression is constructed from the kinetic momentum operator $\mathbf{L}_i = \hbar\boldsymbol{\lambda}_i$, the spin operator $\mathbf{S}_i = \frac{1}{2}\hbar\boldsymbol{\sigma}_i$ over the atom i, and the spin-orbit coupling constant Δ_i. The interatomic matrix elements between orbitals of the same spin are identical to those of the Hamiltonian without spin-orbit coupling, and the terms between orbitals with different spin are neglected.

1.2.1 Adjustment of the Tight-Binding Parameters

It was mentioned before that TB parameters are adjusted over energies $\epsilon_{n,\mathbf{k}}$ of a bulk material for a set of $\mathbf{k}$ points distributed all over the first Brillouin zone (points of high symmetry and some points along the axes). The selected energies $\epsilon_{n,\mathbf{k}}$ are measured or calculated with an *ab initio* method, corrected (if needed) to get the correct energy gap.

The root mean square (rms) deviation between the TB band structure $\epsilon_{n,\mathbf{k}}^{TB}$ and the reference band structure $\epsilon_{n,\mathbf{k}}$

$$\sigma_\epsilon^2 = \sum_{n,\mathbf{k}} \alpha_{n,\mathbf{k}}(\epsilon_{n,\mathbf{k}}^{TB} - \epsilon_{n,\mathbf{k}})^2, \tag{1.10}$$

is minimized with respect to the TB parameters, using for example a method of conjugate gradients[2] or a method of simulated annealing[3]. The simulated annealing is slower than the conjugate gradients but it avoids in principle to get trapped by a local minimum of σ_ϵ^2. The

[2]The only available information about a function $F(x)$ which is needed to minimize, is its value and gradient at a set of points. This technique first defines the conditions to make each minimization step independent of the previous ones. The initial direction (not necessarily the one in which $F(x)$ decreases most rapidly) is taken as the negative of the gradient at the starting point. The next conjugate direction is constructed from a linear combination of the new gradient and the previous direction that minimized $F(x)$. At each iteration the vector space explored is reduced by 1, since the minimizations along the conjugate directions are independent[6].

[3]In this case the space is discrete and in its basic form at each iteration the method aims to lead the system to states of lower energy checking if going to some neighbouring state s' of the current state s or stay in the same state.

coefficients $\alpha_{n,\mathbf{k}}$ ($\sum_{n,\mathbf{k}} \alpha_{n,\mathbf{k}} = 1$) make possible to privilege the description of some parts of the band structure, as it is the case of the neighborhood of the forbidden gap. The quadratic error is thus distributed all over the first Brillouin zone. However, the effective masses at the valence band and the conduction band in most tight-binding models are incorrect. Even though the calculated results on small nanocrystals, in large confinement, are usually satisfying, they do not converge towards those calculated with the $\mathbf{k} \cdot \mathbf{p}$ method in larger nanostructures.

A way to deal with this problem is the one presented in [7] where TB parameters are adjusted over a group of selected energies $\epsilon_{n,\mathbf{k}}$ and the experimental effective masses m_i^* of valence and conduction bands. The rms error is minimized from the expression

$$\sigma^2 = \sigma_\epsilon^2 + K_m \sum_i \beta_i (m_i^{*TB} - m_i^*)^2, \tag{1.11}$$

where $\sum_i \beta_i = 1$. Here K_m has units of eV^2 and the masses are in units of the mass of the free electron. The first step is to obtain the band structure without adjustment of the effective masses (i.e. $K_m = 0$), and then K_m is increased, but at the same time, an improvement on the TB effective masses leads to a degradation of the band structure. It is then necessary to impose some quality limits for the effective masses and the TB energies, as it could be a maximum value of σ_ϵ^2 to achieve the obtaining of the TB parameters.

1.2.2 Tight-Binding on Bulk Materials

To illustrate how semi-empirical TB works for the calculation of band structure, we show some results from previous works on the compounds of main interest in this work.

Cadmium Selenide - CdSe

The first example, CdSe is a II-VI material, with direct bandgap at the Γ point $E_g = 1.85$ eV. It crystallizes in wurtzite (WZ) structure (the most common case, though it is also synthesized with zinc-blende (ZB) structure[8] as described in chapter 3), with cell parameters $a = 4.299$ Å and $c = 7.01$ Å, corresponding to the perfect lattice, i.e. $c = a\sqrt{8/3}$ and/or $u = c/r_0 = 3/8$, being r_0 the nearest neighbor distance. Due to their low dispersion, d valence bands can be neglected so it is enough to apply a sp^3 TB model including nearest neighbors in the two center approximation[9, 10], adjusted to a LDA band structure and the experimental effective mass at the conduction band and introducing spin-orbit coupling, since its splitting here is not negligible (~ 0.4 eV both for WZ or ZB[11]).

The band structure is shown in Fig. 1.2. Valence bands and the two lowest conduction bands are described in the whole first Brillouin zone. The calculated value of the bandgap is $E_g^{TB} = 1.805$ eV and even lower is the discrepancy between the calculated conduction band effective mass $m_e^* = 0.128\ m_0$ and the experimental value $m_e^{*exp} = 0.130\ m_0$. Here and afterwards, the zero of energy on the plots of band structures is located at the top of the valence band.

Cadmium Telluride - CdTe

We present another II-VI semiconductor, CdTe, where the larger atomic number of Te (compared to Se) makes that clusters of this material only exist in ZB form, crystalline structure that can be constructed from two face-centered-cubic (fcc) sublattices (one for each element) displaced by $[111]\,\frac{a}{4}$. The cell parameter is $a = 6.482$ Å, and each atom has four nearest neighbors, forming tetrahedrons. The direct bandgap in this case is $E_g = 1.53$ eV, again at the Γ point.

Intra-atomic terms atom 1 (Cd)	**Intra-atomic terms atom 2 (Se)**
$E_s1 = -11.39201$ eV.	$E_s2 = 1.70734$ eV.
$E_p1 = 0.90756$ eV.	$E_p2 = 5.39164$ eV.
$E_{pz}1 = 0.86256$ eV.	$E_{pz}2 = 5.34664$ eV.
$SO1 = 0.16000$ eV.	$SO2 = 0.07567$ eV.
Hydrogen parameters atom 1 (Cd) and atom 2 (Se)	
$E_H = 0.00000$ eV.	
$V_{ss}H = -3.50000$ eV.	
$V_{ps}H = 4.50000$ eV.	
1 (Cd) - 2 (Se) 1st nearest neighbors parameters	**1 (Cd) - 1 (Cd) 2nd nearest neighbors parameters**
$V_{ss\sigma}12(1) = -1.15622$ eV.	$V_{ss\sigma}11(2) = 0.02024$ eV.
$V_{sp\sigma}12(1) = 1.62238$ eV.	$V_{ps\sigma}(2) = 0.10783$ eV.
$V_{sp\sigma}21(1) = 2.36338$ eV.	$V_{pp\sigma}11(2) = 0.21199$ eV.
$V_{pp\sigma}12(1) = 3.25867$ eV.	$V_{pp\pi}11(2) = 0.02379$ eV.
$V_{pp\pi}12(1) = -0.39548$ eV.	
2 (Se) - 2 (Se) 2nd nearest neighbors parameters:	
$V_{ss\sigma}22(2) = -0.12948$ eV.	
$V_{sp\sigma}22(2) = -0.05565$ eV.	
$V_{pp\sigma}22(2) = 0.42834$ eV.	
$V_{pp\pi}22(2) = -0.25463$ eV.	

Table 1.1: CdSe TB parameters for a sp^3 basis using second-nearest neighbors from Ref. [9]. We introduce the notation for the next parameter tables. The listed terms correspond to interactions on the same atom (intra-atomic), which include the spin-orbit (SO). The interatomic terms are divided into first-nearest neighbors, labeled with (1), and second-nearest neighbors with (2). The atom types, unless it is stated, are numbered "1" for the cation and "2" for the anion. The subscripts follow the notation of Eq. 1.8.

The band structure calculation is obtained with a $sp^3d^5s^*$ basis (ten orbitals) (Fig. 1.3). Here are taken into account only the first nearest neighbors again with two centers, and spin-orbit coupling, whose splitting in this case is larger (about 1 eV), another consequence of the fact that Cd and Te are heavy elements.

On-site parameters atom 1 (Te) :	**On-site parameters atom 2 (Cd) :**
$E_s1 = -8.716293$ eV.	$E_s2 = -1.269161$ eV.
$E_p1 = 2.362764$ eV.	$E_p2 = 5.739082$ eV.
$E_{dyz}1 = 11.204600$ eV.	$E_{dyz}2 = 15.107061$ eV.
$E_{dxz}1 = 11.204600$ eV.	$E_{dxz}2 = 15.107061$ eV.
$E_{dxy}1 = 11.204600$ eV.	$E_{dxy}2 = 15.107061$ eV.
$E_{dxx}1 = 13.061473$ eV.	$E_{dxx}2 = 17.014361$ eV.
$E_{dzz}1 = 13.061473$ eV.	$E_{dzz}2 = 17.014361$ eV.
$E_{s^*}1 = 13.802893$ eV.	$E_{s^*}2 = 17.908140$ eV.
$SO1 = 0.385000$ eV.	$SO2 = 0.065000$ eV.
Hydrogen parameters atom 1 (Te) and atom 2 (Cd)	
$E_H = 0.00000$ eV.	
$V_{ss}H = -35.69727$ eV.	
$V_{ps}H = 61.82948$ eV.	
$V_{ds}H = 0.00000$ eV.	
$V_{s^*s}H = 0.00000$ eV.	
1 (Te) - 2 (Cd) 1st nearest neighbors parameters	
$V_{ss\sigma}12(1) = -1.372451$ eV.	$V_{sp\sigma}12(1) = 2.464283$ eV.
$V_{sp\sigma}21(1) = 2.010538$ eV.	$V_{sd\sigma}12(1) = -0.999978$ eV.
$V_{sd\sigma}21(1) = -0.947854$ eV.	$V_{ss^*\sigma}12(1) = 0.177593$ eV.
$V_{ss^*\sigma}21(1) = 0.171087$ eV.	$V_{pp\sigma}12(1) = 3.633352$ eV.
$V_{pp\pi}12(1) = -0.770868$ eV.	$V_{pd\sigma}12(1) = -0.994358$ eV.
$V_{pd\sigma}21(1) = -0.166481$ eV.	$V_{pd\pi}12(1) = 1.364603$ eV.
$V_{pd\pi}21(1) = 2.200983$ eV.	$V_{ps^*\sigma}12(1) = -0.299793$ eV.
$V_{ps^*\sigma}21(1) = -0.299617$ eV.	$V_{dd\sigma}12(1) = -2.100122$ eV.
$V_{dd\pi}12(1) = 1.714043$ eV.	$V_{dd\delta}12(1) = -0.727556$ eV.
$V_{ds^*\sigma}12(1) = -0.047237$ eV.	$V_{ds^*\sigma}21(1) = -0.231393$ eV.

Table 1.2: CdTe TB parameters. First-nearest neighbors interactions in a $sp^3d^5s^*$ basis. (Acknowledgements: Guy Allan.)

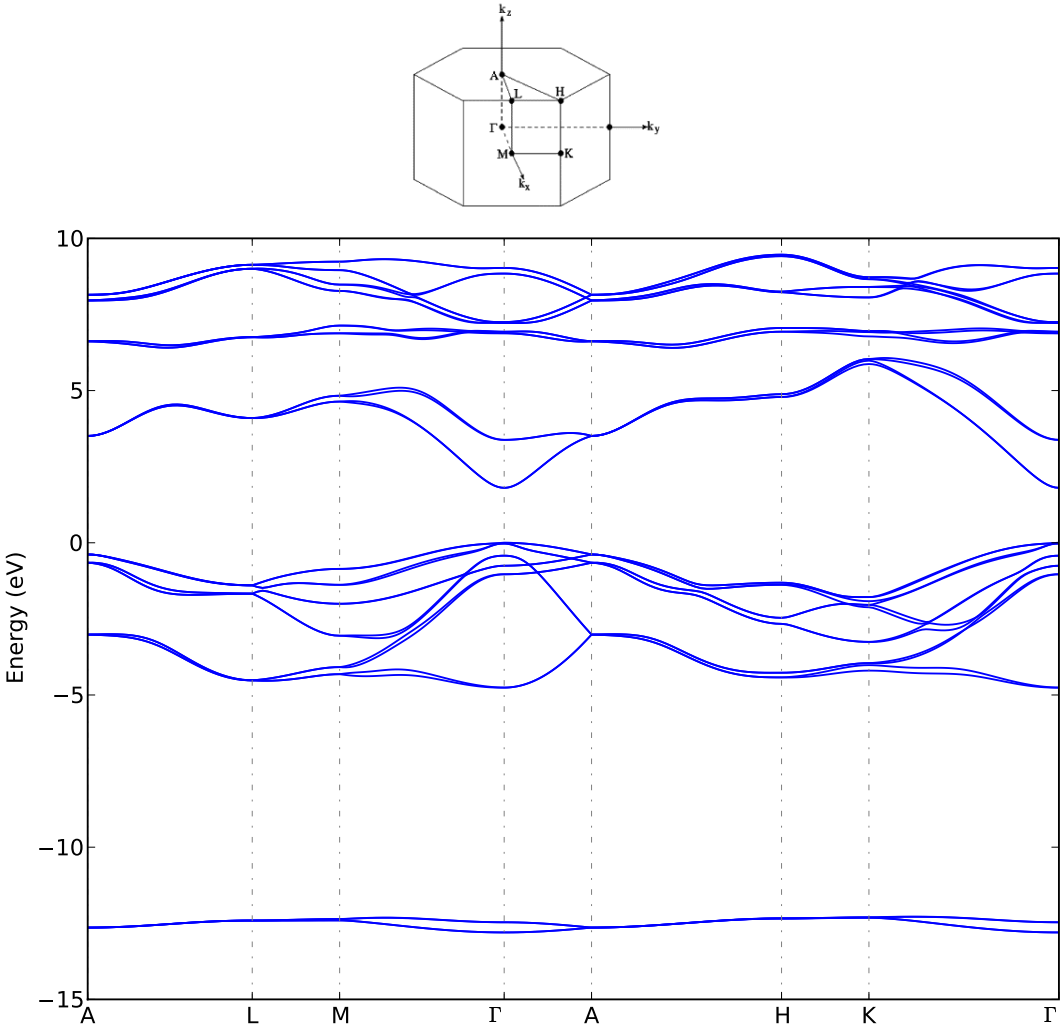

Figure 1.2: Wurtzite CdSe Bulk band structure. The Brillouin zone showing the symmetry points for the WZ lattice is displayed on top. The top of the valence band is at zero of energy.

Lead Selenide - PbSe

The last example, PbSe, is a IV-VI semiconductor with cubic rock-salt (RS) structure[4] like NaCl, and a cell parameter $a = 6.17$ Å. The nearest neighbor distance is the half of that quantity, each atom having six first nearest neighbors of the opposite type around it oriented in the directions of the main coordinate axes. It can be seen as two fcc sublattices for each element displaced by $[100]\,\frac{a}{2}$.

The parameters used here are taken from [13]. The band structure obtained for the bulk PbSe is shown in Fig. 1.4. Here the Hamiltonian matrix is written in a $sp^3d^5s^*$ basis restricted to first nearest neighbors interactions, including the effect of spin-orbit coupling, thus the basis set is doubled. Pb has a high atomic number and then the relativistic effects localize its valence on the $6s$ orbital, transforming Pb into a $6p^2$ atom[14].

[4]PbSe is often mentioned as a "pseudo II-VI" compound[12], and should behave like the two previous compounds. Due to the high atomic number of Pb, the coordination number on PbSe is larger than in other metallic monoselenides (CdSe, ZnSe, etc.), going from 4 to 6.

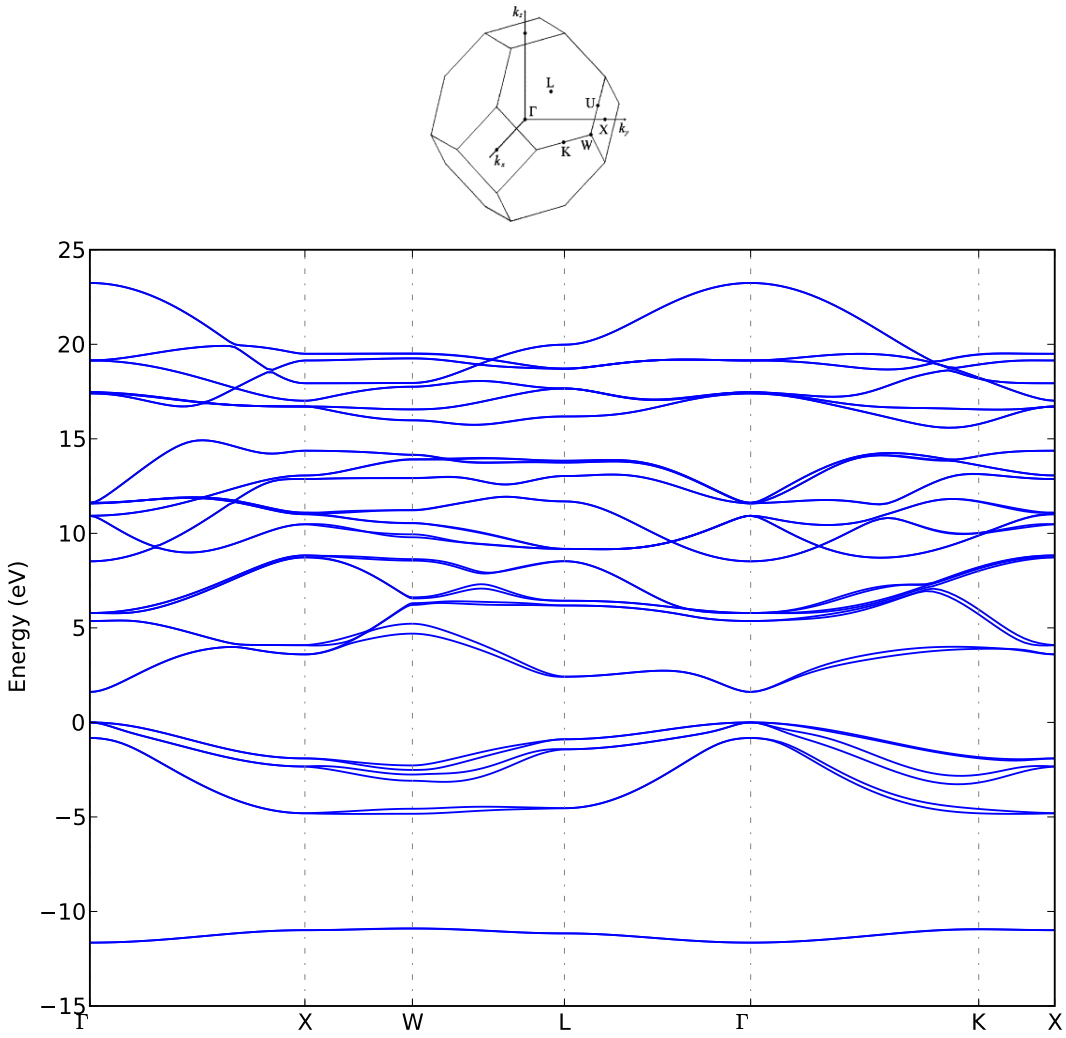

Figure 1.3: CdTe Bulk band structure.

One peculiarity of the band structure of IV-VI semiconductors (like PbS and PbTe), is the presence of the gap at the L point. In the fcc Brillouin zone, there are four equivalent L-point valleys, so after inclusion of spin the valence band maximum and conduction band minimum are eight-fold degenerate.

The energy gap for bulk PbSe in this case is $E_g = 0.176$ eV at 0K, but there is a strong dependence of the energy gap on the temperature, and in quantum dots the variation on the temperature is also size dependent[13, 15]. This is going to be discussed in chapter 2. Before, we introduce the effects of quantum confinement.

1.3 Quantum Confinement

In the previous section, we presented some examples of the electronic structure of bulk semiconductors, characterized by delocalization of electronic states and a quasi continuous spectrum of energies in the conduction band and the valence band. The electrons, holes and excitons are free to move in three dimensions. Some interesting modifications on the electronic properties of semiconductors appear with the creation of structures where the carriers are confined in space,

On-site parameters atom 1 (Pb)	**On-site parameters atom 2 (Se)**
$E_s1 = -5.07781$ eV.	$E_s2 = -11.45405$ eV.
$E_p1 = 4.33168$ eV.	$E_p2 = -1.47533$ eV.
$E_d1 = 10.97439$ eV.	$E_d2 = 12.13125$ eV.
$E_{s^*}1 = 24.35922$ eV.	$E_{s^*}2 = 17.60374$ eV.
$SO1 = 0.55000$ eV.	$SO2 = 0.24000$ eV.
1 (Pb) - 2 (Se) 1st nearest neighbors parameters	
$V_{ss\sigma}12(1) = -0.36267$ eV.	$V_{sp\sigma}12(1) = 1.31029$ eV.
$V_{sp\sigma}21(1) = 1.20593$ eV.	$V_{sd\sigma}12(1) = -1.71725$ eV.
$V_{sd\sigma}21(1) = -0.83693$ eV.	$V_{ss^*\sigma}12(1) = -1.29525$ eV.
$V_{ss^*\sigma}21(1) = -1.12089$ eV.	$V_{pp\sigma}12(1) = 1.71542$ eV.
$V_{pp\pi}12(1) = -0.38235$ eV.	$V_{pd\sigma}12(1) = -2.13886$ eV.
$V_{pd\sigma}21(1) = -1.07458$ eV.	$V_{pd\pi}12(1) = 0.73701$ eV.
$V_{pd\pi}21(1) = -0.14844$ eV.	$V_{ps^*\sigma}21(1) = -2.27510$ eV.
$V_{ps^*\sigma}12(1) = -2.51117$ eV.	$V_{dd\sigma}12(1) = -0.27384$ eV.
$V_{dd\pi}12(1) = 1.48923$ eV.	$V_{dd\delta}12(1) = -0.35624$ eV.
$V_{ds^*\sigma}21(1) = 0.18794$ eV.	$V_{ds^*\sigma}12(1) = -0.92754$ eV.
$V_{s^*s^*\sigma}12(1) = -0.93835$ eV.	

Table 1.3: PbSe TB Parameters. First-nearest neighbors interactions in a $sp^3d^5s^*$ basis[13].

like in quantum wells, wires or dots. The purpose of this section is to introduce briefly two important consequences of quantum confinement on the energy spectrum.

1.3.1 From Bands to Discrete Energy Levels

The confinement is going to be defined in terms of the number of free dimensions of the carrier in the system. In this description, quantum wells are 2D systems, since the mentioned particles are confined in only one direction. Quantum wires represent 1D systems. Going up to confinement of the particles in three dimensions, we get quantum dots, 0D systems. In the following, we discuss the electronic structure of those confined systems using simple effective mass approximation (EMA).

Quantum Wells and Wires

We present first the most basic case, a quantum well in the region $-L_z/2 \leq z \leq L_z/2$ with high (infinite) potential barriers, so free motion of a particle with effective mass m is allowed in the x, y plane. The boundary conditions along the z axis imply that the probability to localize the particle (either electron or hole) at the interfaces and out of this region is null. This can represent a layer of a semiconductor sandwiched between two layers of any semiconductor or insulator with a bandgap much larger than in the well.

Under these conditions the form of the wave function in EMA along the direction z is

$$\psi(z) = \sqrt{\frac{2}{L_z}} \sin\left(\frac{n\pi z}{L_z}\right), \tag{1.12}$$

where $n \neq 0$ is a positive integer, and the allowed energy values are then discrete, of the form

$$E_n = \varepsilon n^2, \tag{1.13}$$

with $\varepsilon = \left(\frac{\hbar^2\pi^2}{2mL_z^2}\right)$. This is enough to deduce the first important consequence of quantum confinement, the energy spectrum becomes discrete in the direction of the confinement.

Something also important to notice is that the levels of energy are inversely proportional to the effective mass, so the electrons, heavy holes and light holes will all have different quantization energies ε. Energy of the levels is also inversely proportional to the square of the well width ($\propto 1/L_z^2$), and these two rules apply also for the more realistic case where the potential of the

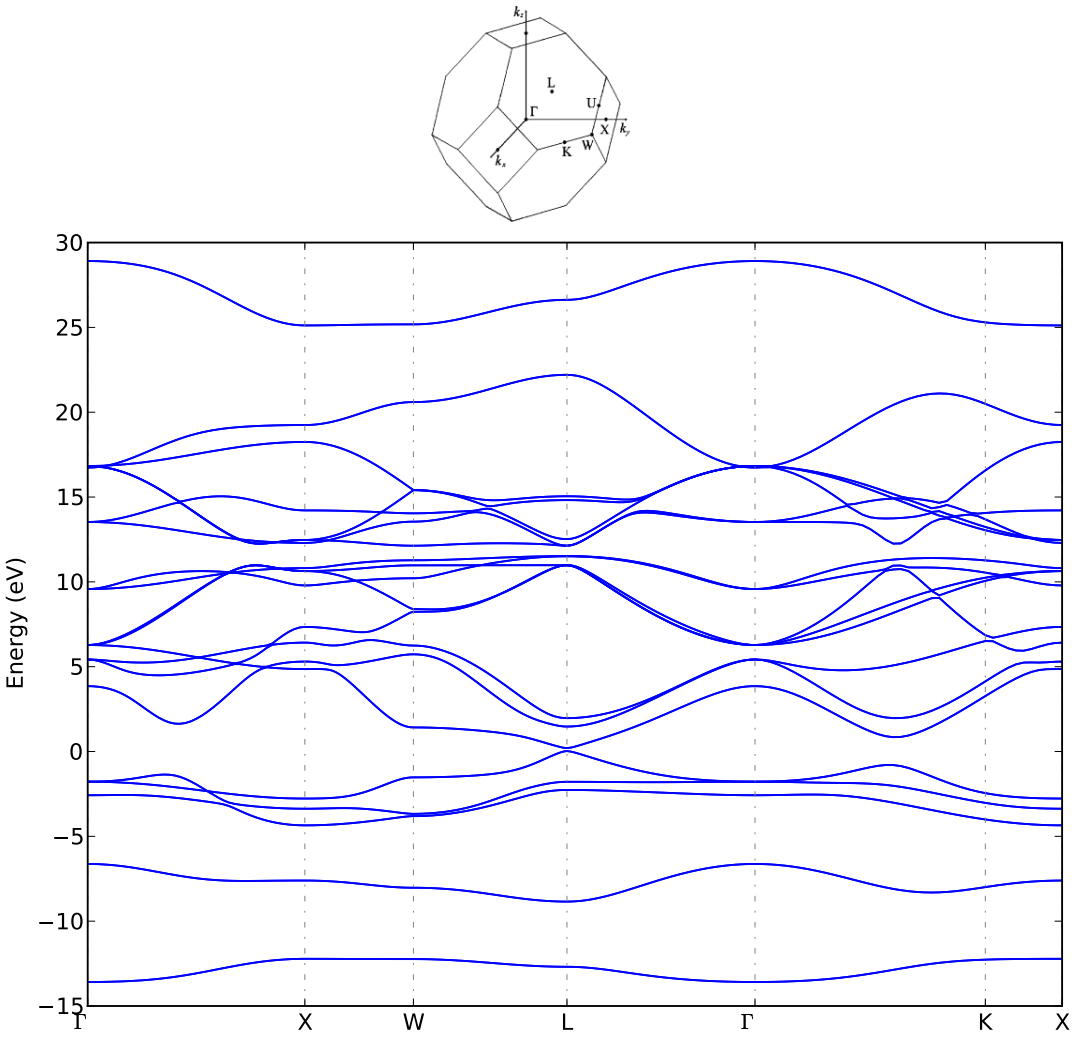

Figure 1.4: PbSe Bulk band structure.

barriers is finite. The second rule makes possible to understand how it is possible to tune the position of the energy levels when the size of the nanostructure is modified. Since electrons are free to move in two directions (x, y), 2D confinement leads to formation of subbands at each energy ε.

If 1D confinement takes place, as it is the case in a quantum wire, the solution is composed by superposition of solutions from the previous case, and the effect is also the creation of subbands. Our interest is focused on 0D systems, so we do not extend the description of this 1D case.

Cubic Quantum Dots

If the well is spanned to the three directions in space, the solution is again a composition of solutions from the 2D case. The energies in the case of an infinite square potential are

$$\varepsilon_{n_x,n_y,n_z} = \frac{\hbar^2\pi^2}{2m}\left[\left(\frac{n_x}{L_x}\right)^2 + \left(\frac{n_y}{L_y}\right)^2 + \left(\frac{n_y}{L_y}\right)^2\right]. \tag{1.14}$$

In a regular cubic dot $L_x = L_y = L_z$, and using spin, the ground state ε_{111} has a twofold

degeneracy, and the first excited level is sixfold degenerate. This is similar to the case of an atom with twofold degenerate S state and sixfold degenerate P state, and that is mainly the reason to call the quantum dots as *artificial atoms*.

Spherical Quantum Dots

When the confinement potential has spherical symmetry inside a region of radius R, the result is a spherical quantum dot. The eigenstates now are composed by a radial part and spherical harmonics Y_{lm} where the index l is related with the orbital momentum operator $\mathbf{L}$. The solutions are

$$\varepsilon_{nl} = \frac{\hbar^2\pi^2}{2m}\left(\frac{X_{nl}}{R}\right)^2, \quad n = 1, 2, 3, ..., \quad l = 0, 1, 2...,$$
$$\psi_{nlm}(r, \theta, \psi) = A j_l\left(\frac{X_{nl}r}{R}\right) Y_{lm}(\theta, \psi), \tag{1.15}$$

where j_l is a spherical Bessel function and X_{nl} are zeros of the spherical Bessel functions labelled with n in order of increasing energy. The values of l are not restricted to a given n in the way $l < n$, as in real atoms, but the levels of energy are labeled with the usual atomic notation, so $1S$ corresponds to $l = 0$ and $n = 1$.

1.3.2 Density of States and Bandgap

Another effect of confinement can be described with the help of the density of states[5] for the different cases presented above. In the bulk, this quantity is a continuous function of energy with parabolic shape (Fig. 1.5)

$$\rho_{bulk} = \frac{m\Omega}{\pi^2\hbar^2}\sqrt{\frac{2m}{\hbar^2}\varepsilon}. \tag{1.16}$$

where Ω is the volume of the system. We kept all the terms in this expression to show the dependence on the quantities that make part also of the expression for the energy. In a 2D system, it changes to be a function of the form

$$\rho_{2D}(\varepsilon) \propto \sum_n \Theta(\varepsilon - \varepsilon_n), \tag{1.17}$$

with the step function $\Theta(x) = \begin{cases} 1, & (x > 0), \\ 0, & (x \leq 0). \end{cases}$

A comparison between the densities from expressions 1.16 and 1.17 can be seen in Fig. 1.5, where it is important to notice that $\rho_{2D} = 0$ for $\varepsilon < \varepsilon_1$, valid for electrons and holes, and that can be understood as an increase of the width of the bandgap compared to the bulk, the second important consequence of confinement.

In a quantum wire, the density of states changes to the form

$$\rho_{1D}(\varepsilon) \propto \sum_{\varepsilon_n < \varepsilon} \frac{1}{\sqrt{\varepsilon - \varepsilon_n}}, \tag{1.18}$$

then the density of states diverges at ε_n, as shown in Fig. 1.5.

[5]Defined as the number of allowed states per unit energy around a given energy ε.

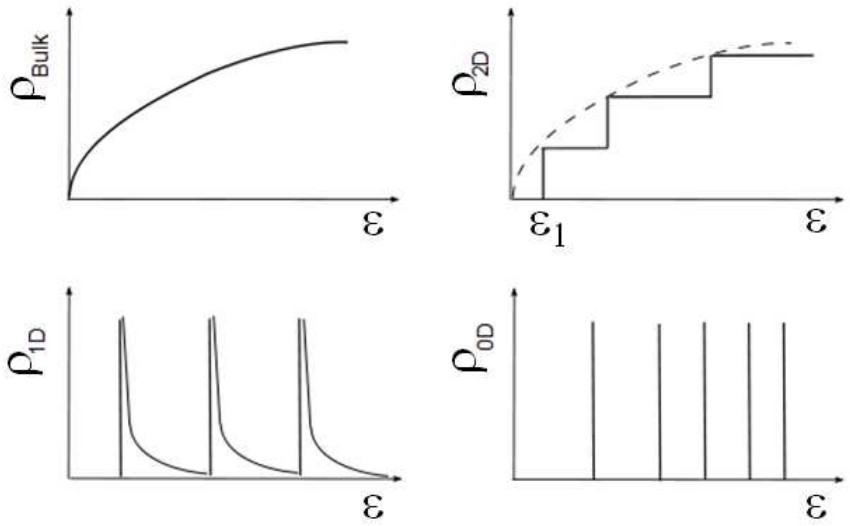

Figure 1.5: Density of states at 3D, 2D, 1D and 0D. The curve for the bulk material is included in the density of states for an infinite square well (dashed line for ρ_{2D}) for comparison between the 3D and 2D confinement, for the latter one, $\rho_{2D} = 0$ if $\varepsilon < \varepsilon_1$.

Finally, for quantum dots of any shape

$$\rho_{0D}(\varepsilon) \propto \sum \delta(\varepsilon - \varepsilon_n). \tag{1.19}$$

This result means, among other implications, that the photoluminescence and the optical absorption at 0K from a quantum dot should show very sharp lines in absence of electron-phonon coupling [16].

In any case, the density of states in the bulk material is still responsable for the distribution of discrete energy levels in quantum dots, so the TB parameters used for the bulk are valid. The TB calculations applied have to include good boundary conditions, then also a correct description of the surface is needed. When passivation of dangling bonds is required, the way to do it is with hydrogen, using first nearest neighbor interactions and an $1s$ orbital of H atoms to simulate chemical passivations of the nanocrystals.

To finish with this chapter, we introduce the deduction of macroscopic optical properties from the electronic structure of nanocrystals.

1.4 Optical Properties

The starting point is the electronic structure of individual nanocrystals within a defined range of sizes. As a feedback from the last section, we emphasize that we are dealing with discrete energy levels and the probabilities of electronic transitions between them. Following Fermi's golden rule[17], the quantum mechanical transition rate for exciting an electron in an initial state $|\psi_i\rangle$ to a final state $|\psi_j\rangle$ by absorption of a photon of angular frequency ω, depends on the product of two factors:

- the square of a matrix element describing the effect of the external perturbation caused by the light wave on the electrons.
- the density of states.

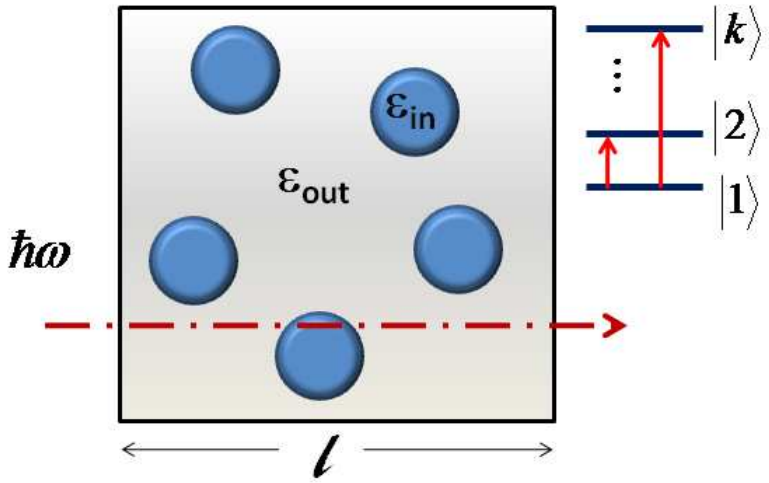

Figure 1.6: Semiconductor nanocrystals of dielectric constant ϵ_{in} embedded in an homogeneous medium with dielectric constant ϵ_{out}. The absorption is measured by the attenuation on the intensity of the transmitted light through the sample. The transition $|1\rangle \rightarrow |k\rangle$ of electrons to excited levels is induced by absorption of a photon of energy $\hbar\omega_{k1}$.

And from the transition rate it is possible to obtain the optical absorption coefficient. We have already an idea of the density of states for the case of quantum dots, now it is necessary to define the matrix element.

1.4.1 Optical Absorption of Nanocrystals

We consider a system composed of N nanocrystals per unit volume, embedded in an homogeneous medium with dielectric constant ϵ_{out} as shown in figure 1.6. The volume of a nanocrystal is Ω, so the volume fraction of nanocrystals is $p = N\Omega$. The frequency-dependent dielectric constant for the quantum dots is ϵ_{in}, and the composite medium is absorbing and non magnetic ($\mu = 1$). Since we are interested in colloidal quantum dots, the situation is not distant from the reality, with the medium represented by the solvent.

The system is irradiated with monochromatic light of intensity I_0, as in the case of an absorption experiment, and what is measured is the intensity of transmitted light. In an absorbing medium of thickness l (Fig. 1.6) this intensity is given by

$$I = I_0 \exp(-\alpha l), \tag{1.20}$$

with α the absorption coefficient. The interaction of the electrons with the electromagnetic field in the system leads directly to electronic transitions between the energy levels, and the case of interest is when the field inside the nanocrystals induces the transition of electrons to excited levels by absorption of a photon. The probability of transition of an electron is thus proportional to the intensity of the electromagnetic field inside the nanocrystal. Spontaneous emission is not going to be treated here.

Since dielectric constants of the particles and surrounding medium are different (usually the one corresponding to the medium is smaller), it is clear that fields are not homogeneous, and the effects of internal local field appear. However, the size of the nanocrystals is small compared to the wavelength of the absorbed photon, so it is possible to define an average electromagnetic

field for which is possible to describe the composite material as homogeneous and isotropic, with an effective dielectric constant ϵ_M.

Local Fields and Dielectric Constant

For quantum dots with spherical shapes, taking into account that the wavelength of the electromagnetic wave is much larger than the size of the particles, the field inside the nanocrystal is uniform and directly proportional to the field outside. Under these conditions it is possible to define a local field factor such that $\mathbf{E}_{in} = F\mathbf{E}_{out}$. The local field factor when all crystals are spherical is defined as

$$F = \frac{3\epsilon_{out}}{\epsilon_{in} + 2\epsilon_{out}}. \tag{1.21}$$

The dielectric constant is complex and frequency dependent $\epsilon_M = \epsilon'_M(\omega) + i\epsilon''_M(\omega)$ as it is the refractive index $K_{ref} = n_{op} + iK_{op} = \sqrt{\epsilon_M}$, with n_{op} the (real) refractive index of the system and K_{op} the extinction coefficient. The relation between real and complex parts of the dielectric constant and the refractive index is given by the expressions

$$\begin{aligned} \epsilon'_M &= n_{op}^2 - K_{op}^2, \\ \epsilon''_M &= 2n_{op}K_{op}. \end{aligned} \tag{1.22}$$

And the absorption coefficient from 1.20 can also be written from the complex part of the refractive index as

$$\alpha = \frac{2\omega K_{op}}{c}. \tag{1.23}$$

Notice that $\mathbf{D}_{in} = \epsilon_{in}\epsilon_0\mathbf{E}_{in}$, $\mathbf{D}_{out} = \epsilon_{out}\epsilon_0\mathbf{E}_{out}$, and for the composite medium the average electric displacement and the average electric field are related as $\bar{\mathbf{D}} = \epsilon_0\bar{\mathbf{E}} + \mathbf{P} = \epsilon_M\epsilon_0\bar{\mathbf{E}}$. The average fields in the composite medium are given by

$$\begin{aligned} \bar{\mathbf{D}} &= p\mathbf{D}_{in} + (1-p)\mathbf{D}_{out}, \\ \bar{\mathbf{E}} &= p\mathbf{E}_{in} + (1-p)\mathbf{E}_{out}. \end{aligned} \tag{1.24}$$

For small values of p, $\epsilon_M \propto \epsilon_{out}$ is real and constant, so $n_{op} \approx \sqrt{\epsilon'_M}$ and the coefficient from 1.23 can be approximated by

$$\alpha \approx \frac{\omega}{cn_{op}}\epsilon''_M \approx \frac{\omega}{cn_{op}}p\left(\frac{3\epsilon_{out}}{\epsilon_{in} + 2\epsilon_{out}}\right)^2 \epsilon''_{in} = \frac{\omega}{cn_{op}}pF^2\epsilon''_{in}. \tag{1.25}$$

Thus the absorption coefficient is proportional to the imaginary part of the dielectric constant, but multiplied by the volume concentration of nanocrystals and the square of the local field factor, as should be from the relation between the field and the intensity and this term is also consistent with the expressions 1.20 and 1.22. Now we must write the relation between this term and the electronic levels of energy of the system.

Matrix Element Construction

Transitions of electrons between the discrete levels of the nanocrystal induce a dipolar momentum $\mathcal{P}$, related to the average polarization by $\mathbf{P} = \mathcal{P}/\Omega$. It can also be written as the statistical average of the operator $-e\mathbf{r}$ (with e the charge of the electron and $\mathbf{r}$ the position vector of the electron)

$$\mathcal{P} = \mathrm{Tr}[\rho(-e\mathbf{r})], \tag{1.26}$$

where we introduce the statistical density matrix ρ_{ij}. The system can be characterized by the Hamiltonian $H = H_0 + W(t)$ which includes the electronic Hamiltonian H_0 in absence of electromagnetic field and the perturbation corresponding to the presence of the field when the system is irradiated $W(t) = e\mathbf{r} \cdot \mathbf{E_0}\mathrm{e}^{-i\omega t}$. The matrix ρ_{ij} is calculated in the basis of the eigenstates of H_0. The diagonal terms ρ_{ii} represent the probability to find the system in the state $|i\rangle$ and also give an expression for the conservation of the electronic population in the system $\sum_i \rho_{ii} = 1$. The equilibrium values of the population of states f_i can be reached starting with these diagonal terms in the regime of weak excitations, i.e. $\Delta\rho = \rho_{ii} - \rho_{jj} \approx f_i - f_j$.

The evolution of the system can be described then in the density matrix formulation of Schrödinger equation

$$\mathrm{i}\hbar\frac{d\rho}{dt} = [H, \rho]\,. \tag{1.27}$$

We consider the transitions between two levels $|i\rangle, |j\rangle$ of energies ε_i and ε_j respectively, for which we define a frequency term $\omega_{ji} = (\varepsilon_j - \varepsilon_i)/\hbar$. The different expressions appearing from the matrix terms get simplified in the permanent regime, where the populations (as already defined) ρ_{ii} become constant, and the non-diagonal terms oscillate with a frequency ω[18], i.e. $\rho_{ij} = \rho^0_{ij}\exp(-\mathrm{i}\omega t)$, and the amplitudes of these terms can be written as

$$\begin{aligned}
\rho^0_{ji} &= \frac{W_{ij}[f_i - f_j]}{\hbar\omega - \hbar\omega_{ji} + \frac{\mathrm{i}\hbar}{\tau}}, \\
\rho^0_{ij} &= -\frac{W_{ij}[f_i - f_j]}{\hbar\omega + \hbar\omega_{ji} + \frac{\mathrm{i}\hbar}{\tau}},
\end{aligned} \tag{1.28}$$

where $W_{ij} = e\langle\mathbf{r}_{ij}\rangle \cdot \mathbf{E}_0\mathrm{e}^{-i\omega t} = e\langle i|\mathbf{r}|j\rangle \cdot \mathbf{E}_0\mathrm{e}^{-i\omega t}$, and τ is the decoherence time of these non-diagonal terms due to random interactions. Some effects such as spontaneous emission or electron-phonon coupling, that are not included directly in the model, are usually described through τ. In the limit $\tau \to +\infty$

$$\lim_{\tau\to+\infty} \mathrm{Im}\left(\frac{1}{\hbar\omega - \hbar\omega_{ji} + \frac{\mathrm{i}\hbar}{\tau}}\right) = -\pi\delta(\hbar\omega - \hbar\omega_{ji}). \tag{1.29}$$

Making use of the expression 1.26, and its relation with the average polarization vector

$$\mathbf{P} = -\frac{e\langle\mathbf{r}_{ij}\rangle}{\Omega}\left(\rho^0_{ji} + \rho^0_{ij}\right)\mathrm{e}^{-i\omega t}, \tag{1.30}$$

taking into account $\epsilon_{in} = 1 + \mathbf{P}/(\epsilon_0\mathbf{E})$ it is be possible to write the dielectric constant introducing the terms from 1.28 in 1.30. We are interested in the imaginary part of ϵ_{in}, which has a resonance when $\omega = \omega_{ji}$. As the system has a large number of levels, it is possible to sum over all possible transitions $|i\rangle \to |j\rangle$ of one electron, each one followed by the absorption of a

photon of energy $\hbar\omega_{ji}$, so the energy dependent absorption in the limit shown in 1.29 for small values of p in 1.25 is

$$\alpha(\hbar\omega) = pF^2 \sum_{ij} \frac{\omega_{ij} e^2 |\langle i|\mathbf{r}\cdot\mathbf{e}|j\rangle|^2 \pi}{c n_{op} \epsilon_0 \Omega} \delta\left(\hbar\omega - \hbar\omega_{ji}\right)\left[f_i - f_j\right], \tag{1.31}$$

where $\mathbf{e}$ is the polarization vector of the electric field. If we take into account the shape of the density of states in 1.19 and the statement at the beginning of this section, this expression is what we were looking for. The matrix term defines the strength of the optical coupling between two levels $|i\rangle$ and $|j\rangle$, often described by the oscillator strength

$$f_{ji} = \frac{2m_0}{\hbar}\omega_{ji} |\langle i|\mathbf{r}\cdot\mathbf{e}|j\rangle|^2, \tag{1.32}$$

a quantity without dimension for which

$$\sum_i f_{ji} = 1. \tag{1.33}$$

Here is also possible to define the optical cross section σ from 1.20 as $I = I_0 \exp(-\alpha l) = I_0 \exp(-\sigma l N)$, then

$$\sigma = \frac{\alpha}{N} = \alpha \frac{\Omega}{p}, \tag{1.34}$$

and it will be enough to replace $\alpha(\hbar\omega)$ from 1.31.

From the TB electronic structure calculations it is straightforward to obtain the oscillator strength using the values of the energy levels already obtained at the valence band and the conduction band and an arbitrary polarization vector $\mathbf{e}$. The absorption is built from the lineshape of each individual transition at each energy in the expression of the oscillator strength and averaged over all orientations of the electric field. In this work we considered a Gaussian lineshape

$$L(x) = \frac{1}{\sigma\sqrt{2\pi}} \exp\left(-\frac{x^2}{2\sigma^2}\right), \tag{1.35}$$

with σ in units of energy. The resulting expression for the cross section is

$$\sigma(\hbar\omega) = F^2 \sum_{ij} \frac{\pi\omega_{ij} e^2 |\langle i|\mathbf{r}\cdot\mathbf{e}|j\rangle|^2}{c n_{op} \epsilon_0} L\left(\hbar\omega - \hbar\omega_{ji}\right)\left[f_i - f_j\right]. \tag{1.36}$$

In 1.31 and 1.36, following the notation in section 1.2 the levels $|i\rangle$ and $|j\rangle$ are written as

$$\begin{aligned} |i\rangle &= \sum_{k,\alpha} c^i_{k\alpha} \psi_{k\alpha}, \\ |j\rangle &= \sum_{l,\beta} c^j_{l\beta} \psi_{l\beta}, \end{aligned} \tag{1.37}$$

thus the terms $\langle r_{ij}\rangle$ from ρ_{ij} in Eq. 1.28 and also implicit in the expressions for absorption and cross-section, are written as

$$\langle i|\mathbf{r}|j\rangle = \sum_k \left(\sum_\alpha c^{i*}_{k\alpha} c^j_{k\alpha}\right) \mathbf{R}_k, \tag{1.38}$$

where $\mathbf{R}_k$ is the position of the atom k.

A sufficient number of calculated states in both valence band and conduction band represents a larger range of energy values for the optical transitions, so depending on the size of the nanocrystals, a full diagonalization procedure of the Hamiltonian matrix is desirable. The parameters to be taken into account from the experiments are the local field factor F, deduced from dielectric constant of the quantum dot material and the embedding medium (the solvent for colloidal suspensions), deduced from its refractive index.

Conclusions

The semi-empirical tight binding method exhibits some advantages for the systems studied in this work. The calculation of the bulk electronic structure reproduces correctly the value of the bandgap, and splitting due to spin-orbit coupling. We include some examples to illustrate this, applied on compounds that have shown interesting properties for the synthesis of nanocrystals. This method can be extended to large clusters, in comparison to methods based like the local-density approximation, which underestimates the value of the bandgap, making necessary to apply systematic corrections.

In the effective mass approximation, the confinement of the carriers in three dimensions results in a discrete spectrum of energy with some similarities in the description of the degeneracy and in the notation used in atoms, especially when the confinement potential has spherical symmetry. The density of states is also modified, going from a continuous (parabolic) function of the energy in the bulk material, to a group of delta functions, still under the influence of the distribution of energy from the bulk, and that is a reason to use the same parameters for the calculation of the bulk band structure in the next chapters.

Macroscopic optical properties can be deduced from the electronic structure of nanocrystals. We are interested in the optical absorption, for which we are able to build an expression based on the density of states and the optical coupling, that we define in terms of the transition rate between couples of energy levels. With a sufficient number of states from the calculations of the electronic structure of quantum dots, we are able to describe optical transitions in significant ranges of energy.

Chapter 2

Electronic Structure of Quantum Dots

This chapter summarizes some results on the electronic band structure of PbSe, CdSe and CdTe quantum dots. The calculations are based on the TB bulk electronic structure already presented in section 1.2.2, and the considerations on quantum confinement introduced in section 1.3.

The first section briefly describes the minimization methods that can be applied in the cases when a full diagonalization of the Hamiltonian matrix is not needed, since the calculation of a small number of states could be sufficient, or the number of atoms in the clusters is large enough to make difficult to get the full set of eigenstates.

We present for the three compounds the analysis of the size dependence of the gap and the inter-valley splittings, giving some especial attention to PbSe quantum dots, including a different shape of the nanocrystals which will be useful in the next chapter.

2.1 Semiempirical Tight-Binding in Nanostructures

Early works on the TB electronic structure calculation of small nanocrystals show its convenience for clusters in ranges from a few hundred atoms to about 2500, in comparison to methods based on the effective-mass approximation (for which the bandgap is overestimated for small clusters)[19, 20]. Reports on the application of semi-empirical pseudopotential methods to calculate the electronic structure reproduce very well exciton energies from experiments, but limited to clusters of about 1000 atoms[21]. We are interested in systems that go over those limits, to assure a correct characterization of the effects of size on the electronic structure.

2.1.1 General Considerations

For the three compounds shown below, spherical quantum dots were built with diameters varying from 1.0 nm $\sim$ 18 nm, or in terms of number of atoms, it represents clusters from $N = 8$ (a situation not realistic) to $N \sim 100000$ semiconductor atoms, so it gives an idea of the dimension of the TB matrix to build in each case, taking into account that the inclusion of spin-orbit coupling doubles the dimension of the Hamiltonian matrix, which is not real symmetric, but complex hermitian in these cases. All dangling bonds, when present, are saturated with hydrogen atoms to avoid surface states in the gap[7, 10], but the number of H atoms included does not affect in a significant way the dimension of the Hamiltonian.

For large clusters ($d \geq 6.0$ nm; $N \sim 4000$) it becomes costly in terms of computation to do a full diagonalization of the Hamiltonian to obtain the electronic structure. However, in many cases it is sufficient to calculate a small number of states around the gap region, the full set of eigenstates is not necessary.

The alternatives to calculate that limited number of states from such large matrices are the Jacobi-Davidson (JD) diagonalization or a conjugate gradient (CG) procedure.

2.1.2 Minimization Methods

In the JD iteration method[22], a subspace $K_n = |\phi_1\rangle, \ldots, |\phi_n\rangle$ is built in such a way that there is fast convergence of the associated eigenpairs of the Hamiltonian H, that can be written in a current approximation $\{E_n, |\psi_n\rangle\}$. It is possible to augment K_n with a vector $|\phi_{n+1}\rangle$ that, in the subspace orthogonal to $|\psi_n\rangle$ and a matrix of already known eigenvectors Q (if any), is the solution of

$$(H - E_n I)\,|\phi_{n+1}\rangle = |r_n\rangle, \tag{2.1}$$

where $|r_n\rangle = H|\psi_n\rangle - E_n|\psi_n\rangle$. Here $\{E_{n+1} = E_n, |\psi_{n+1}\rangle\}$ is an exact eigenpair of H in K_{n+1} (the augmented subspace). The closer E_n gets to the target eigenvalue, the faster the ratio $|r_{n+1}|/|r_n|$ decreases.

The other alternative, CG method [6, 23] minimizes the expectation value of $(H - \sigma I)^2$ for a given trial vector $|\psi\rangle$ and an arbitray target value σ

$$R(|\psi\rangle) = \frac{\langle\psi|(H - \sigma I)^2|\psi\rangle}{\langle\psi|\psi\rangle}, \tag{2.2}$$

i.e. $|\psi\rangle$ is an eigenvector of H associated with the eigenvalue closest to σ. Once one (or more) eigenvectors $\{|\psi_1\rangle, \ldots, |\psi_n\rangle\}$ are converged, the other ones can be found in the corresponding orthogonal subspace using Gram-Schmidt orthogonalization and further minimizing

$$R'(|\psi\rangle) = \frac{\langle\psi'|(H - \sigma * I)^2|\psi'\rangle}{\langle\psi'|\psi'\rangle}, \tag{2.3}$$

where $|\psi'\rangle = |\psi\rangle - \sum_i \langle\psi_i|\psi\rangle|\psi_i\rangle$. A preconditioner i.e. an approximate inverse P of $(H - \sigma I)^2$ can help to speed-up the convergence. Another term that determines the efficiency of the CG algorithm is the *condition number* i.e. the ratio of its largest to its smallest eigenvalue. As in this case the eigenvalues of interest are around the gap, σ must be as close as possible to the mid-gap in order to reduce the condition number and make possible to get eigenvalues from both sides of the gap.

We present examples of the application of TB to nanocrystals in the next sections, following the order of the calculated bulk band structures in the previous chapter.

2.2 II-VI Semiconductor Quantum Dots

Nanocrystals of II-VI semiconductors are widely studied because their synthesis is very well controlled . We start with a prototypical compound in its more common configuration.

2.2.1 CdSe Quantum Dots

The bulk properties of CdSe were already described in section 1.2.2 in its most common WZ configuration, as confirmed in experiments using colloidal synthesis[24]. CdSe quantum dots with a ZB structure are also syntethised using similar methods[25]. The values of bulk bandgap are not very different (1.85 eV for WZ and 1.78 for ZB at 0K), and the effect of spin orbit coupling gives the same values for the valence band splitting in both possible configurations[11]. In WZ-CdSe, the valence band at the Γ point splits into two 2-fold degenerate levels by the crystal field, while in ZB-CdSe there is a 4-fold degenerate level[8]. A deep description of the characteristics of ZB-CdSe quantum dots is not presented in this work, since we are interested only in reproducing its most general feature, the bulk bandgap, that is going to be useful for the description of the structures presented in chapter 3.

Spherical WZ CdSe nanocrystals were built with diameters from 1.0 nm up to 15.0 nm. For all dots built in this chapter, the ratio between number of anion atoms and cation atoms is intended to be 1 : 1 or at least close to that, something that can be done choosing correctly the origin of coordinates of the system, thus for large atoms, the number of one type of atoms compared to the other one does not differ in more than 5%. The effective diameter d of the dots is obtained comparing the expression of the volume of a sphere of that diameter and the volume of the structure, defined by the volume of the unit cell (V_{uc}) over the number of atoms n_{uc} contained in the unit cell (i.e. the effective volume of each atom), multiplied by the total number of atoms N:

$$d = 2 \times \left(\frac{3}{4\pi}\right)^{1/3} \times \left(\frac{N}{n_{uc}} V_{uc}\right)^{1/3}. \tag{2.4}$$

In WZ structure with cell parameters a and c the crystal lattice vectors are

$$\begin{aligned} \vec{a} &= a[1, 0, 0], \\ \vec{b} &= a[1, \sqrt{3}, 0]/2, \\ \vec{c} &= c[0, 0, 1]. \end{aligned} \tag{2.5}$$

The volume of the unit cell in the perfect lattice ($c = a\sqrt{8/3}$) is $V_{uc} = \vec{a} \times \vec{b} \cdot \vec{c} = \sqrt{2}a^3$, and as there are four atoms in the unit cell (two Cd and two Se atoms), Eq. 2.4 can be written as

$$d = 2 \times \left(\frac{3\sqrt{2}N}{16\pi}\right)^{1/3} a.$$

The surface dangling bonds of nanocrystals are saturated by pseudo-hydrogen atoms. As the diameter increases, the number of atoms also increases quickly, so above a diameter of about 6.0 nm a full diagonalization of the Hamiltonian was not possible and was restricted only to a limited number of states.

The variation of the energy of the highest occupied state and of the lowest unoccupied state, as function of the diameter can be well defined by analytic expressions[18]:

$$\begin{aligned} E_v^{CdSe}(d) &= E_v^{CdSe}(\infty) - \frac{1}{0.22573d^2 + 0.63567d - 0.13567}, \\ E_c^{CdSe}(d) &= E_c^{CdSe}(\infty) + \frac{1}{0.08292d^2 + 0.20721d + 0.33300}, \end{aligned} \tag{2.6}$$

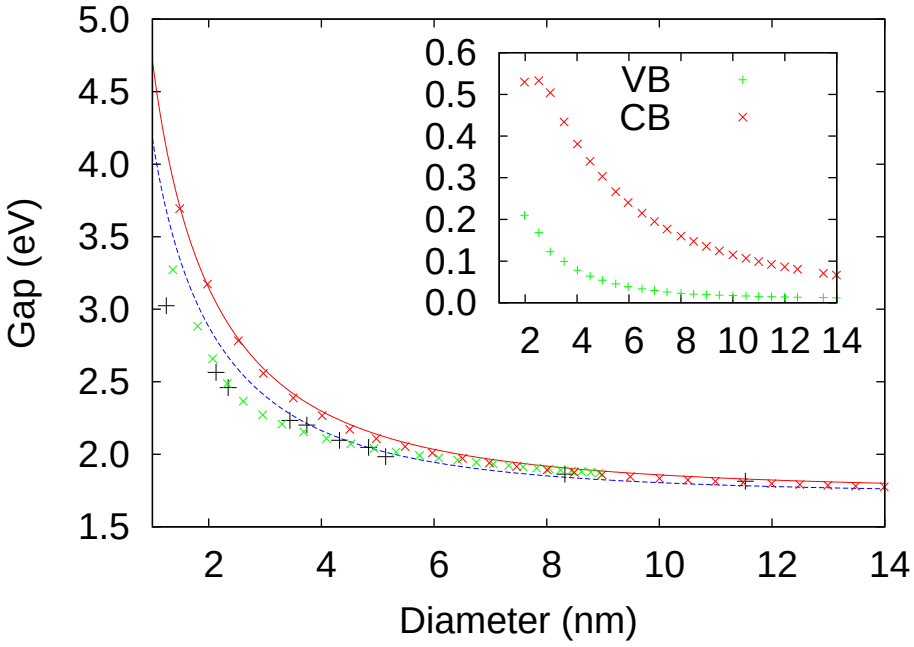

Figure 2.1: Gap versus diameter for WZ CdSe quantum dots. The calculated gaps (red ×) and the fitting from Eq. 2.6 (red line) show a good agreement with the data from Ref. [24] (+) and the fitting proposed from experimental data in Ref. [26] (green ×). The excitonic bandgap is included (blue). The inset shows the conduction and valence S-P splitting.

where $E_v^{CdSe}(\infty)$ and $E_c^{CdSe}(\infty)$ are the bulk band edges.

The calculated bandgap for different diameters of spherical WZ CdSe nanocrystals is plotted in Fig. 2.1, going a little further in size than the results shown in [9]. The curve, adjusted to the bulk bandgap at room temperature (1.73 eV for 300 K), shows a good agreement with the calculated excitonic gap [18], except for very small sizes, also with experimental data of Ref. [24] and the analytic fit obtained from experiments in Ref. [26]. The size variation of the energy gap in the analytic fits suggested in Refs. [26, 27] is mainly influenced by a term proportional to $1/d^2$, something that seems consistent with the predictions from the theory of confinement based in EMA, treated in section 1.3. Some discrepancy may come from the fact that WZ CdSe nanocrystals are not perfectly spherical but slightly prolate ellipsoids (ratio ~ 1.2). Another property that we can derive in this case is the behavior of the S-P splitting, illustrated in the inset of Fig. 2.1, calculated as the difference between the mean values of P states and S states in each band, defined according to the degeneracy mentioned at the beginning of this section. The associated values of energy are greater in the conduction band, with a fast decay to zero in the valence band for dots over $d = 7.0$ nm.

Now we apply the same methods to other structures.

2.2.2 CdTe Quantum Dots

Another example of II-VI compounds, CdTe nanocrystals take ZB structure, as in the case of bulk material. In this case, there are two atoms in the unit cell of volume $V_{uc} = a^3/4$, so Eq. 2.4 transforms into

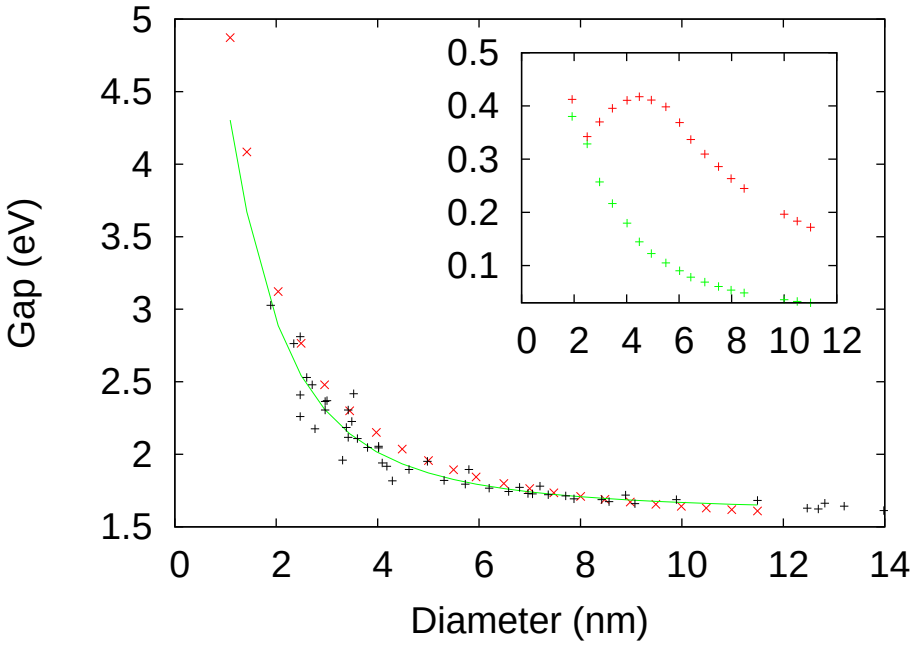

Figure 2.2: Calculated gap versus diameter for ZB CdTe quantum dots (red). The analytic fit (green) and the experimental data[27] used to adjust it (+) are included. The inset shows how the S-P splitting for the valence band (green) decreases quickly from values close to the ones of the conduction band (red).

$$d = 2 \times \left(\frac{3N}{32\pi}\right)^{1/3} a. \tag{2.7}$$

The parameters already used in section 1.2.2 (Table 1.2) correspond to the 0 K regime, so in Fig. 2.2 the displayed points correspond to the case of room temperature (300 K), assuming the same temperature dependence of the gap E_g(0 K) - 0.116 eV = E_g(300 K) as in the bulk.

We compare the calculated size dependence of the bandgap with experimental results of sizes up to 14.0 nm and the corresponding analytic fit of the experimental data[27]:

$$E_g^{CdTe}(d) = 1.596 + \frac{1}{0.137d^2 + 0.206}. \tag{2.8}$$

The agreement between the calculated results and the empirical fit is really satisfactory. The S-P splitting, as in the previous case, is greater for the conduction band than for the valence band, but the difference is not as large as in the case of WZ CdSe. The decay to zero at the valence band is more evident.

2.3 PbSe Quantum Dots

In its bulk configuration, PbSe has a narrow bandgap at L point but the effects of confinement are still more significant than in the II-VI semiconductors shown in section 2.2. As in all lead chalcogenides, PbSe is characterized by a large bulk exciton Bohr radius ($\sim$ 46 nm compared to 20 nm for PbS), which allows tuning of the bandgap and absorption edge across the near-infrared to the visible spectrum[28], starting from the bulk value up to values over 2.0 eV decreasing

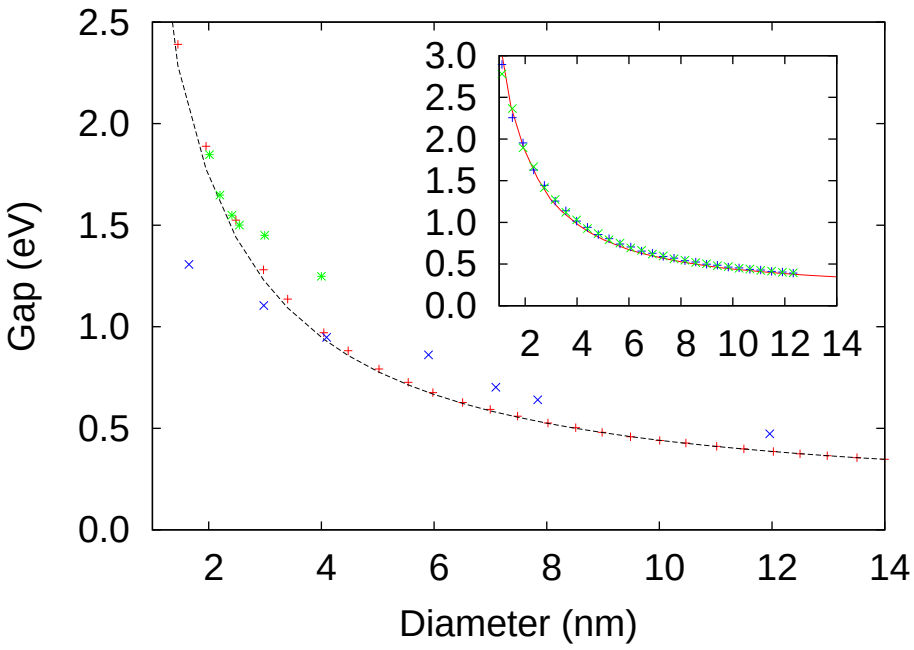

Figure 2.3: Bandgap versus size in spherical PbSe quantum dots: fit from Eq. 2.9 (dashed line) and calculated TB values (red +). Experimental values of Ref. [30] (blue ×) and Ref. [29] (green ×). The inset demonstrates that the gap for octahedrons centered on a Pb atom (blue) or a Se atom (green) is the same as for spherical dots (red curve).

the diameter of the nanocrystals. We have considered quantum dots with two different shapes, spheres and octahedrons with eight facets in the [111] directions, for reasons which will become clear in Chapter 3. The effective diameter of the octahedron is taken as the diameter of the sphere with the same volume. The surfaces are not passivated by pseudo-hydrogen atoms because there is no surface state for reasons discussed in Ref. [13].

The analytic relation between the energy gap (in eV) and effective diameter D (in nanometer) of PbSe nanocrystals, in analogy to Eq. 2.8, given by

$$E_g^{PbSe}(D) = E_g(\infty) + \frac{1}{0.0105D^2 + 0.2655D + 0.0667}, \tag{2.9}$$

with $E_g(\infty) = 0.176$ eV for the bulk bandgap, shows $1/D$ dependence relative to the size, then effective masses are not relevant quantities to give a description of the effects of quantum confinement in PbSe nanostructures[13].

The variation of the gap versus the size of the spherical and octahedral dots is shown in Fig. 2.3. There is a reasonable agreement with the early experimental results from Refs. [29] and [30] taking into account their large dispersion. The analytic fit from Eq. 2.9 is also included. The inset shows the gaps for two different types of octahedral nanocrystals, which are in very good agreement with the values for spherical nanocrystals.

A different analytic expression, very similar to Eq. 2.9, was suggested in Ref. [31], based on the same experimental data of Refs. [29, 30], and their own results. Recently, the synthesis of "small" dots, with diameter between 1-3 nm, was demonstrated[28]. A new analytic fit was suggested in Ref. [32], gathering an important group of measurements, and taking into account the small dots. The two analytic curves from Refs. [31] and [32] are compared with our calculations in Fig. 2.4a, showing that both fits correspond very well with our results, especially

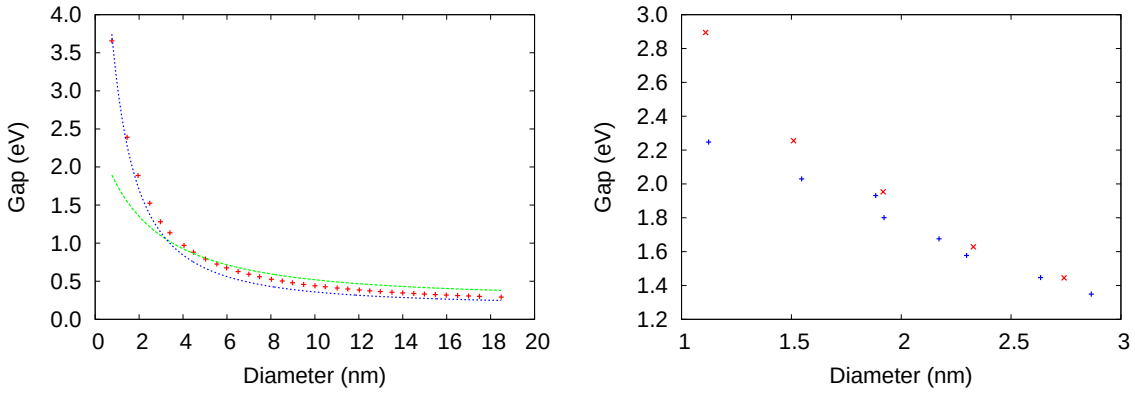

(a) (b)

Figure 2.4: Energy gap versus size of PbSe quantum dots. **(a)** The analytic expressions from Refs. [31] (green) and [32] (blue) adjusted on experimental data show good agreement with our calculations (red +). **(b)** Comparison between the results reported for small crystallites in Ref. [28] (blue +) and our calculations for octahedrons (red ×).

the most recent one, that takes into account very small dot sizes. We include in Fig. 2.4b a comparison between our calculations for octahedrons and the results reported by Ma et al.[28] for PbSe quantum dots with sizes from 1.0 to 3.0 nm. The agreement is good, except for very small crystals containing just few atoms. The selection of the octahedral instead of the spherical shape is based on observations of small PbSe particles[33].

PbSe is characterized by an eightfold degeneracy of conduction-band and valence-band valleys at the L point of the Brillouin zone, as predicted by EMA. However, the lowest (highest) S electron (hole) level in quantum dots is not eightfold degenerate due to so-called inter-valley couplings, i.e., the couplings between states are not constant, but oscillatory functions of size, depending strongly on the boundary conditions[34]. Figure 2.5 shows that the resulting inter-valley splittings in the manifold of the eight S states are non-negligible for small dot sizes. Inter-valley couplings also split the 24 (3×8) P states[13]. The average splitting between the S and P states is also shown in Fig. 2.5. In contrast to CdSe and CdTe quantum dots, the S-P splitting is almost the same for electrons and holes because valence and conduction bands are quite symmetric in PbSe.

Conclusions

We have presented TB electronic structure calculations on quantum dots of three different compounds (WZ CdSe, ZB CdTe and RS PbSe), reproducing with success the relation between bandgap and size of the nanocrystals, compared to experiments. The size ranges force us to apply minimization techniques to calculate just a few number of states for large structures, and the validity of the results demonstrates the efficiency of these techniques.

In the case of PbSe, the agreement between theory and experiments is obtained for a very wide range of sizes (1.5 - 14 nm) and energy gap (0.3 - 2.2 eV)

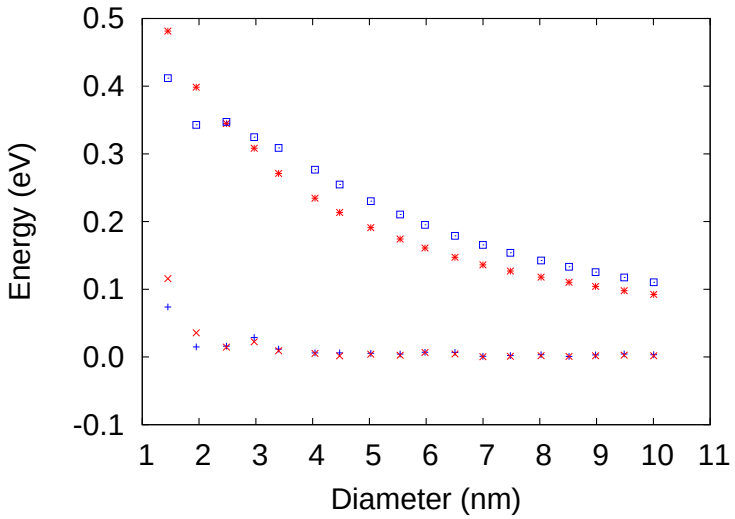

Figure 2.5: Intervalley coupling of S states (blue +: valence band, red ×: conduction band) and S-P splitting (blue □: valence band, red ∗: conduction band) in spherical PbSe quantum dots. The S-P splitting is expressed as the difference between the mean energy of the 8 S states and of the 24 P states.

Chapter 3

PbSe/CdSe Core/Shell Quantum Dots

Amongst the systems that became relevant in the framework of the Herodot network, the PbSe/CdSe core-shell quantum dots received special attention. They are heterogenous structures, composed by a RS IV-VI semiconductor core and a ZB II-VI semiconductor shell, both of them derived from fcc lattices. The lattice mismatch is very small, and this fact is the starting point for the construction of the structure as we can use exactly the same cell parameter for the whole structure, to be modeled with core and shell sharing a common fcc lattice of Se atoms. The growth of a CdSe shell over PbSe nanocrystals, very sensitive to ambient conditions, is useful to gain structural stability, and increases the probability to keep confined the charge carriers in the core. Relevant synthesis techniques are epitaxial precipitation and cation exchange, starting from the PbSe core.

After the introduction, briefly describing the reasons and methods to obtain core/shell quantum dots, in section 3.2 we describe the structural properties and parameters, based on the observed shape and type of interfaces between the core and the shell.

Section 3.3 is dedicated to the electronic structure calculations, showing the connection with the quantum dots of PbSe just presented in the previous chapter, including a brief discussion about the band offset, still unknown, given the scarce bibliography on the topic and the limitations of analytical techniques to its determination.

3.1 Introduction - Core/Shell Quantum Dots

Heterogeneous quantum dots deserve great attention for the modeling of electronic structure and optical properties. The compounds involved in such heterostructures can share structural properties to a greater or lesser extent, for example, having both one common type of atom (anion or cation) and exactly the same crystal structure, or as in the case to be treated in this chapter, different crystal structure with a common primitive lattice.

Under ambient conditions, many types of semiconductor quantum dots (especially lead chalcogenides) exhibit photochemical instability, with effects such as rapid oxidation of the nanocrystals and photoluminescence quenching when exposed to air[35]. To improve the stability and/or to enhance the photoluminescence (PL) quantum yield of a variety of quantum dots, overcoating them by a wider bandgap semiconductor material has become a successful strategy, yielding a core/shell hetero-nanocrystal usually with type-I band alignment [3].

The growth of a shell reduces surface degradation of the core and removes surface defects,

responsible for undesired emission quenching. But after the creation of the shell, defects can appear from strain caused by a large lattice mismatch between the core and the shell semiconductor materials, and they will act as trap sites for the charge carriers. Then it is evident that the selection of the semiconductor material for the shell has to take into account that the lattice mismatch between core and shell materials has to be small. Furthermore, the band offsets between the core and shell regions should be sufficiently high to assure that carriers are confined into the core region[36].

Lead chalcogenide quantum dots are more sensitive to heating in solution than, for example, CdSe quantum dots[37], then the growth of a shell is more difficult than in systems combining two II-VI compounds, where it is possible to use precursors from both the shell cation and anion. A good alternative to overcome that problem is in cation exchange reactions at lower temperatures (below 150 ℃), achieved through the introduction, for the present case, of a slow-reacting Cd precursor in excess compared to Pb in the original core, leading to controlled substitution of Pb atoms by Cd atoms[3, 38, 39], although control of the shell thickness may not be easy[40]. Another type of synthesis is solid source molecular beam epitaxy, starting from 2D RS type layers deposited over a cation[1]-stabilized buffer at low temperature and then converted into nanocrystals by annealing in an inert gas atmosphere[41, 42].

The inclusion of the core improves the thermal stability, demonstrated by the conservation of shape and size of the system, compared to the plain-core nanocrystals. However, an interesting effect appears upon thermal annealing under high vacuum ($T \geq 150$ ℃ and pressure 10^{-7} mbar or even lower)[43]. The number of atoms in each nanocrystal stays constant, also preserving their spherical shape, but the originally concentric core/shell structure is transformed, the shell component migrates to one side of the dot, leading to bi-hemisphere dimer heterogenous nanocrystals. Each hemisphere keeps its original crystalline structure, and the resulting dots show a preferential interface in [111] direction, which is also privileged in the core-shell synthesis, as discussed in the next section.

3.2 Description of the System

In sections 1.2.2 and 2.2.1 we treated CdSe in the WZ structure, as it is the most common disposition that appears for the bulk and individual nanostructures. It was also mentioned that ZB CdSe quantum dots can be synthesized with similar methods as those used for the synthesis of WZ nanocrystals. Growth of a CdSe shell over PbSe nanocrystals by cation exchange does not alter the total quantum dot size[38], and the CdSe shell exhibits ZB structure.

RS and ZB structures come both from fcc lattice, and as the bulk lattice parameters of PbSe and ZB CdSe have a small mismatch ($\sim 1\%$)[38], therefore we assume the same cell parameter value a for the whole structure. The system for the calculations is built defining first a common Se fcc lattice, then introducing the $[100]\,\frac{a}{2}$ displaced Pb fcc lattice and $[111]\,\frac{a}{4}$ displaced Cd lattice in the regions defining respectively the core and the shell. The same procedure is used for the construction of any other type of RS-ZB structure.

Experiments of high-resolution transmission electron microscopy (HRTEM) and high-angle annular dark-field scanning transmission electron microscopy (HAADF-STEM) show that the core tends to form facets oriented in the [111] direction, taking the shape of an octahedron[43, 44], and keeping the spherical shell as shown in the model of Fig. 3.1a. The projections along [110] and [001] axes, with the HRTEM images along the corresponding axes of PbSe, are shown in Fig. 3.1b. We include an HRTEM image in Fig. 3.1c to show the change in the disposition

[1] For the ZB structure.

of the heteronanocrystals after annealing the PbSe/CdSe core/shell system in high vacuum, taking the shape of a dumbbell, with hemisphere interfaces formed by Se [111] planes[43]. The sharp edges in the TEM images from Fig. 3.1b help to exclude other [110] or [001] planar interfaces, that can be identified in PbTe/CdTe core/shell nanocrystals synthesized by the same cation-exchange methods[45–47]. Based on these results, the core is built with the shape of a regular octahedron, which has the eight facets oriented in the [111] direction and the equivalent conjugate planes, without truncating the junctions between them, so those [111] facets are the only planar interfaces with the shell (otherwise there could be also interfaces in the [001] or [110] directions, and the core should have the shape of the first Brillouin zone for fcc structure). As in section 2.3, it is possible to control the core surface, choosing to be composed by planes of just Pb (Pb-terminated interface) or Se (Se-terminated interface) atoms. This assumption does not assure that all interfaces are equivalent, in part due to the asymmetric disposition of the ZB structure regarding the $[\bar{1}\bar{1}\bar{1}]$ direction compared to the [111] direction, and due to the fact that we do not consider any relaxation of the surface.

The (111) surfaces, both in RS and ZB systems are polar, terminated by planes formed by anions or cations. A difference between them is induced by the asymmetry of the ZB structure, as it is not possible to reconstruct the same anion or cation terminated (111) surface if we look in the conjugate $[\bar{1}\bar{1}\bar{1}]$ direction. The next step is the description of the possible types of interfaces in the core/shell system.

3.2.1 Interfaces of RS-ZB Heterostructures

Theoretical and experimental works on RS-ZB interfaces[46–48] show that in the [111] and [001] directions, there are two non-equivalent configurations at the interface, whereas in the [110] direction, there is a single type of interface. The interfaces in the [111] direction show a better stability, compared to the other two directions, in terms of interface energies calculated by *ab initio* methods[46]. Therefore, and for the reasons discussed above, we have only considered nanocrystals with [111] interfaces in the present work. The way to build the quantum dots in this work makes possible that there appears a third type of [111] interface, feasible from the theory, but possibly not allowed in the real system. In the following, we describe these three types of [111] interfaces.

The first case, that we will call hereafter type-1 interface (we will use numbers to avoid confusion with the notation for the band alignment), corresponds to an interface between Pb-terminated (as seen from the RS structure) and Se-terminated (as seen from the ZB structure). Each Se atom from the first ZB interface plane has one Cd atom as nearest neighbor, at $[111]\,\frac{a}{4}$ and three Pb atoms at $[\bar{1}00]\,\frac{a}{2}$, $[0\bar{1}0]\,\frac{a}{2}$ and $[00\bar{1}]\,\frac{a}{2}$, acting also (from the point of view of the RS region) as first nearest neighbors of the Se atom. The separation between Pb and Cd atoms is larger than both nearest neighbor distances from ZB or RS structure, so core and shell zones are well identified in this case, as shown in Fig. 3.2a.

In the type-2 interface, illustrated in Fig. 3.2b, there is a Se-terminated (RS) and Cd-terminated (ZB) interface, the Se atoms in the RS interface plane have three Cd atoms as neighbors in the directions $[11\bar{1}]\,\frac{a}{4}$, $[\bar{1}11]\,\frac{a}{4}$ and $[1\bar{1}1]\,\frac{a}{4}$ and three Pb atoms in the directions $[\bar{1}00]\,\frac{a}{2}$, $[0\bar{1}0]\,\frac{a}{2}$ and $[00\bar{1}]\,\frac{a}{2}$, as in the first case. This is a particular situation, since at each side of a Se plane the first planes of Pb and Cd are aligned in the [111] direction in such way that the atoms are at distance $\frac{\sqrt{3}}{4}a$, i.e. the nearest neighbor distance for the ZB structure. The TB parameters between the Pb and Cd atoms in those planes are not considered.

In both cases, we can identify a plane of Se atoms at the interface, belonging to any of the two regions as it is actually impossible to define to which compound corresponds originally the

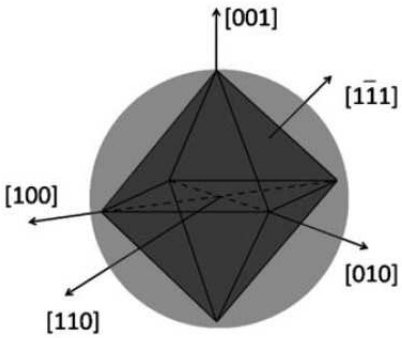

(a)

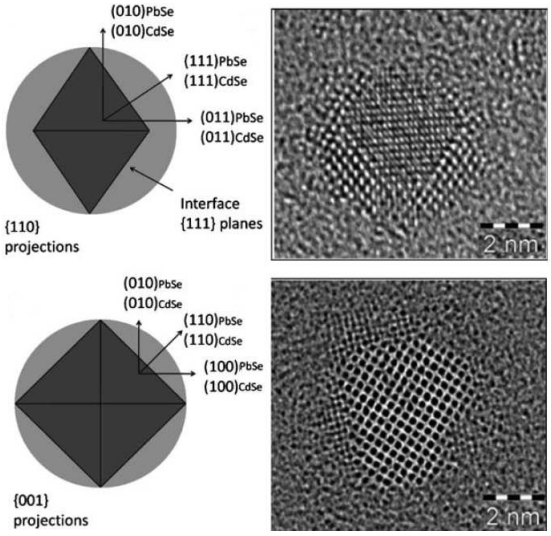

(b)

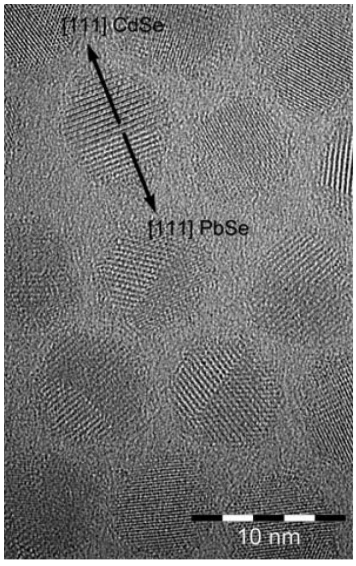

(c)

Figure 3.1: **(a)** Model for the core and shell shapes in PbSe/CdSe heteronanocrystals. **(b)** Projections along [110] and [001] axes in HRTEM, showing the [111] facets at the interface. **(c)** After annealing in high vacuum, the size of the nanocrystals is not affected, but they turn into dumbbells, with interfaces oriented in the [111] direction[43].

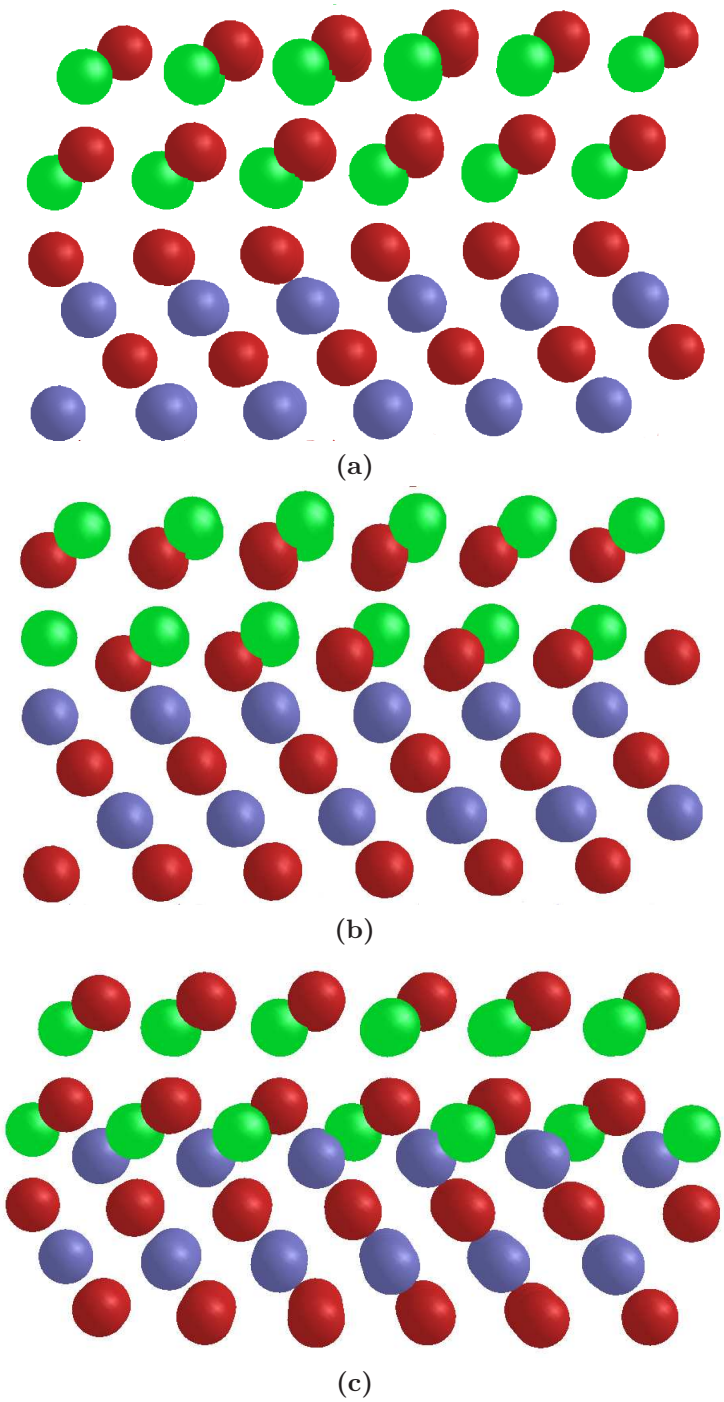

Figure 3.2: PbSe/CdSe interfaces in the [111] direction. Se atoms are in red, Cd and Pb are in green and blue, respectively. **(a)** Type-1: the RS region is Se-terminated, and the ZB is Cd-terminated. **(b)** Type-2: RS Pb-terminated and ZB Se-terminated. **(c)** Type-3: RS is Pb-terminated and ZB is Cd-terminated.

Se plane. The differences in stability between the two cases in question are studied in Ref. [46] for PbTe/CdTe superlattices, using an *ab initio* pseudopotential method. Across the interface, it is shown that there are partially covalent bonds between the Te and Cd atoms at the ZB side of the interface, and ionic bonds between the same Te atom and the neighbor Pb atoms at the RS side, i.e., the interfaces in the [111] direction keep the character of the bonds from each independent bulk compound[2]. Atomic displacements after structural relaxation are normal to the interface, with more significant effects in the type-2 (ZB Cd-terminated) than in the type-1 (ZB Se-terminated). Therefore, the latter exhibits bulk-like behavior in its geometry, and likely a higher stability. We assume that the same conclusions are valid for the PbSe/CdSe interface. Atomic relaxation is thus neglected in our model.

Between two facets of the second type, it is still possible to find a third type of interface, Pb-terminated (RS) and Cd-terminated (ZB), illustrated in Fig. 3.2c. It can be seen as a Cd layer which is extended inside the RS region. The situation of the neighbors here is more complicated, since each Pb atom at the interface is surrounded by six Se atoms (nearest neighbors in the original RS structure) and three Cd atoms in the directions [100] $\frac{\sqrt{3}-2}{4}a$, [010] $\frac{\sqrt{3}-2}{4}a$ and [001] $\frac{\sqrt{3}-2}{4}a$, at a distance $\frac{1}{4}\sqrt{7-2\sqrt{3}}a < \frac{a}{2}$, i.e. slightly less than the nearest neighbor distance for the RS structure. In a reciprocal way, each Cd atom has three Pb atoms at the same distance (greater than the nearest neighbor distance for ZB structure) in the corresponding conjugate directions. This type of interface does not seem to be chemically allowed. However, we have kept the nanocrystals presenting this type of interface into consideration. We remind that, in our model, we do not consider the parameters between Pb and Cd atoms, which is clearly an approximation. In these conditions, we will show in the following that the nanocrystals with type-3 interfaces do not behave differently from the others.

In the following, we study the variation with size of the electronic structure of PbSe/CdSe quantum dots. We do not select any specific interface type and any specific termination of the core surface when we build them. The first interface appears as the only interface type in about 35% of the dots. The type-2 interface appears always combined with the type-1, and in about 30% of the cases, simultaneously combined with type-3 interfaces.

3.2.2 Shell Thickness

The next parameter to control is the thickness of the CdSe shell. Measured absorption spectra of PbSe/CdSe quantum dots during the cation exchange show an increasing blueshift with exchange time[49]. The explanation can be related with the shrinking of the PbSe core and the simultaneous increase in the shell thickness. The usual measured values for the thickness go from ~ 0.4 nm to ~ 1.5 nm[38].

To measure the shell thickness, HRTEM can be used (Fig. 3.1b). The thickness could be defined as the distance from the edges of the octahedral core, along the [110] or [011] directions, to the shell surface. However, although the boundary between the two regions can be distinguished, it is not straightforward to say if it corresponds to a cation or anion plane. Moreover, this technique cannot analyze a large number of samples in short times[49]. A useful approach is presented in Ref. [49], based on the measurement of the non-stoichiometric Pb/Se ratio of the original PbSe core quantum dots[31] and of the derived PbSe/CdSe quantum dots. As the Se-content remains constant, it is possible to determine the amount of Pb in the core/shell nanocrystal, setting the stoichiometry of the new core equal to the stoichiometry of a PbSe

[2]It is not the case in some specific disposition at the interface oriented in the [100] direction, which we do not take into account here.

dot containing the same amount of Pb, for which it is assumed that the core is terminated by Pb-planes[31], i.e., the interfaces correspond to the first case of the previous section (Fig. 3.2a).

In the creation of the system for the TB calculations, we set initial values for spherical core and shell radii, and the shell thickness is first defined as the difference between them. The sphere is circumscribed to an octahedron which defines the core shape. If R_{sph} is the radius of the initial sphere, the edge length of the octahedron is $l_{oct} = \sqrt{2}R_{sph}$, and its volume is

$$V_{oct} = \frac{1}{3}\sqrt{2}l_{oct}^3 = \frac{4}{3}R_{sph}^3 = \frac{V_{sph}}{\pi}. \tag{3.1}$$

Therefore, when the core is limited to its final octahedral shape, the volume is strongly reduced and the shell thickness is obviously not homogeneous. For the sake of comparison between the different nanocrystals, we define as in section 2.3 the effective diameter of the core as the diameter of a sphere with the same volume. Similarly, we define the effective thickness of the shell as if it was a (hollow) spherical shell with the same volume. The initial radii for spherical core and shell are defined such that the effective thickness is equal to 0.5 nm and 1.0 nm for a thin and a thick shell, respectively. Values lesser than 0.5 nm are not convenient for the calculations, since under those conditions the small regions between each vertex of the octahedron and the dot surface present defects.

Now that we have defined the structural properties of these heteronanocrystals, we can go to the description of their electronic structure.

3.3 Electronic Structure Calculations

ZB and WZ CdSe have a bandgap at Γ-point, but valence band structure show some relevant differences at the same Γ-point: the ZB-CdSe has a 4-fold degenerate valence band, while the crystal field in WZ-CdSe splits the valence band into 2-fold degenerate levels[8, 50]. Early attempts to compare the electronic structure of WZ and ZB-CdSe nanocrystals using tight-binding[51] and empirical pseudopotentials[52, 53] conclude that there are minor differences in the sizing curves (gap versus size).

TB parameters for ZB-CdSe can be found Refs. [11, 20, 54–57]. Most of these parameters, usually restricted to a sp^3 basis, yield similar values for the bulk bandgap at 0K, not far from the reported experimental values[8], although the spin-orbit coupling and its corresponding splitting are not taken into account in all the references. High-energy conduction bands are not very well described with these parameters, but we believe that the are sufficient for our purpose here which is just to describe CdSe as a barrier material.

Table 3.1 shows the parameters that we have considered in this work as a combination between first nearest neighbor parameters in a sp^3s^* basis for the shell[11], and a $sp^3d^5s^*$ basis for the core[13], as in sections 1.2.2 and 2.3. The on-site parameters for the d orbitals in CdSe are taken with large energy values, the parameters of interaction between Pb and Cd atoms are neglected, and no relaxation is considered at the interface. The passivation with H atoms is needed for the dangling bonds at CdSe surface.

We have still to discuss an important parameter of the calculations, the band offset at the interface between the two materials.

3.3.1 Valence Band Offset

We already gave some description of the possible types of band alignments in the Introduction of this thesis. It defines the localization of the electron and the hole wave function. For a type-I

Intra-atomic terms 1 (Pb) and 2 (Cd)	
$E_s1 = -5.07781$ eV.	$E_S2 = 0.03000$ eV.
$E_p1 = 4.33168$ eV.	$E_p2 = 4.73000$ eV.
$E_d1 = 10.97439$ eV.	$E_d2 = 100.00000$ eV.
$E_{s*}1 = 24.35922$ eV.	$E_{s*}2 = 5.72000$ eV.
$SO1 = 0.55000$ eV.	$SO2 = 0.05910$ eV.
Intra-atomic parameters atom 3 (31: Se in PbSe, 32: Se in CdSe)	
$E_s31 = -11.45405$ eV.	$E_s32 = -9.63000$ eV
$E_p31 = -1.47533$ eV.	$E_p32 = 1.32600$ eV
$E_d31 = 12.13125$ eV.	$E_d32 = 100.00000$ eV.
$E_t31 = 17.60374$ eV.	$E_{s*}32 = 7.53000$ eV.
$SO3 = 0.24000$ eV.	$SO3 = 0.14340$ eV.
Hydrogen parameters atom 2 (Cd) and 3 (Se)	
$E_H = 0.56004$ eV.	
$VH_{SS} = -35.69727$ eV.	
$VH_{PS} = 61.82948$ eV.	
1st nearest neighbors parameters PbSe	
$V_{ss\sigma}13(1) = -0.36267$ eV.	$V_{ss^*\sigma}13(1) = -1.29525$ eV.
$V_{sp\sigma}13(1) = 1.31029$ eV.	$V_{ss^*\sigma}31(1) = -1.12089$ eV.
$V_{sp\sigma}31(1) = 1.20593$ eV.	$V_{ps^*\sigma}13(1) = -2.51117$ eV.
$V_{sd\sigma}13(1) = -1.71725$ eV.	$V_{ps^*\sigma}31(1) = -2.27510$ eV.
$V_{sd\sigma}31(1) = -0.83693$ eV.	$V_{ds^*\sigma}13(1) = -0.92754$ eV.
$V_{pp\sigma}13(1) = 1.71542$ eV.	$V_{ds^*\sigma}31(1) = 0.18794$ eV.
$V_{pp\pi}13(1) = -0.38235$ eV.	$V_{s^*s^*\sigma}13(1) = -0.93835$ eV.
$V_{pd\sigma}13(1) = -2.13886$ eV.	$V_{pd\sigma}31(1) = -1.07458$ eV.
$V_{pd\pi}13(1) = 0.73701$ eV.	$V_{pd\pi}31(1) = -0.14844$ eV.
$V_{dd\sigma}13(1) = -0.27384$ eV.	$V_{dd\pi}13(1) = 1.48923$ eV.
$V_{dd\delta}13(1) = -0.35624$ eV.	
1st nearest neighbors parameters CdSe	
$V_{ss\sigma}23(1) = -1.16000$ eV.	$V_{sp\sigma}23(1) = 2.39889$ eV.
$V_{sp\sigma}32(1) = 1.97887$ eV.	$V_{pp\sigma}23(1) = 3.34000$ eV.
$V_{pp\pi}23(1) = -0.68000$ eV.	
$V_{ps^*\sigma}23(1) = 1.32069$ eV.	
$V_{ps^*\sigma}32(1) = 1.07820$ eV.	
Electronic charges in bulk (number of electrons)	
Q1 = 2.839782	
Q2 = 2.346022	
Q31 = 7.160218	
Q32 = 5.653978	

Table 3.1: Tight-binding parameters for PbSe/CdSe core/shell nanocrystals. The Pb(1), Cd(2) and Se(3) TB parameters are extracted from Refs. [11] and [13] for ZB CdSe and RS PbSe, respectively. Between Pb and Cd atoms there is no interaction, so all the parameters are null. To illustrate the difference in ionicity between the two compounds, we include the relative electronic charges, expressed in number of electrons, calculated in the bulk.

alignment, electron and hole are confined together either in the core or in the shell, and spatially separated if it is a type-II alignment. For the intermediate case, the quasi-type-II, one carrier is localized in one region, while the other is fully delocalized over the entire volume (Fig. 2). The large difference between bulk bandgaps of PbSe and CdSe makes this system to be more suitable to type-I alignment, but there is no clarity on the actual situation.

We can give some examples of measured and calculated band offsets in PbTe/CdTe. Measured values through different techniques in the [111] direction for PbTe/CdTe show reasonable agreement between them, as the valence band offset (VBO) is $\Delta E_v = 0.135 \pm 0.05$ eV using X-ray photoelectron spectroscopy[58], and $\Delta E_v = 0.09 \pm 0.12$ eV from ultraviolet photoelectron spectrum using synchrotron radiation[59]. But *ab initio* calculations without taking into account spin-orbit coupling[60, 61], give much larger values for the PbTe/CdTe [110] (0.42 eV) and [100] (0.37 eV) interfaces, although the inclusion of the coupling diminishes the VBO almost to zero[59]. Moreover, we must remind that DFT methods also underestimate in a significant way the bandgap values (Ref.[47], E_g(CdTe) = 0.34 eV), so calculations of the VBO should be reviewed carefully.

It is clear that the determination of the band offsets is not an easy task for this type of heterostructures. In Ref. [62], self-consistent TB calculations have been successfully used to study the VBO at GaAs/AlAs interfaces, in planar superlattices or in more complex heteronanostructures. We have tried to apply the same method to PbSe/CdSe without success, the

selfconsistency could not be reached. We have dealt with many difficulties, due to the asymmetric disposition of the interface planes in the construction of the superlattices, and to the significant difference of net charge at each side of the interface[46], due to the strong ionicity of PbSe (and in general of lead chalcogenides)[63, 64], compared to CdSe.

We must resort then to experimental values of the band offset, but we could find two values for the VBO in PbSe/CdSe interfaces. The first one[49] gives a type-I band alignment with a VBO of 0.78 eV between bulk PbSe and CdSe. A recent estimation of the VBO, as part of the experimental work within the Herodot network, using Ultraviolet Photoelectron Spectroscopy directly in PbSe/CdSe quantum dots[65], shows a different value, about $\Delta E_v = 1.1$ eV, again with type-I alignment. The following calculations used mainly the second value. The results obtained with the first value will be presented later.

3.3.2 Construction of Core/Shell Quantum Dots

We already described in section 3.2 the starting point for the construction of the system, using a common Se fcc-lattice for both core and shell. The criterion to define the core and the shell diameters was introduced in section 3.2.2. The size increases in steps of 0.5 nm as function of the diameter of the circumscribed sphere.

To assure the obtaining of an octahedral core, an atom (whether Pb or Se) is located at the origin of coordinates, then it is surrounded by its six first nearest neighbors, vertex of the smallest octahedron that we can construct. The first recognizable (111) planes appear after the inclusion of a new layer of atoms, as illustrated in Fig. 3.3a, where we start from a Se-centered octahedron. The procedure is continued to get the desired octahedral core (Fig. 3.3b) and after that, extending the same Se lattice up to the diameter of the shell, as shown in Fig. 3.3c where no Cd or H atoms are displayed. It is possible to identify the (111) planes of Se atoms in the shell. Evidently, the ratio between the Pb and Se atoms in the core is far from being 1:1, as in the construction of spherical core nanocrystals in the previous chapter.

We control only the type of atom at the origin, but we do not get preferential termination at the surface, then a Se-centered core results into Se-terminated and Pb-terminated surfaces more or less in the same proportion, and it has no direct effect to select the type of interfaces with the CdSe shell. We then obtain different types of interfaces in the proportion already mentioned at the end of section 3.2.1.

3.3.3 Electronic Structure

The electronic structures of two PbSe/CdSe dots, Se-centered and Pb-centered, with a core of ~ 4.5 nm, and of the equivalent spherical PbSe dot are shown in Fig. 3.4. The difference between the two core/shell dots is also in the interface planes, Pb-terminated combining the type-1 and type-2 interfaces for the Pb-centered core, and Se-terminated with interfaces of the type-1 (Fig. 3.2a), for the Se-centered core. The bandgap is approximately the same as for the PbSe quantum dot in both cases, with no significant shift in the band edges. A manifold of eight states is found for the lowest (highest) conduction (valence) states. As already discussed in Chapter 2, they arise from the eightfold degeneracy of the conduction (valence) band extrema in PbSe. In quantum dots, the degeneracy is slightly lifted due to inter-valley couplings. The inter-valley splittings seem to be larger in core/shell quantum dots, in particular for valence states. It was shown in Ref. [34] that inter-valley couplings are very sensitive to the boundary of quantum dots, thus to their capping (if there was no boundary like in bulk PbSe, there would be no coupling). Therefore it is not surprising that the presence of a shell influences these

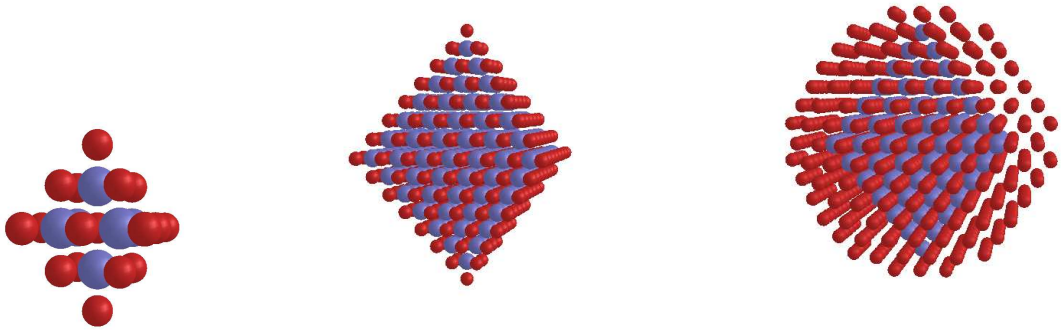

(a) **(b)** **(c)**

Figure 3.3: The construction of the octahedral core is done locating an atom (in this case, Se) at the origin of coordinates, then "growing" alternated layers of Pb and Se up to the desired core radius, limited by (111)-like planes. In **(a)** is displayed the first recognizable (111) layer, for a core containing 6 Pb atoms and 19 Se atoms. The extension to the desired size, and how the original planes at the octahedron can still be seen when the Se lattice is extended until the shell surface is shown in **(b)** and **(c)**, respectively.

couplings.

The variation of the bandgap with the diameter of the core is shown in Fig. 3.5. The PbSe/CdSe dots with thick and thin shells are compared to the spherical and octahedral PbSe dots of the same diameter. It is clear that the value of the bandgap is completely dominated by the core, in agreement with the experimental results from [49], and therefore the role of the shell is limited to guarantee the stability of the confined system. It is important to mention that the type of interface does not affect these results, taking into account that for this size distribution, we are using indifferently dots that combine the different interface types, in the proportions already mentioned in section 3.2.1. The change of the VBO makes no important difference regarding the variation of the bandgap versus the quantum dot size, as seen in the inset of the same figure. Despite the difference between the two offsets (about 30%), in both cases we have a well defined type-I alignment, with offsets in all cases at least two times greater than the bulk bandgap of PbSe.

The inter-valley coupling and S-P splitting are shown in Fig. 3.6. Similar values are obtained for PbSe and PbSe/CdSe quantum dots, except for a small increase in the inter-valley splittings in the valence band. These results confirm that the electronic structure of PbSe/CdSe nanocrystals is totally governed by the core, a situation confirmed by experiments, where these calculations were used as a support[65].

Finally, we already mentioned the difference in the position of the bandgap in the k-space for the bulk compounds, at the Γ point for CdSe, and at the L point for PbSe. To evaluate if there is any effect due to that difference, we can check the localization of the states, calculating the weight of the wave functions (Eq. 1.2) on the atoms in the quantum dot.

In Fig. 3.7a we show the evolution with energy of the weight of the wave functions over the core, for an effective core diameter $\sim$3.15 nm and a shell effective diameter $\sim$4.67 nm. There is no important difference at first sight between electron and hole states, and it is evident that the

Figure 3.4: Electronic structures, first 40 states in the conduction band and valence band. From left to right, for PbSe, and equivalent PbSe/CdSe quantum dots with combined (type-1 and type-2) interfaces, and single type-1 interface, with core diameter $D \sim 4.5$ nm.

states closer to the bandgap are localized in the core, as a consequence of the type I interface. The weight starts to reduce in a significant (but not drastic) way just after reaching differences in energy comparable to the corresponding offsets in the valence band and the conduction band, leading to full delocalization of states. For high energy values, the weight is around the ratio between the volume of the core and the total volume, with greater dispersion of the distribution in the conduction band. In this case, the knowledge of the offset is important, to determine the mixing of states in the core or in the shell.

It is interesting to check if similar behavior occurs in other systems than PbSe/CdSe. We have thus considered the case of GaAs/AlAs core-shell quantum dots. Even if these systems have not been synthesized to the best of our knowledge, they are interesting for the following reasons. There is no problem of strain since GaAs and AlAs have very similar lattice constant. GaAs and AlAs are both characterized by valence band maxima at $k = 0$ (Γ point). In contrast, the conduction band minimum is at Γ in GaAs while it is at the X points in AlAs. GaAs has a smaller bandgap than AlAs (1.51 eV compared to 2.22 eV) and the interface is of type I. For the calculation of the electronic structure, we consider a $sp^3d^5s^*$ tight-binding model with the parameters of Ref. [66] and we follow the approach of Ref. [62]. In that case, the valence-band offset is equal to 0.447 eV, thus much smaller than in the case of PbSe/CdSe.

Figure 3.7b shows the evolution of the weight of each wave-function on the atoms of the core as function of the energy (core diameter = 1 nm; shell diameter = 2 nm). The deepest states (closest to the gap) are clearly localized in the core, as expected from a type I interface. But, very quickly, we see that at increasing absolute energy the weight decreases and reaches a

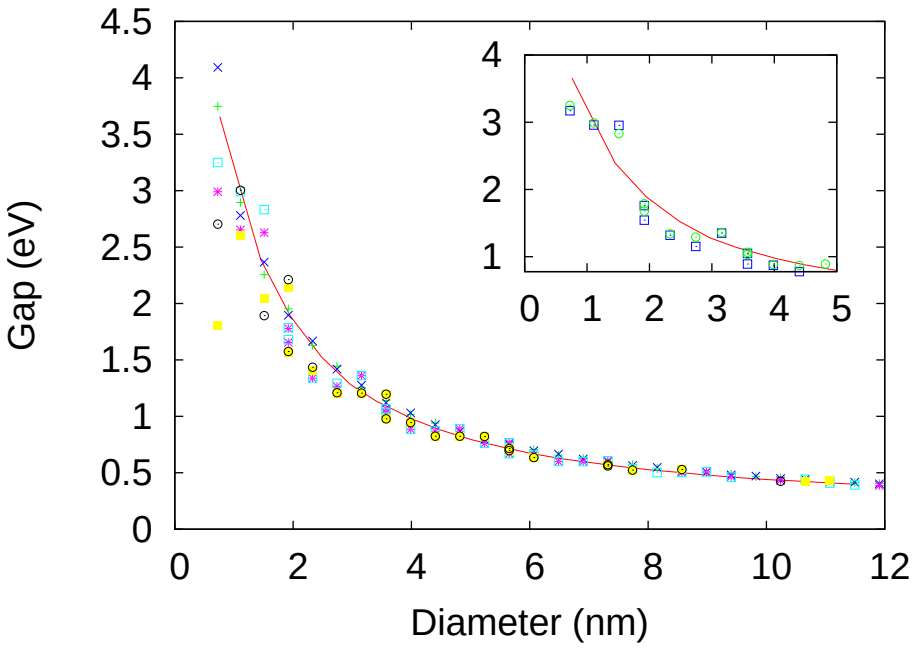

Figure 3.5: Bandgap versus Size for PbSe/CdSe nanocrystals. Dots centered in a Pb atom with thin (○) and thick shell (yellow □). Centered in a Se atom with thin (open, light blue □) and thick (purple ∗) shell. The octahedral PbSe nanocrystals, Pb-centered (green +) and Se-centered (blue ×) are included. The solid line corresponds to PbSe quantum dots. The inset shows the similarity between the results for the thin shell Se-centered PbSe/CdSe dots with VBO = 1.1 eV (green ○) and VBO = 0.78 eV (blue □).

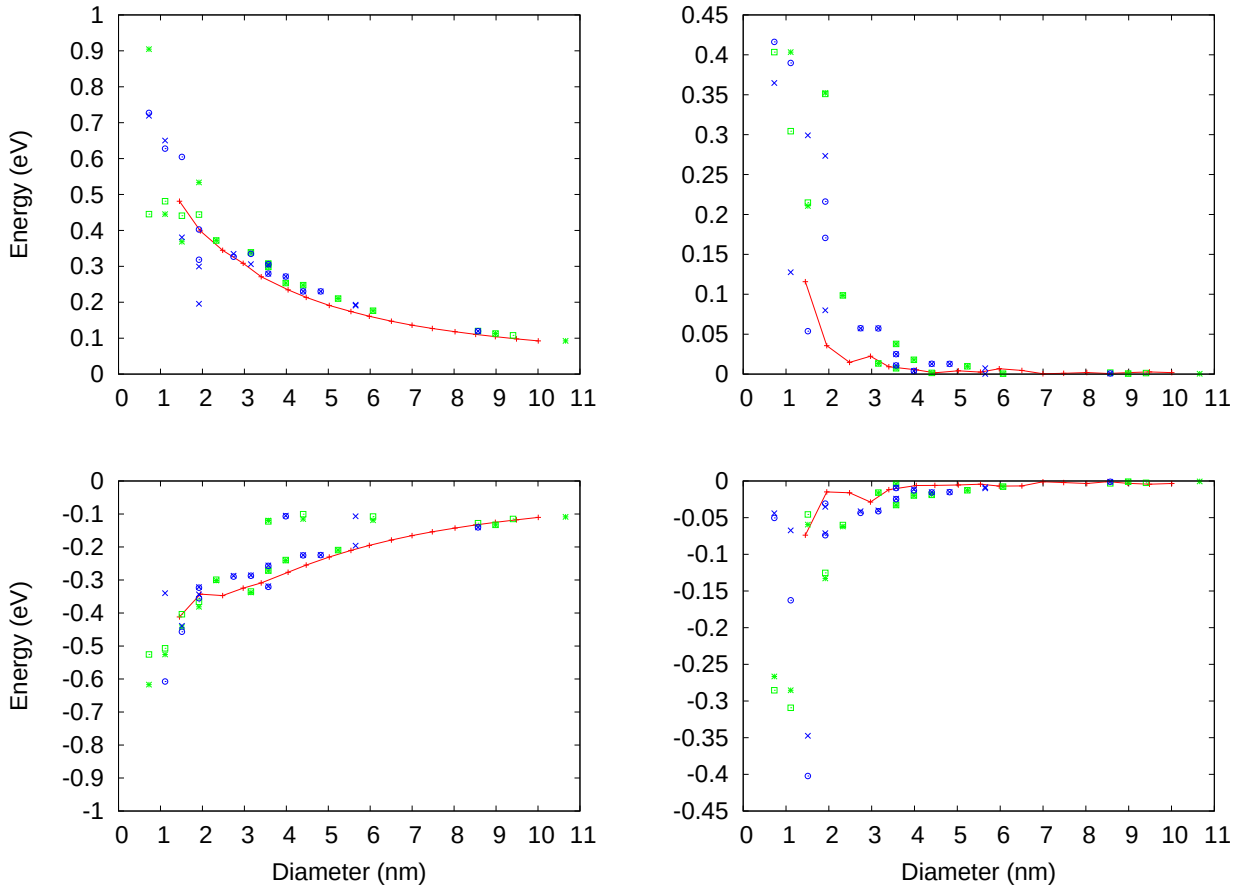

Figure 3.6: S-P splitting (plots in the left) and inter-valley coupling (right) as function of the core effective diameter for PbSe/CdSe quantum dots: Se-centered (green) and Pb-centered (blue), with thin ($*$ and $\circ$, respectively) and thick ($\square$ and $\times$) shells. Conduction band (top) and valence band (bottom). The negative values for the valence band plots are just a help to visualize them along with the values in the conduction band. The red points joined by a line correspond to the calculations for spherical PbSe quantum dots.

value close to 0.125 which corresponds to ratio between the volume of the core the volume of the shell. This result means that each state at high enough energy is fully delocalized in the quantum dot. We do not see a marked difference between the electron and the hole states, even if the minimum of the conduction is not as the same k-point in GaAs and AlAs. Therefore we conclude that in core-shell quantum dots, in the strong confinement regime, the states above the barrier are fully delocalized over the whole volume of the quantum dot, whatever is the position of the conduction-band minima and valence-band maxima in the k-space.

Conclusions

We presented TB calculations of the electronic structure in PbSe/CdSe quantum dots. We have considered first the difference in the crystalline structure, and second the possible types of interfaces derived from that difference. Experiments on HRTEM show that the core takes the shape of an octahedron inside a spherical shell, with interfaces in the [111] directions. These

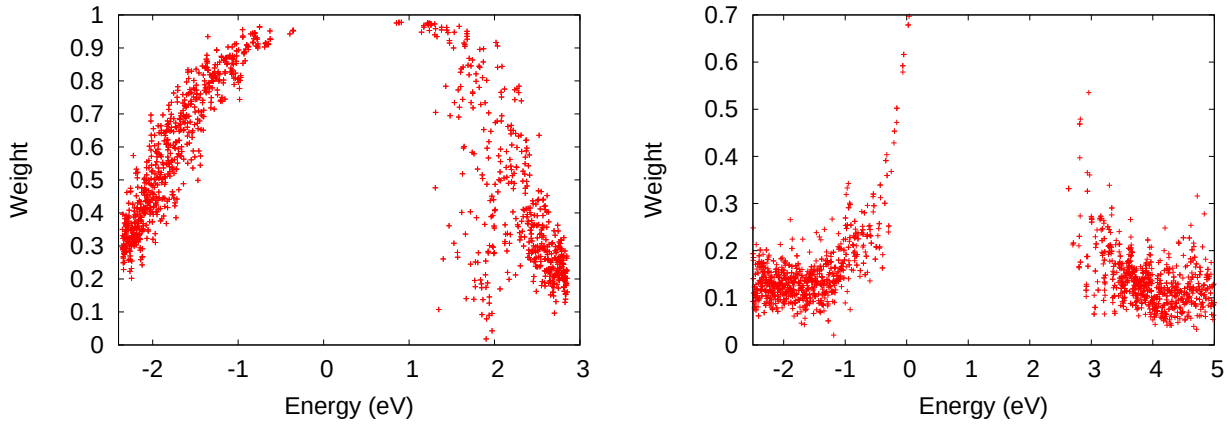

Figure 3.7: Weight of the wave-functions over the core versus energy for PbSe/CdSe **(a)** and GaAs/AlAs **(b)** core/shell quantum dots. A weight equal to 1 means that the wave-function is totally localized in the core.

polar surfaces show two possible configurations, due to the asymmetry of the ZB structure of the CdSe in the shell.

We apply a simple model, which takes the shell just as a barrier, due to the big difference between the bulk bandgaps of PbSe and CdSe. In consequence, we assume type I band alignment. The analytic estimation of the band offset deserves special work since there exists still some uncertainty about the value of the offset, and then we use the value obtained by collaborators in the Herodot network.

We are able to confirm that the electronic structure is governed completely by the PbSe core, with no relevant influence from the type of interface. Above the barrier imposed by the band alignment, we find full delocalization of states over the whole volume of the quantum dot. We compare our results with the same type of calculations in GaAs/AlAs core/shell quantum dots, where we can find similar behavior.

Chapter 4

Simulations on Induced Intraband Absorption

Optical spectroscopy techniques occupy a relevant place amongst the usual methods to probe electronic and vibrational processes in materials physics, chemistry and biology. For example, non-emissive states can be investigated efficiently using absorption spectroscopy, and, to study emissive states and their evolution, time-resolved fluorescence can be used. Absorption spectroscopy is a standard method to probe interband transitions in quantum dots. In this chapter, we consider transient absorption spectroscopy, which gives valuable information on intraband transitions. We apply the methods already introduced in section 1.4 to simulate spectra measured by means of these techniques. We study the nature of previously non-reported signals that can be associated with intraband photo-induced absorption.

Some general concepts, just mentioned in chapter 1, are commented briefly as an introduction of section 4.1, complemented by a short description of the general principle of transient absorption experiments and implementation of the absorption calculation method introduced in section 1.4.1.

The sections 4.2 to 4.4 present the results of the simulated optical properties in the quantum dots already treated in the previous chapters. For PbSe and PbSe/CdSe core/shell quantum dots, the calculations are compared directly with recent experimental results, which are described in more detail in the section dedicated to PbSe nanocrystals. For the case of the II-VI quantum dots discussed in section 2.2, the calculations predict a group of intraband transitions which have not been experimentally revealed so far.

4.1 Introduction

This chapter deals with simulations of optical properties, in the way introduced in section 1.4 to interpret the results of transient absorption spectroscopy experiments performed by our collaborators in Ghent and Delft[1]. We start with a description of the basic principles of this technique.

[1]Collaboration between groups part of IMEC, the Department of Chemical Engineering, the Center for Nano-and-Biophotonics, and the Inorganic and Physical Chemistry Department from Ghent University, and the Department of Chemical Engineering and The Kavli Institute of Nanoscience, from Delft University of Technology [67]

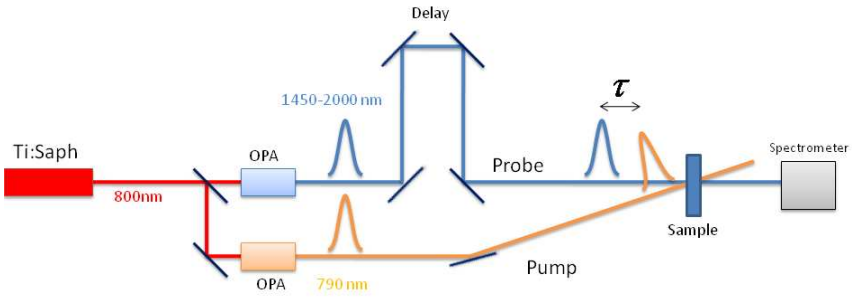

Figure 4.1: Transient absorption experiments scheme. In the specific experiments discussed in section 4.2.2, pump and probe pulses are obtained by non-linear processes at optical parametric amplification devices (OPA) using as primary source a Ti:Saph laser system. The delay time τ between the pump and the probe pulses can be controlled (here represented as change in the optical path). Both pulses are overlapped under a small angle over the quantum dot sample. The measured transient absorption corresponds to $\Delta\alpha = \alpha_0 - \alpha$, where α and α_0 are the measured absorptions with pump on and pump off, respectively. The positive values of this difference indicate bleach. An increase in absorption yields negative values.[67]

4.1.1 Transient Absorption Spectroscopy

In transient absorption spectroscopy, the transmission of a sample is measured as a function of time after its excitation to an electronically excited state by means of a laser pulse (pump), using a time-delayed probe pulse[68]. A general scheme and an extended description can be seen in Fig. 4.1. The ground state absorption in the excited sample is less than in the sample before the excitation, due to the promotion of a fraction of quantum dots (or molecules) to the excited state. Changing the time delay τ between the pump and the probe pulses, varying also the probe energy, and calculating the difference between the measured absorption in the excited sample α and the steady state absorption α_0 for each τ, a difference absorption spectrum profile (i.e. the $\Delta\alpha = \alpha_0 - \alpha$) is obtained as a function of τ and the wavelength λ. It contains information on the dynamic processes in the system under study. In the regime of the ultrafast processes in the nanostructures considered in this work, both pump and probe sources come from pulsed lasers with duration equal or below 50 fs[69, 70]. In the following, we will refer to the femtosecond transient absorption spectroscopy simply as TA.

In quantum dots, TA involves two types of transitions, interband and intraband ones. Interband transitions correspond to the optical excitation of electrons from occupied valence band states to unoccupied conduction band states. Each electron promoted to a band state leaves a hole in the initial valence state, leading to the creation of an electron-hole pair or exciton (the associated quasi-particle).

The nanocrystals presented in the previous chapters are in the strong confinement regime i.e. when the quantum dot size is smaller than the exciton Bohr radius. Both carriers are independently confined and the confinement energy is much larger than the Coulomb interaction, still present since the carriers are in a finite volume[18]. The band gap, as well as the spacing between states in the conduction band and the valence band of these confined structures, as already presented in chapters 2 and 3, strongly vary with size. This size-dependent behavior is clearly visible in the interband transitions[71].

After creation of an electron-hole pair by interband transition, intraband transitions may occur. The contributions are divided in two cases, when electrons located in the conduction band are excited to higher states in the conduction band, or when the holes are excited between

states in the valence band. Of course, intraband transitions are also size tunable.

In TA experiments, the effect of the pump pulse is the creation of single or multiple excitons, and interband or intraband transitions can be probed depending on the wavelength range of the probe beam[72]. TA signal contributions from electrons and holes are not easily resolved with a visible probe, and the intraband response is better characterized in the infrared (IR) range, for which the intraband transitions usually occur in nanocrystals [69]. Re-excitation to higher energy states using a second pump pulse can be used to obtain modulation of intraband populations[70].

Section 1.3.1 briefly introduced the way to label the electron and hole energy levels in analogy with the usual atomic notation, using a letter to denote the angular momentum of the envelope wave function (the index l in such a way that S corresponds to $l = 0$, P to $l = 1$, etc.) and the integer $n = 1, 2, 3, \ldots$, increasing with the energy, but without the restriction $l < n$. For the electron and hole states, the simplified notation $1S_e, 1P_e, D_e, \ldots; 1S_h, 1P_h, 1D_h, \ldots$, respectively, will be used. In bulk semiconductors, optical transitions only take place between states with the same wave vectors $\mathbf{k}$, and the intraband transitions need to be assisted by phonons or scattering on defects[18, 73]. In quantum dots, no-phonon intraband transitions are allowed, but it is shown that the difference between the quantum number l in the initial and final states, must be[18, 74]:

$$\Delta l = \pm 1 \Rightarrow \text{Transitions are allowed.} \tag{4.1}$$

The oscillator strengths associated to transitions such that $\Delta l \neq \pm 1$ are usually very small compared to the values in the allowed transitions[74]. Examples of intraband transitions analogue to the S $\rightarrow$ P transitions in atoms are discussed in detail in the following sections.

4.1.2 Implementation of the Calculations

The absorption spectrum of suspensions of colloidal quantum dots can be modeled in the same way as the system described in section 1.4.1. The refractive index n_{op} in Eq. 1.31 corresponds to the solvent, and the local field factor F is given by the dielectric constants of the solvent and of the bulk material of the quantum dots, using Eq. 1.21.

The calculated energy levels from a full or partial diagonalization of the TB Hamiltonian matrix are used in Eqs.1.31, 1.32 and 1.36 to build the optical matrix. The first quantity to be deduced is the optical coupling between two levels $|i\rangle$ and $|j\rangle$, represented by the oscillator strength, averaged over all the orientations of the electric field described by its polarization vector $\mathbf{e}$, and in consequence, all the other quantities are averaged in the same way. In the ground state, neglecting excitonic effects, the population term f_i is equal to 1 for all the valence states and equal to 0 for all the conduction states. Under these conditions, all absorption terms are null between two states of the conduction band or between two states of the valence band due to the term $[f_i - f_j]$, so there are no intraband terms in the ground state. In the implementation of these formulas for the calculations, the construction of the oscillator strength matrix terms from Eq. 1.32 is done in such a way that the rows will be labeled by the valence band states indices and the columns by the conduction band states indices. The notation is such that the first state, labeled as 1, in the conduction (valence) band is the LUS (HOS)[2], also corresponding to the lowest S-state in each case.

The effect on the quantum dot of the pump pulse is the excitation of an electron from a valence state to a conduction state, i.e., the creation of an electron-hole pair, and this can be represented in a simple way by switching the population of the HOS and the LUS. In the optical

[2]Highest occupied state (HOS) and lowest unoccupied state (LUS).

matrix notation, this is equivalent to exchange the row and the column representing the coupling with the HOS and the LUS, respectively. Then, the terms representing intraband transitions from (to) other energy states at the valence band (conduction band) to (from) the HOS (LUS), that were null in the ground state, are visible. It is straightforward to assume that multiple excitons can be modeled in the same way, exchanging a greater number of levels both at the conduction band and the valence band. The effects of these multiple substitutions are discussed in the section 4.2, for PbSe quantum dots.

The calculations of the absorption spectrum and the optical cross section are done starting from the oscillator strength. Both quantities are sums of peaks corresponding to single-particle transitions (Eqs. 1.31 and 1.36). We consider for each peak a Gaussian lineshape as in Eq. 1.35.

The intraband terms that are now allowed due to the change in the occupation number of both HOS and LUS appear as transitions both at the valence band and the conduction band. We can identify to which band belongs each transition, as it is possible to deduce which energy levels are involved from their positions in the optical matrix. The 1S-1P intraband transitions are usually well identified in photo-induced absorption spectroscopy experiments. The corresponding peaks are well defined in terms of transition energies, they are well separated from the others. At higher energy, intraband and interband transitions may be mixed such that their identification is more difficult.

In the next sections of this chapter, we study the intraband photo-induced absorption from the electronic structure of the quantum dots already considered in the previous chapters.

4.2 PbSe Quantum Dots

Published works on absorption spectroscopy and its theoretical analysis for this type of lead chalcogenide quantum dots are usually focused on the interband transitions[12, 14, 75–80]. The results of these works will not be reproduced here. We just remind that the lowest absorption peak (optical gap) corresponds to the interband $1S_h \rightarrow 1S_e$ transition. Its energy versus size is very well given by tight-binding calculations as shown in section 2.3. Higher energy peaks have been subject of intense debates that we do not discuss here.

4.2.1 S-P Intraband Transitions

IR induced intraband absorption in PbSe quantum dots was first reported in the work of Wehrenberg et al.[81], showing a strong increase in the absorption for sub-gap energy values in different samples of spherical nanocrystals The spectra of intraband transitions (shown in Fig. 4.2) are built taking a series of delay scans (10 and 300 ps) at different IR probe energies after a 1064 nm pump pulse. The intensity of the intraband peak at 10 ps is comparable to the intensity of the first exciton absorption peak and exhibits a symmetric shape, but the effect of the system relaxation is the reduction of the intensity and a shift of the intraband peak to lower energies. The origin of the long-lived broadband intraband absorption peak is suggested as a combination of transitions from a single electron and a single hole occupying the $1S_e$ and $1S_h$ states, respectively. The two different $1S_e - 1P_e$ and $1S_h - 1P_h$ transitions are not resolved separately in experiments since the masses of the electron and the hole are very similar (and therefore the confinement energies are similar). About the fast component, it is attributed to transitions of electrons and holes from the $1P_e$ and $1P_h$ states to higher energy states, explaining the broadband profile and fast decay.

It was already shown in Ref. [13] that the same tight-binding method as in the present work is able to describe these experimental results of Wehrenberg et al. [81]. An example showing

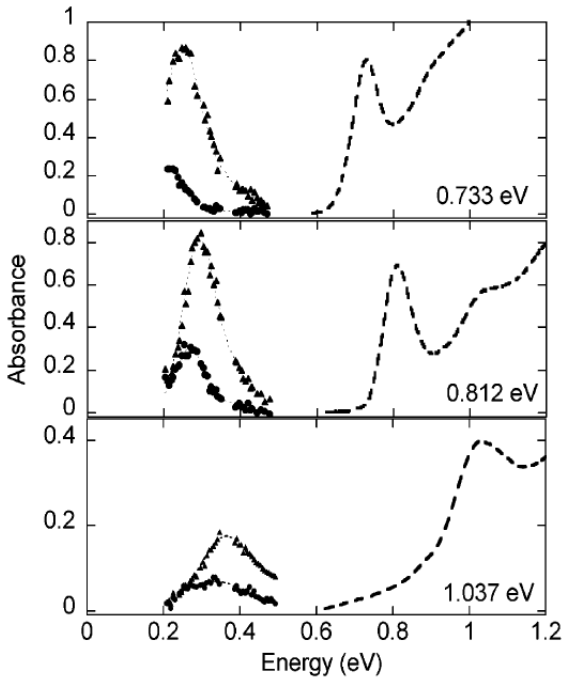

Figure 4.2: Transient absorption spectra from experiments on PbSe quantum dots [81]. The linear aborption spectra (−−) indicate the first exciton energy of each dot. It is easy to recognize the shift to a lower energy and the reduction of the intensity of the intraband peaks between 10 ps (▲) and 300 ps (•) time delays.

the good agreement between theory and experiments of Ref. [81] will be presented in section 4.2.3. Before, we discuss other TA experiments on PbSe nanocrystals.

4.2.2 Higher-Energy Intraband Transitions

Here we discuss the recent TA experiments performed by our collaborators. They have revealed intraband transitions at higher energy than S-P ones. The theoretical description of these transitions was one of the main objectives of our work.

The sample consists in PbSe quantum dots of diameter $d = 4.6$ nm dispersed in C_2Cl_4. The hot carriers in the excited states produced by a 50 fs pump pulse ($\lambda_{pump} = 790$ nm) cool down rapidly to the 1S state, and there is a reduction (absorption bleach) of the bandgap absorption, represented by a positive value of the difference $\Delta\alpha = \alpha_0 - \alpha$ between the ground state absorption α_0 and the absorbance after the pump α . Below the bandgap, in the interval between 1700 to 2000 nm or approximately 0.6 to 0.8 eV, well separated from the domain of the 1S-1P intraband peak, a negative value of $\Delta\alpha$ (i.e. an increase in the absorbance after the pump pulse) is measured, identified as photo-induced absorption[67] due to intraband transitions. Other possibilities as Coulomb shifts or absorption from surface-localized states or defects are discarded, due to the wavelength range and the broadband nature of the signal observed in the experiments. The photo-induced absorption is represented in Fig. 4.3, where the steady state and differential absorption spectrum 5 ps after the excitation are shown.

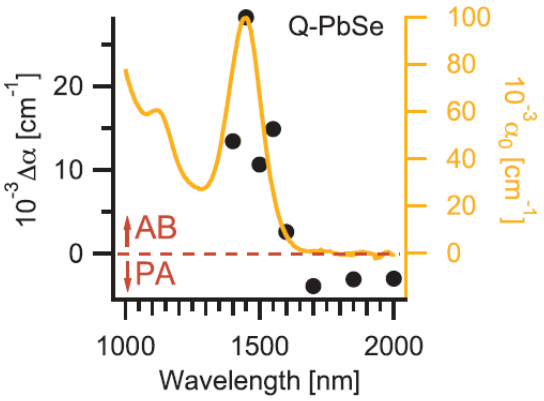

Figure 4.3: Steady state (α_0, in orange) and differential transient absorption spectrum ($\Delta\alpha$,black dots) of PbSe quantum dots, as originally displayed in [67]. The term $\Delta\alpha = \alpha_0 - \alpha$, where α is the absorption after a 5 ps delayed pump pulse, indicates bleach when positive. It is negative below the bandgap (1700 to 2000 nm), indicating photo-induced absorption. The induced S-P intraband transitions take place over 3000 nm, they are not visible in this experiment.

4.2.3 Calculations

Three different sizes ($D \approx 2.0; 3.0; 4.5$ nm) of spherical PbSe quantum dots were chosen for the oscillator strength and absorption spectrum calculations, the latter size enabling a direct comparison with the experiments of our partners [67]. The matrix of the TB Hamiltonian can still be fully diagonalized for these diameters (≈ 1600 atoms for $D \approx 4.5$ nm). For larger sizes, Conjugate Gradient or Jacobi-Davidson diagonalization procedures should be applied. Using the experimental refractive index of the solvent (1.49 for C_2Cl_4) and the PbSe bulk dielectric constant ($\epsilon_\infty \approx 23$)[13] the local field factor in Eqs. 1.21 and 1.22 is $|F^2| = 0.059$. We assume that the electron and the hole have time to be fully thermalized in their respective bands. Note that the radiative lifetime in PbSe nanocrystals is long, in the microsecond (μs) range.

In the quantum dot ground state, before creation of the electron-hole pair, all transitions correspond to the interband regime, as explained before in section 4.1.2. The corresponding oscillator strengths are shown in Fig. 4.4a for $D \approx 4.5nm$ (bandgap ≈ 0.86 eV), and Fig. 4.4b shows the oscillator strengths after creation of the electron-hole pair. The main intraband transitions around 0.2 eV correspond to 1S-1P with an oscillator strength of the same order of magnitude as the transition at the band gap[81]. Mixed contributions from the electron and the hole are identified. The absorption spectra are calculated using the oscillator strengths and a Gaussian lineshape (35 meV). The quantities α_0, α and $\Delta\alpha$ are shown in Figs.4.4c and 4.4d, where the normalization is done with respect to the maximum in the displayed range. We see that the bleach of the transitions at the bandgap is also obtained in our calculations. In Fig. 4.4e, we show the intense S-P peak between 0.1 and 0.4 eV, in good agreement with the experimental results of Wehrenberg et al. for quantum dots with similar energy gap, taking into account that the experimental spectra are cut below 0.2 eV, limited by the detector. The agreement is better with the spectra obtained after 300 ps, when the electron and the hole have relaxed to the 1S states.

Figure 4.5a shows the optical cross section of a quantum dot after creation of an electron-hole pair measured from TA (deduced from the absorption coefficient and the concentration of quantum dots in the solution) compared with our calculations. The amplitude of the cross section at the lowest $S_h - S_e$ interband transition (~ 0.86 eV) is in excellent agreement with

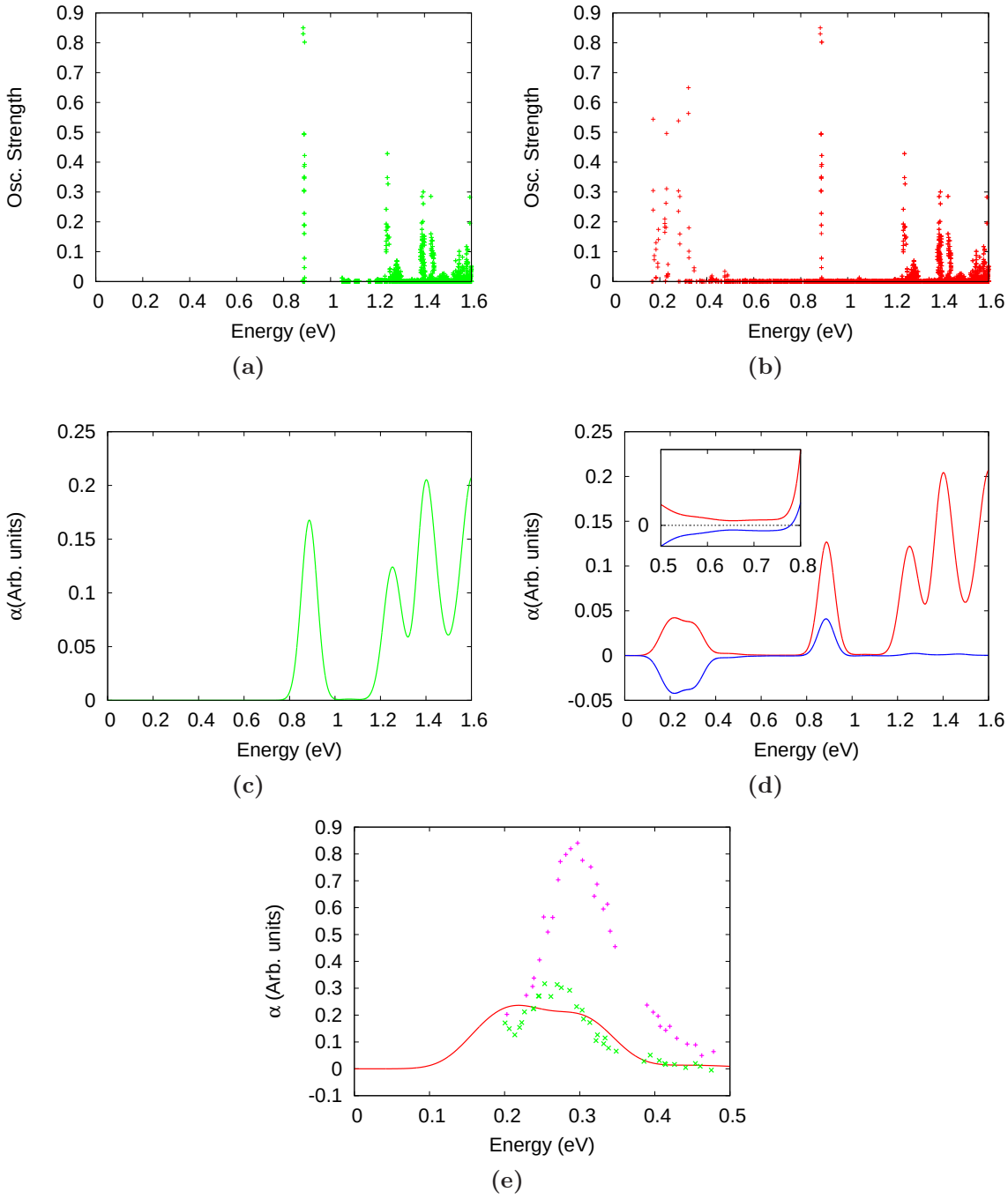

Figure 4.4: Oscillator Strength before **(a)** and after **(b)** pump. The 1S-1P peak for intraband transitions shows an oscillator strength comparable to the first exciton peak. In these plots the oscillator strength and the absorption spectra are normalized over the maximum in the whole displayed range. In **(c)**, the spectrum calculated before pump and **(d)** after the pump. The term $\Delta\alpha = \alpha_0 - \alpha$ (blue) is included in **(d)**. Negative values of $\Delta\alpha$ can be seen between the main intraband absorption peak and the bleached bandgap peak (zoom in the inset). In **(e)**, the intraband S-P transitions for a Pbse quantum dot $D \approx 4.5nm$ (bandgap ~ 0.86 eV) are compared with the result from Wehrenberg et al.[81] (Fig. 4.2) for a dot with bandgap 0.812 eV. The purple points indicate the 10 ps response, and the green ones correspond to the signal at 300 ps delay. Our calculations, in red, are normalized to the scale of Fig. 4.2.

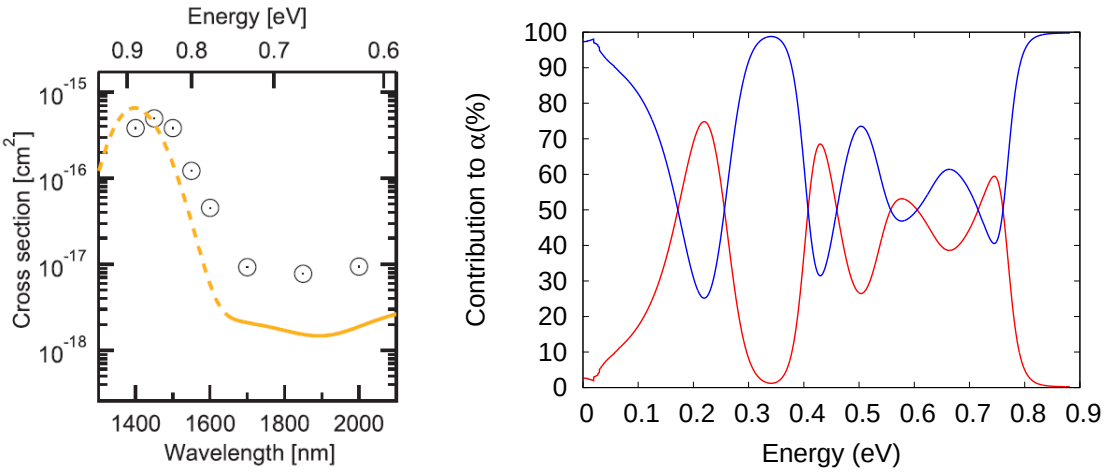

Figure 4.5: **(a)** Calculated cross section (line) for a PbSe nanocrystal of $D \approx 4.5$ nm, compared with the experimental cross-section measured after 500 ps (dots)[67]. **(b)** Contributions to the absorption from the electron (red) and the hole (blue).

the experiments. The theory also explains the existence of the broadband induced absorption between 0.6 eV and 0.75 eV, even if the theoretical cross section is too small. It is important to note first that the the amplitude of this PA broad signal does not depend on the lineshape broadening value, since it remains the same for lower values, e.g. $\sigma = 5$ meV. Calculations of the dielectric constant on lead chalcogenide quantum dots show no significant size dependence, as the average values are very similar to the bulk value for different crystal sizes[25]. Therefore the discrepancy between theory and experiments in Fig. 4.3 cannot be explained by a size-dependence of the local field factor $|F^2|$ due to a change in the dielectric constant. No excitonic effects are taken into account as it has been mentioned previously, and this could be an explanation for the difference in the amplitude of the signal. A complementary explanation might be the effect of electron-phonon coupling if phonon-assisted transitions are involved in the photo-induced absorption[82].

The contributions from electron or hole transitions in the range of interest (from ≈ 0.6 eV to 0.8 eV for $D \approx 4.5$ nm) are almost equal, as can be seen in Fig. 4.5b. If the electron-hole pair is not in the 1S states, but in the higher energy P-states, there is an increase in the photo-induced absorption signal in the mentioned range (Fig. 4.6). We conclude that intraband transitions are more efficient at higher initial states, and this might explain that in the experiments, as carriers occupy P states during their cooling towards the 1S states, the photo-induced absorption transient signal exceeds the absorption bleach transient signal at the band gap[67]. The simulation of multiple excitons by switching the occupation of multiple states at the same time, as displayed in Fig. 4.6 for the case of 2, 4 or even 8 electrons and holes in the S states also shows an increase in the intraband PA signal, but in this case it is accompanied by a reduction (bleach) in the main transition at the bandgap.

The identification of the high energy states involved in the PA in the range shown in Fig. 4.5a is not straightforward. We consider a larger number of states than in the 1S-1P case, as we take about 300 electron (hole) states in the conduction (valence) band for the calculation of the PA signal in this range. There are many transitions with non-negligible oscillator strength to states which should correspond to 1D-1F states, but at the same time there are also 2S and

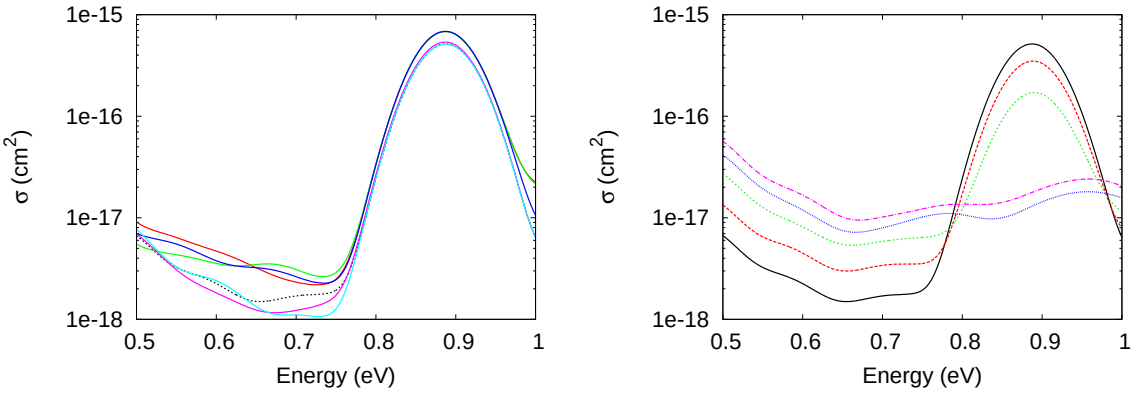

Figure 4.6: **(a)** Optical cross section for a single electron-hole pair in different situations: in the band edges (black dashed line), for an intermediate S state (purple), and the higher S state (light blue). In the lower P state (red) the signal of the photo-induced absorption is increased, going to a maximum for an intermediate P state (green) and starts to reduce for higher energy P states (blue). **(b)** Cross section calculated assuming a larger number of electron-hole pairs in the S states 2 (red), 4 (green), 6 (blue) and 8 (purple), compared to the single exciton in the 1S state.

2P states close in energy (1S-2P transitions should also fulfill $\Delta l = \pm 1$). The final states for all these transitions are forming a dense spectrum as shown by the density of states plotted in Fig. 4.7, and the involved states could be a mixing between 1F and 2P states. Complex mixing of the states is due to the fact that the true Hamiltonian is not spherical, not fulfilling the necessary symmetry condition (for the envelope wave functions), which relates the optical transitions and the selection rule $\Delta l = \pm 1$ introduced in 4.1[74].

The plots of the calculated cross section for the other nanocrystal sizes are included in Fig. 4.8. The 1S-1P transition peaks broaden as the size decreases [13, 81].

The high interband absorption cross-sections of PbSe quantum dots make easy to obtain the intraband absorption studied here. The wide spectral range of this response, as well as the possibility to be tuned with size in the same way as the bandgap, converts them (and by extension, other lead chalcogenides) in an interesting alternative for all-optical signal processing devices, given the stronger effect of the free carrier absorption, compared with, for example, silicon.

Next, we apply our calculations to photo-induced intraband transitions in II-VI quantum dots, to evaluate differences in the optical spectrum, compared to the PbSe quantum dots. The works about the absorption properties of II-VI materials can be found in a more important proportion than the works on IV-VI materials[69, 83–108], in particular for CdSe quantum dots.

4.3 CdSe Quantum Dots

Induced intraband transitions in CdSe nanocrystals were reported by Guyot-Sionnest et al.[89], considerably earlier than in PbSe quantum dots, using the same type of TA techniques as in the previous section, with probe infrared laser pulses. The intense intraband peaks (up to one order of magnitude over the intensity of the first exciton absorption peak) are associated exclusively

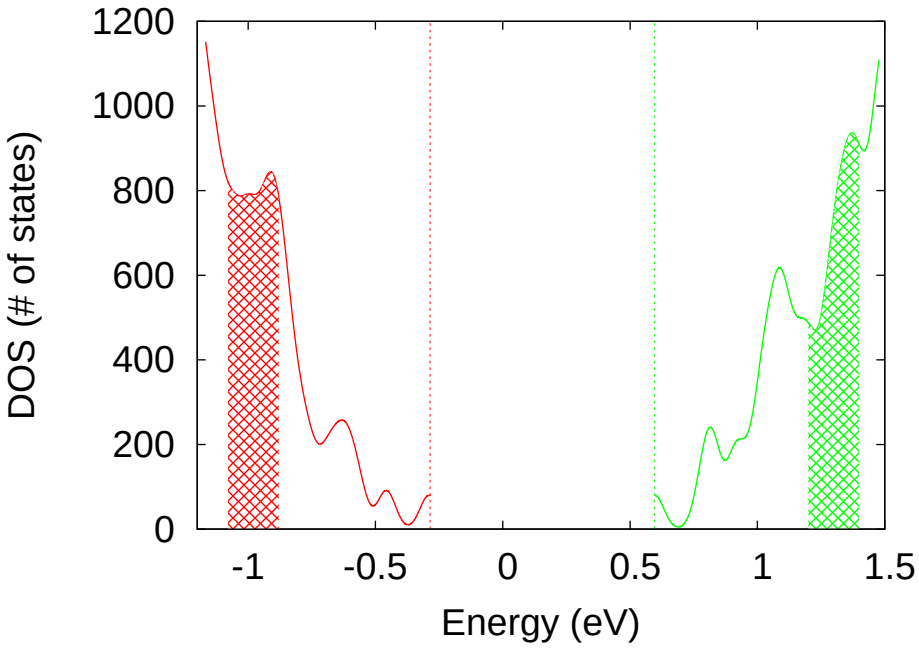

Figure 4.7: Density of states for the electron and hole in a 4.5 nm PbSe quantum dot. The dashed lines are the valence and conduction band edges. A large number of states both from conduction band and valence band contributes to the intraband absorption between 0.6 eV and 0.8 eV (shaded regions), forming a quasi-continuum in the corresponding regions of energy measured from the edge of each band.

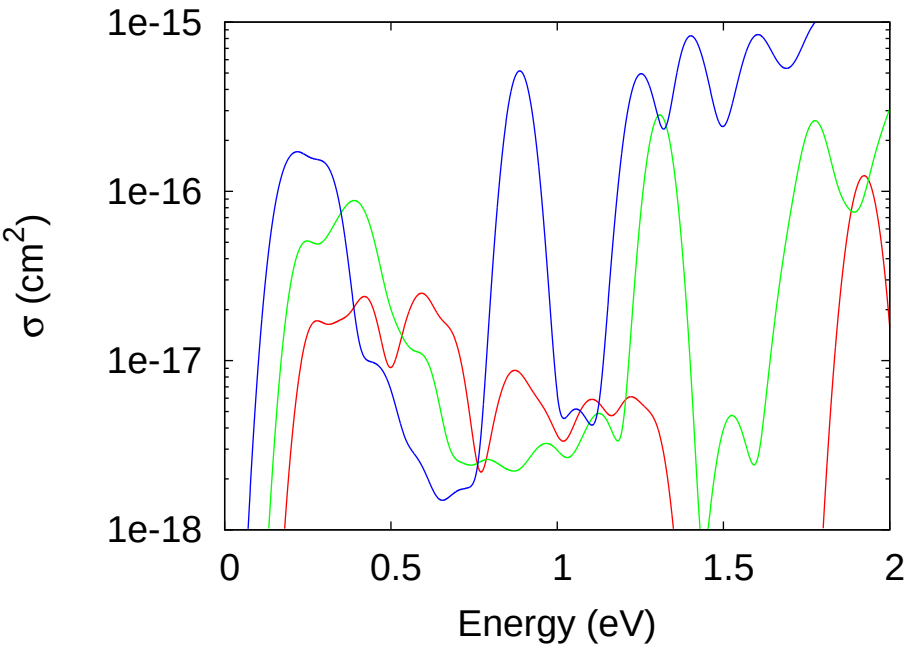

Figure 4.8: Cross section spectra for PbSe quantum dots of 2.0 nm (red), 3.0 nm (green) and 4.5 nm (blue) diameters. The electron and hole contributions are splitted for the smaller dots.

with the one-electron $1S_e - 1P_e$ transition. To explain why the hole makes no contribution to the intraband transitions, the same report cites previous studies on CdSe, giving two different assumptions about the hole after excitation, as being in a delocalized state[85, 86], or being localized after ultra-rapid surface trapping[109]. The latter is accepted to be the best explanation of the absence of the hole transitions in the main intraband peak. In Refs.[94, 95], the group of Guyot-Sionnest measured the infrared absorption induced by the injection of extra electrons in the nanocrystals using electrochemical approach. In that case, the infrared absorption can only be due to the excitation of the electron(s).

Transient absorption from the hole in the infrared or the near-infrared ranges was reported in CdSe nanocrystals in Refs.[69, 91, 96]. In Refs. [69, 96], the TA signal was only measured at selected wavelengths so that the nature of the transitions cannot be deduced. In Ref. [91], the TA signal was measured in the [0.5-0.7] and [0.8-1.05] eV ranges as shown in Fig. 4.9. This signal decays very rapidly (faster than 5 ps), which is attributed to the fast trapping of the hole, likely at the surface of the nanocrystals.

For our calculations, five different nanocrystals were chosen, again into the limit to apply full diagonalization procedures. The diameters are $D \approx 3.0$; 3.5; 4.5; 6.0 nm, and a larger dot of $D \approx 7.0$ nm, for which a conjugate gradient procedure was necessary to achieve the sufficient number of states to cover the energy range of the studied transitions.

We use the CdSe bulk dielectric constant ($\epsilon_0 \approx 7$)[16][3], then the local field factor in this case is $|F|^2 = 0.339$, one order of magnitude larger then the value for PbSe, using the same solvent (C_2Cl_4) as in the calculations in the previous section. The Gaussian lineshape used to calculate the absorption spectra is also the same (35 meV).

The calculated TA spectra are shown in Fig. 4.10a. The stronger intraband peak, below 0.5 eV, corresponds to the expected $1S_e - 1P_e$ transitions. As the diameter of the dots is increased,

[3]The values usually presented in the literature can change between $\epsilon = 6$ and $\epsilon = 8$.

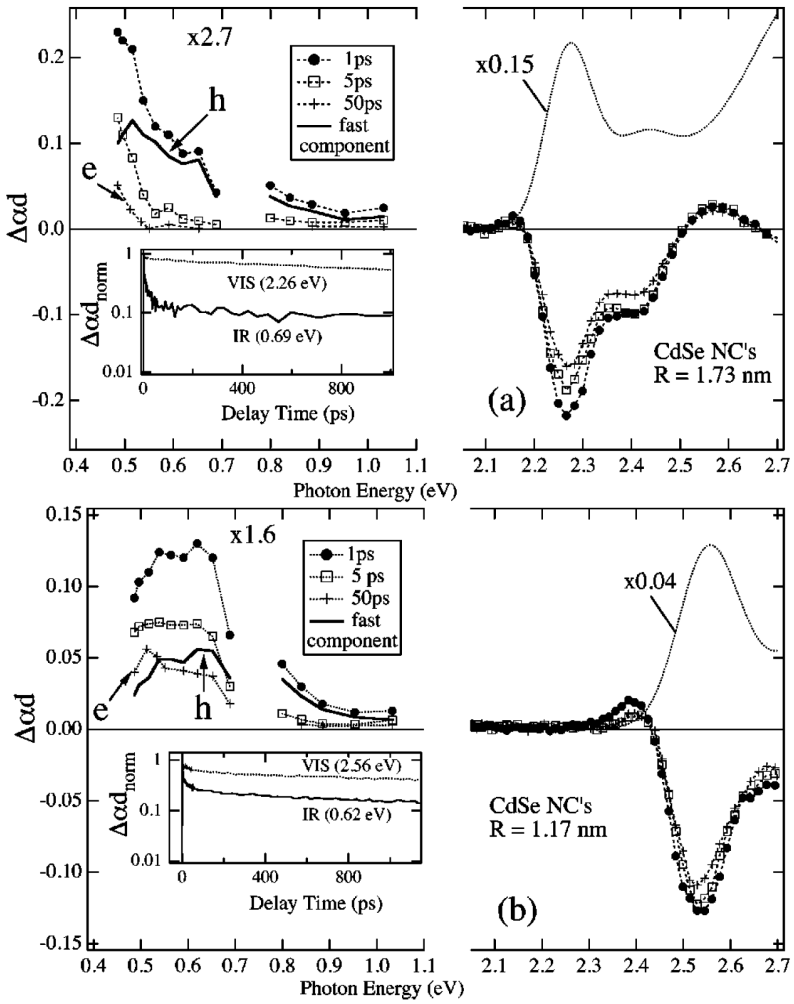

Figure 4.9: TA spectra of CdSe nanocrystals for R = 1.73 nm **(a)** and 1.17 nm **(b)** [91] for various values of the time delay between pump and probe pulses are indicated in the left side. The rapid decay of the signal is due to fast trapping of the hole. The TA spectra at 50 ps are attributed to the electron only. Therefore the hole contribution (fast component) is deduced as the difference between the TA spectra obtained at 50 ps and 1 ps.

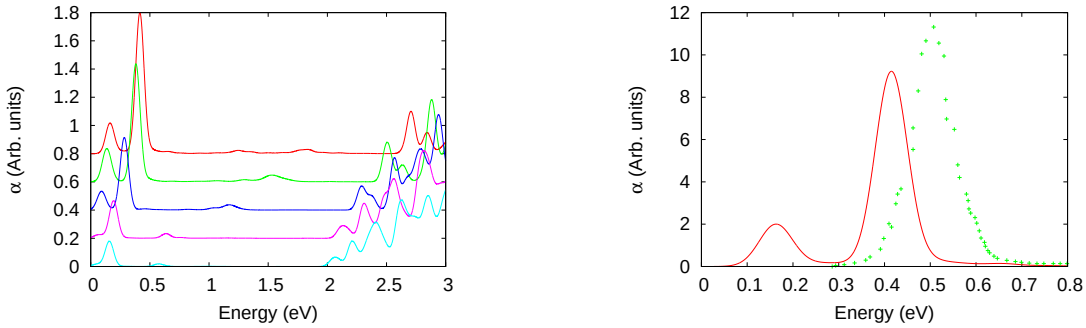

(a) **(b)**

Figure 4.10: **(a)** Calculated TA spectra of CdSe quantum dots for (from top to bottom) $D \sim 3.0$ nm, 3.5 nm, 4.5 nm, 6.0 nm, and 7.0 nm. **(b)** Comparison between the $1S_e - 1P_e$ transition peak as reported in Ref. [89] for $D \sim 3.15$ nm and the absorption calculated for $D \sim 3.0$ nm. The low energy peak corresponds to the hole transitions which are absent in the experimental spectrum.

this intraband peak shifts to lower energy values, following the corresponding splitting of the electronic levels at the conduction band already discussed in section 2.2.1. There is a second lower energy peak just below the $1S_e - 1P_e$, which is mainly produced by hole transitions with smaller amplitude and visible in the calculations just for the smaller dots, its position is, once more, in agreement with the results of the splitting at the valence band in Fig. 2.1.

The low-energy peak associated with the hole is out of range for the detectors in the TA experiments of Refs. [69, 91, 96]. In addition, intraband absorption of the hole is usually not visible due to its fast capture by defects, as discussed previously. Figure 4.10b shows a comparison between calculations and experiments[89] for D close to 3nm. The calculated $1S_e - 1P_e$ transition peak is ~ 0.1 eV too low in energy. This difference may be due to the important electric field induced by the hole trapped at the surface, as discussed in Ref. [89]

In the region between the $1S_e - 1P_e$ intraband peak and the $1S_h - 1S_e$ interband peaks, our calculations predict other peaks which, to our knowledge, have not been discussed so far. This region is completely dominated by hole transitions, most of them with negligible oscillator strength values. But Fig. 4.10a shows, for each dot size, a well-defined broad peak in the middle of that region. As the crystal size is increased, the peak shifts to lower energy values, in a wide range, going from approximately 1.8 eV for the 3 nm dot, to approximately 0.6 eV for the 7 nm dot. It varies with size faster than the bandgap and the $1S_e - 1P_e$ splitting, as shown in Fig. 4.11a. The optical cross-section of this intraband peak is one order of magnitude smaller than for the first interband transition and increases with the dot size, as can be seen in Fig. 4.11b, where the cross-sections calculated for three sizes (3.0 nm, 4.5 nm and 7.0 nm) are displayed. The peak has a low intensity component (the tail at lower energy in the plots of Fig. 4.10a), mixing contributions from the electron and the hole in the same proportion. But the higher intensity part is completely dominated by contributions from the hole. It involves transitions to the band edge from states with density even higher (Fig. 4.11c) than PbSe quantum dots, then it is even more difficult to identify the type of transitions.

The very fast (< 5 ps) TA signal in the [0.5-0.7] and [0.8-1.05] eV ranges obtained in Ref. [91] and shown in Fig. 4.9 could be effectively attributed to the absorption from the hole. It is however impossible to conclude at the present stage without experimental data to check the agreement. We can only say that the calculations predict this new group of transitions,

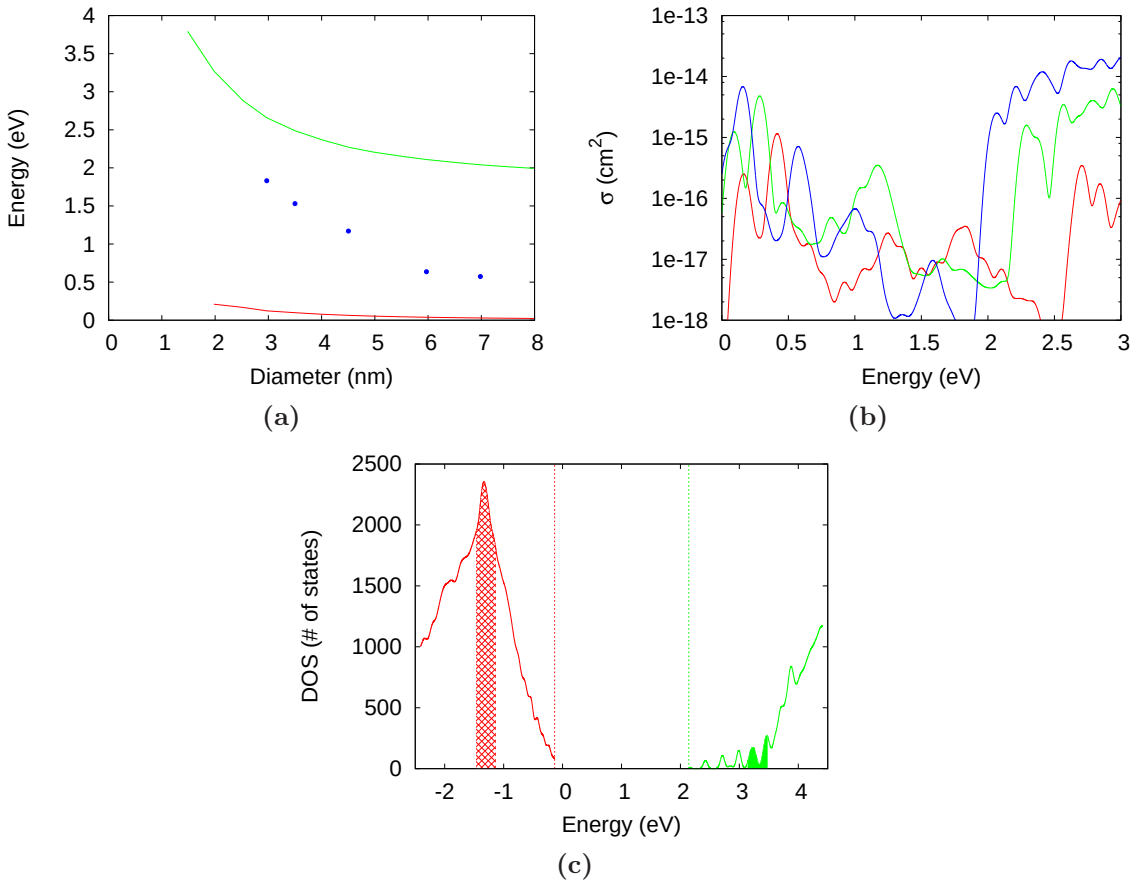

Figure 4.11: **(a)** Position of the maximum of the new intraband absorption peak predicted by the calculations (blue points) plotted versus the dot diameter, compared to the bandgap (green) and the S-P splitting at the valence band (red). **(b)** TA cross section calculated for three sizes, 3.0 nm (red), 4.5 nm (green), and 7.0 nm (blue), with the peaks of interest at ~ 1.83 eV, ~ 1.17 eV, and ~ 0.57 eV, respectively. All peaks below ~ 0.5 eV correspond to $1S_e - 1P_e$ transitions. **(c)** Density of states for the 4.5 nm quantum dot, with a strong maximum for the valence band states (red) corresponding to the maximum of the hole intraband absorption.

which are in energy ranges not considered in the usual experimental setups to detect the well characterized IR intraband absorption. In order to observe these new transitions, the trapping of the hole by surface states must be avoided. This can be achieved using core/shell nanocrystals, like CdSe/ZnS[110].

The structure of the valence band in WZ CdSe is very complicated as shown in Fig. 1.2. There are several bands very close in energy which, in the nanocrystals, give rise to confined states. Therefore the identification of the states involved in the transitions is not clear at the moment. We should perform more complex analysis of the final hole states, for example using projections on the bulk valence-band states, to be able to identify them.

Once more, the prediction of new TA bands in the near-to-mid infrared (in a wider range than for PbSe) is very interesting for all-optical signal processing.

4.4 PbSe/CdSe Quantum Dots

We discussed in Chapter 3 the dominant effect of the core in the electronic structure of core/shell quantum dots. The shell acts as a barrier, and there is complete delocalization of the states over the entire dot for energies above the offsets.

An experimental study on the intraband spectroscopy of II-VI CdSe/CdS core/shell quantum dots[72] shows redshift of the intraband and interband spectra as the shell thickness is increased. The hole stays localized in the core, and the spectra (for the different thickness) can be associated with the valence band behavior of the core. In these examples, the difference between the bulk bandgaps is less significant, then it is possible to have either type I or type II alignments.

Studies on the interband absorption of PbSe/CdSe[49, 111] show that the first absorption peak is defined by the PbSe core, as discussed in Chapter 3.

The experiments of our collaborators were performed in the same conditions described in section 4.2.2 on samples of PbSe/CdSe core/shell quantum dots, synthesized by means of cation exchange[38]. The PbSe core diameter in this case is 4.5 nm and the ZB CdSe thickness is 0.5 nm. Figure 4.12 shows the differential absorption spectrum measured in Ref. [67], with a 5 ps delay pump pulse. The core being equivalent, the bandgap is approximately the same as in PbSe nanocrystals discussed in section 3.3. This spectrum shows exactly the same absorption bleach at the gap as in the case of PbSe quantum dots (Fig. 4.3). The photo-induced absorption, represented by a negative value of $\Delta\alpha$, was reported for the PbSe dots in the same energy range. The measured cross-section, though not displayed here, gives values closer to the results in PbSe after 500 ps, between 7.0×10^{-18} and $8.0 \times 10^{-18}\text{cm}^2$(see Fig. 4.5a).

Calculations

The calculations of section 3.3 showed that, in our approximation, as the shell thickness is changed, neither the value of the bandgap is affected, nor the band splitting. The two different valence band offsets used in that section also gave similar relation between bandgap and core size. Therefore, we restrict our calculations to shell thickness at the lowest value (0.5 nm).

The expression for the local-field factor in Eq. 1.21 takes into account a spherical nanocrystal formed by a single semiconductor compound. To define the dielectric permittivity of core/shell structures, we can use the general expression [49, 112]:

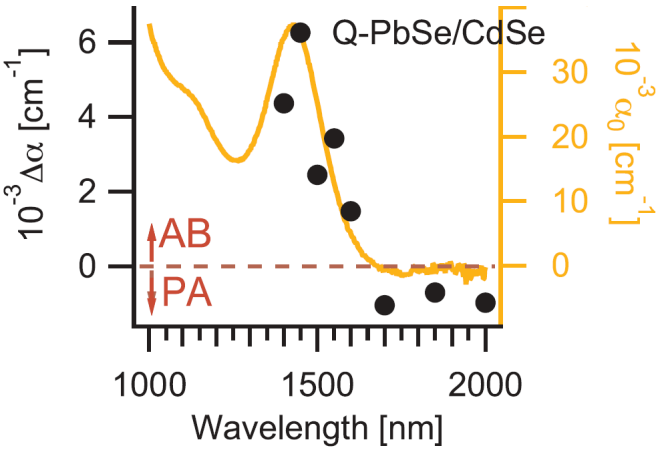

Figure 4.12: Steady state (α_0, in orange) and differential transient absorption spectrum ($\Delta\alpha$,black dots) of PbSe/CdSe quantum dots, as originally displayed in Ref. [67]. The term $\Delta\alpha = \alpha_0 - \alpha$, where α is the absorption after a 5 ps delayed pump pulse, indicates bleach when positive, and photo-induced absorption when negative, here below the bandgap (1700 to 2000 nm).

$$|F| = \left| \frac{9\epsilon_{sh}\epsilon_{out}}{\epsilon_{sh}\epsilon_a + 2\epsilon_{out}\epsilon_b} \right|, \tag{4.2}$$

with

$$\epsilon_a = \epsilon_c \left(3 - 2\frac{V_{sh}}{V_{QD}}\right) + 2\epsilon_{sh}\frac{V_{sh}}{V_{QD}},$$
$$\epsilon_b = \epsilon_c \frac{V_{sh}}{V_{QD}} + \epsilon_{sh}\left(3 - \frac{V_{sh}}{V_{QD}}\right);$$

where ϵ_c and ϵ_{sh} are the dielectric constants of the core and the shell, respectively, and we use the ratio between the volume of the shell and the total volume of the nanocrystal V_{sh}/V_{QD}. In the construction of the system, described in section 3.3, the shell thickness is such that the ratio is ~ 0.75. Using the values of the bulk dielectric constants for PbSe and CdSe in Eq. 4.2, the mean value of the local-field factor for the dots selected in this section $|F_{CS}|^2 \sim 0.09$ is closer to the core ($|F_{PbSe}|^2 = 0.059$) than to the shell ($|F_{CdSe}|^2 = 0.3$) value. The core and shell diameters were chosen to match the sizes in the experiments mentioned at the beginning of this section, and we add two sets of values to compare with the dots presented in the previous sections. The dot sizes, and the corresponding volume ratio and local-field factor are summarized in Table 4.1.

Eff. Diam. Core	Eff. Diam. Shell	V_{sh}/V_{QD}	$\lvert F\rvert^2$
3.57 nm	5.45 nm	0.78108	0.09376
4.40 nm	6.25 nm	0.74108	0.09130
6.90 nm	9.38 nm	0.71566	0.08978

Table 4.1: PbSe/CdSe local-field factor calculated from Eq. 4.2.

The calculated cross-sections for a PbSe/CdSe core/shell quantum dot and for the equivalent PbSe quantum dot with the diameters of the nanocrystals studied in Ref. [67], are presented

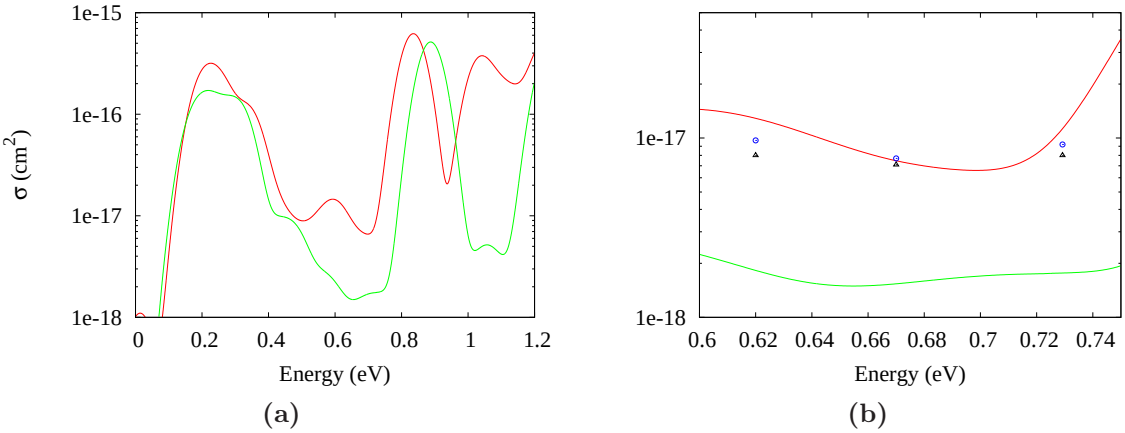

Figure 4.13: **(a)** Optical cross section for PbSe/CdSe (red) and PbSe (green) quantum dots with core diameter ≈ 4.5 nm, after excitation of a single electron-hole pair. **(b)** Zoom over the zone where the experimental induced absorption is identified for PbSe ($\triangle$) and PbSe/CdSe (blue $\circ$) quantum dots[67].

in Figs. 4.13. We selected the dot with the electronic structure displayed at the center of Fig. 3.4. The positions of the main intraband peak and of the first exciton peak, as expected from the electronic structure calculations, are very similar for the two types of quantum dots, with just a slight shift in the value of the bandgap (Fig. 4.13a). The new group of photo-induced intraband transitions shows a larger cross-section than in PbSe nanocrystals. Interestingly, the cross section for PbSe/CdSe nanocrystals is now in excellent agreement with experiments as shown in Fig. 4.13b whereas, for PbSe quantum dots, it is underestimated. The reason for this better agreement for core/shell nanocrystals is not easy to identify. From Fig. 4.13a, it is clear that the presence of the shell strongly enhances the photo-induced absorption between 0.5 and 0.8 eV. A possible explanation is that the shell induces breaking of the selection rules by mixing states from PbSe and CdSe. Evaluating the contributions from the electron and the hole to the group of intraband transitions, no relevant difference can be observed for the $1S-1P$ peak, compared to the case of the PbSe quantum dot, where electron and hole contribute in the same proportion. For the second intraband peak, the relative contribution from the hole is increased.

The absorption cross section for the three quantum dots of Table 4.1 is presented in Fig. 4.14. As the size decreases, the $1S-1P$ peaks broaden and the induced absoprtion above these peaks and below the bandgap is enhanced. Similar behavior was found for PbSe quantum dots.

The improvement in thermal and photochemical stability produced by the shell makes this type of hetero-nanostructures even more suitable for the applications already mentioned for the PbSe quantum dots, given their similarities.

Conclusions

With the purpose to understand the origin of non-previously reported photo-induced intraband transitions in TA experiments on PbSe and core/shell PbSe/CdSe quantum dot samples, we have applied the methods introduced in Chapter 1 to the calculation of optical properties of the quantum dots described in Chapters 2 and 3.

Known features like the absorption bleach at the bandgap, as well as the main S-P intraband

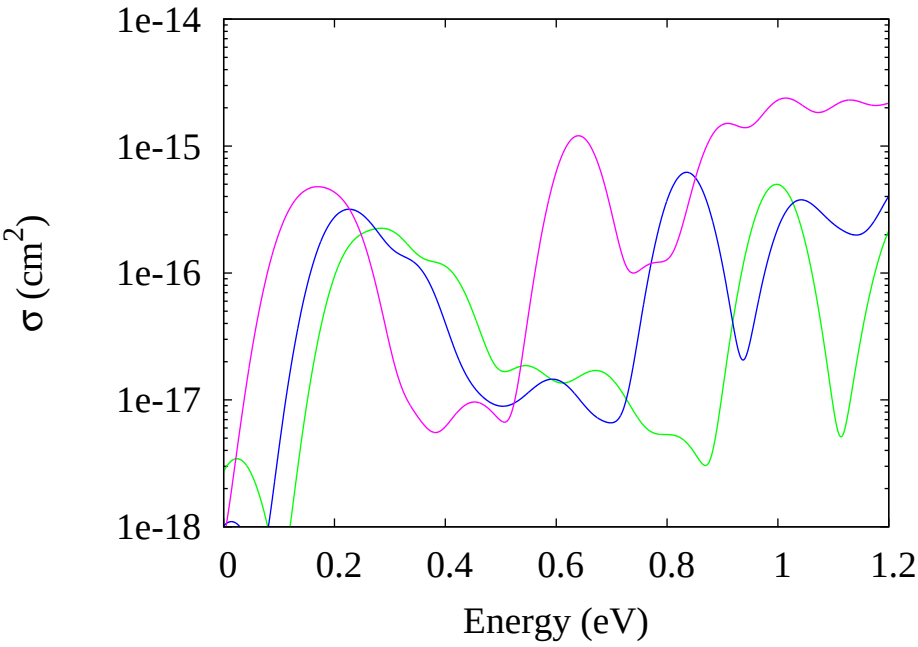

Figure 4.14: Optical cross section for PbSe/CdSe quantum dots with core diameter $\sim$ 3.5 (green) nm, 4.5 nm (blue) and 6.9 nm (purple), after excitation of a single electron-hole pair. The change in energy and broadening of the 1S-1P peaks is comparable to the case of PbSe quantum dots (Fig. 4.8).

peaks, are very well described by our theory. In addition, the analysis of the absorption spectra in the range of energy evaluated in the experiments lets us identify a new group of intraband transitions. The calculated optical cross section is consistent with the measurements, being underestimated in the case of PbSe quantum dots, but yields an excellent agreement in the PbSe/CdSe nanocrystals. As expected from the electronic structure calculations, the absorption spectrum of a PbSe/CdSe quantum dot is mainly influenced by the PbSe core, but the presence of the shell enhances the absorption in the intraband regime, especially for the group of new transitions. The calculations for CdSe quantum dots also reveal the existence of a group of intraband transitions which do not seem to be exhaustively studied in the literature.

We can affirm that in the limit of the approximations, not taking into account excitonic effects or phonon-assisted transitions, this method is able to give a qualitative description of induced intraband absorption in these systems.

Conclusion

The size-tunable electronic structure and optical properties of colloidal nanocrystals, along with the possibilities of manipulation that they offer to be integrated on surfaces, convert this type of nanostructures in an interesting alternative for the development of photonic nano-materials. The development of nanocrystals containing heterojunctions offers new opportunities for applications, but characterization of the band alignment at the interface is still needed for future progress in this field, which is clearly challenging.

We have used the TB method for the calculation of the electronic structure of nanocrystals, transferring the parameters defined for the bulk material to the case of the spherical nanocrystals studied in this work. We started with calculations on PbSe, CdSe and CdTe nanocrystals. We have obtained a reliable description of the relation between the gap and the size, showing good agreement with available experiments. We have also studied PbSe/CdSe core/shell quantum dots which have been recently synthesized. Due to the difference between the bulk bandgaps of PbSe and CdSe, it was assumed that the shell acts as a barrier in a type I band alignment. The band offset was deduced from the experimental value determined by colleagues of the Herodot network. Under these assumptions, our calculated electronic structures for PbSe/CdSe quantum dots show to be governed by the PbSe core. The effects induced by the fact that PbSe and CdSe have their bandgap at two different points of the Brillouin zone were studied with some care. We show in particular that, above the barriers, the electronic states are fully delocalized over the whole nanocrystals. In the future, it would be particularly interesting to perform calculations of the band offsets at PbSe/CdeSe heterojunctions to strengthen the hypothesis of the present work.

The calculation of the optical properties using the electronic structure is achieved defining the optical coupling between the states. Then the resulting group of oscillator strengths can be used for the calculation of the absorption and the optical cross section. The ground state interband absorption, and the intraband absorption (which appears after the creation of an electron-hole pair in transient absorption experiments), are reasonably well described by these calculations. Similar results are obtained for PbSe and PbSe/CdSe quantum dots, showing that the optical properties are mainly governed by the core. Our work has revealed the existence of new bands of photo-induced intraband absorption in ranges which could be of interest for applications in photonics. In the future, it would be particularly interesting to extend this study to other types of semiconductor quantum dots, III-VI or II-VI, in a more systematic manner.

Bibliography

[1] Maria Rosa Antognazza, Francesco Scotognella, Karol Miszta, Dirk Dorfs, Marco Zanella, Margherita Zavelani-Rossi, Liberato Manna, Guglielmo Lanzani, and Francesco Tassone. Steady-state photoinduced absorption of CdSe/CdS octapod shaped nanocrystals. *Physical Chemistry Chemical Physics : PCCP*, 13(33):15326–15330, July 2011.

[2] Hunter McDaniel, Philip Edward Heil, Cheng-Lin Tsai, Kyekyoon Kevin Kim, and Moonsub Shim. Integration of type II nanorod heterostructures into photovoltaics. *ACS Nano*, 5(9):7677–83, September 2011.

[3] Celso de Mello Donegá. Synthesis and properties of colloidal heteronanocrystals. *Chemical Society Reviews*, 40(3):1512–46, March 2011.

[4] Carina Faber, Jonathan Laflamme Janssen, Michel Côté, E. Runge, and X. Blase. Electron-phonon coupling in the C_{60} fullerene within the many-body GW approach. *Physical Review B*, 84(15):30–34, October 2011.

[5] J. C. Slater and G. F. Koster. Simplified LCAO method for the periodic potential problem. *Physical Review*, 94:1498, 1954.

[6] M.C. Payne, M.P. Teter, D.C. Allan, T.A. Arias, and J.D. Joannopoulos. Iterative minimization techniques for ab initio total-energy calculations: molecular dynamics and conjugate gradients. *Reviews of Modern Physics*, 64(4):1045–1097, 1992.

[7] Y. M. Niquet, C. Delerue, and G. Allan. Method for tight-binding parametrization: Application to silicon nanostructures. *Physical Review B*, 62(8):5109–5116, 2000.

[8] Richard Karel Capek, Iwan Moreels, Karel Lambert, David De Muynck, Qiang Zhao, André Van Tomme, Frank Vanhaecke, and Zeger Hens. Optical Properties of Zincblende Cadmium Selenide Quantum Dots. *The Journal of Physical Chemistry C*, 114(14):6371–6376, 2010.

[9] C. Delerue, G. Allan, and Y. Niquet. Collective excitations in charged nanocrystals and in close–packed arrays of charged nanocrystals. *Physical Review B*, 72(19):1–6, November 2005.

[10] Y.M. Niquet. *Etude des propiétés de transport de nanostructures de semiconducteurs*. PhD thesis, Université des Sciences et Technologies de Lille, 2001.

[11] V. Albe, C. Jouanin, and D. Bertho. Confinement and shape effects on the optical spectra of small CdSe nanocrystals. *Physical Review B*, 58(8):4713–4720, August 1998.

[12] Rolf Koole, Guy Allan, Christophe Delerue, Andries Meijerink, Daniël Vanmaekelbergh, and Arjan J. Houtepen. Optical investigation of quantum confinement in PbSe nanocrystals at different points in the Brillouin zone. *Small (Weinheim an der Bergstrasse, Germany)*, 4(1):127–33, January 2008.

[13] G. Allan and C. Delerue. Confinement effects in PbSe quantum wells and nanocrystals. *Physical Review B*, 70(24):1–9, December 2004.

[14] J. M. An, A. Franceschetti, S. V. Dudiy, and Alex Zunger. The peculiar electronic structure of PbSe quantum dots. *Nano Letters*, 6(12):2728–35, December 2006.

[15] Su-Huai Wei and Alex Zunger. Electronic and structural anomalies in lead chalcogenides. *Physical Review B*, 55(20):605–610, 1997.

[16] Y. Masumoto and T. Takagahara, editors. *Semiconductor Quantum Dots: Physics, Spectroscopy and Applications*. Springer, Berlin, 2002.

[17] M. Fox. *Optical Properties of Solids*. Oxford University Press, New York, 2001.

[18] C. Delerue and M. Lanoo. *Nanostructures: Theory and Modelling*. Springer, Berlin, 2004.

[19] PE Lippens and M. Lannoo. Calculation of the band gap for small CdS and ZnS crystallites. *Physical Review B*, 39(15):10935, 1989.

[20] P.E. Lippens and M. Lannoo. Comparison between calculated and experimental values of the lowest excited electronic state of small CdSe crystallites. *Physical Review B*, 41(9):6079–6081, 1990.

[21] L. W. Wang and A. Zunger. Pseudopotential calculations of nanoscale CdSe quantum dots. *Physical Review B*, 53(15):9579–9582, April 1996.

[22] G. L. G. Sleijpen and H. A. Van der Vorst. A jacobi–davidson iteration method for linear eigenvalue problems. *SIAM Review*, 42:267, 2000.

[23] Lin-Wang Wang and Alex Zunger. Solving Schroödingers equation around a desired energy: Application to silicon quantum dots. *The Journal of Chemical Physics*, 100(3):2394, 1994.

[24] C. B. Murray, D. J. Norris, and M. G. Bawendi. Synthesis and characterization of nearly monodisperse CdE (E= S, Se, Te) semiconductor nanocrystallites. *Journal of the American Chemical Society*, 115(4):8706–8715, 1993.

[25] Iwan Moreels, Guy Allan, Bram De Geyter, Ludger Wirtz, Christophe Delerue, and Zeger Hens. Dielectric function of colloidal lead chalcogenide quantum dots obtained by a Kramers-Krönig analysis of the absorbance spectrum. *Physical Review B*, 81(23):1–7, June 2010.

[26] W. W. Yu, Lianhua Qu, Wenzhuo Guo, and X. Peng. Experimental determination of the extinction coefficient of CdTe, CdSe, and CdS nanocrystals. *Chemistry of Materials*, 15(14):2854–2860, 2003.

[27] Celso de Mello Donegá and Rolf Koole. Size dependence of the spontaneous emission rate and absorption cross section of CdSe and CdTe quantum dots. *The Journal of Physical Chemistry C*, 113(16):6511–6520, 2009.

[28] Wanli Ma, Sarah L Swisher, Trevor Ewers, Jesse Engel, Vivian E Ferry, Harry a Atwater, and a Paul Alivisatos. Photovoltaic performance of ultrasmall PbSe quantum dots. *ACS Nano*, 5(10):8140–7, October 2011.

[29] A. Sashchiuk, L. Langof, R. Chaim, and E. Lifshitz. Synthesis and characterization of PbSe and PbSe/PbS core-shell colloidal nanocrystals. *Journal of Crystal Growth*, 240:431–438, 2002.

[30] A. Lipovskii, E. Kolobkova, V.D. Petrikov, I. Kang, A. Olkhovets, T. Krauss, M. Thomas, J. Sicox, F. Wise, Q. Shen, and S. Kycia. Synthesis and characterization of PbSe quantum dots in phosphate glass. *Applied Physics Letters*, 71:3406, 1997.

[31] Iwan Moreels, Karel Lambert, David De Muynck, Frank Vanhaecke, Dirk Poelman, José C. Martins, Guy Allan, and Zeger Hens. Composition and Size-Dependent Extinction Coefficient of Colloidal PbSe Quantum Dots. *Chemistry of Materials*, 19(25):6101–6106, December 2007.

[32] Doris Segets, J. Matthew Lucas, Robin N. Klupp Taylor, Marcus Scheele, Zheng Haimei, A. Paul Alivisatos, and Wolfgang Peukert. Determination of the Quantum Dot Band Gap Dependence on Particle Size from Optical Absorbance and Transmission Electron Microscopy Measurements. *ACS Nano*, 6:9021–9032, 2012.

[33] Tobias Hanrath, Dirk Veldman, Joshua J. Choi, Christina G. Christova, Martijn M. Wienk, and René A. J. Janssen. PbSe nanocrystal network formation during pyridine ligand displacement. *ACS applied materials & interfaces*, 1(2):244–50, February 2009.

[34] G. Allan, C. Delerue, and Y. Niquet. Luminescence polarization of silicon nanocrystals. *Physical Review B*, 63(20):205301, April 2001.

[35] Milan Sykora, Alexey Y Koposov, John a McGuire, Roland K Schulze, Olexandr Tretiak, Jeffrey M Pietryga, and Victor I Klimov. Effect of air exposure on surface properties, electronic structure, and carrier relaxation in PbSe nanocrystals. *ACS Nano*, 4(4):2021–34, April 2010.

[36] Assaf Aharoni, Taleb Mokari, Inna Popov, and Uri Banin. Synthesis of InAs/CdSe/ZnSe core/shell1/shell2 structures with bright and stable near-infrared fluorescence. *Journal of the American Chemical Society*, 128(1):257–64, January 2006.

[37] Jeffrey M Pietryga, Richard D Schaller, Donald Werder, Michael H Stewart, Victor I Klimov, and Jennifer a Hollingsworth. Pushing the band gap envelope: mid-infrared emitting colloidal PbSe quantum dots. *Journal of the American Chemical Society*, 126(38):11752–3, September 2004.

[38] Jeffrey M. Pietryga, Donald J. Werder, Darrick J. Williams, Joanna L. Casson, Richard D. Schaller, Victor I. Klimov, and Jennifer A. Hollingsworth. Utilizing the lability of lead selenide to produce heterostructured nanocrystals with bright, stable infrared emission. *Journal of the American Chemical Society*, 130(14):4879–85, April 2008.

[39] Keith A. Abel, Haijun Qiao, Jeff F. Young, and Frank C. J. M. van Veggel. Four-Fold Enhancement of the Activation Energy for Nonradiative Decay of Excitons in PbSe/CdSe Core/Shell versus PbSe Colloidal Quantum Dots. *The Journal of Physical Chemistry Letters*, 1(15):2334–2338, August 2010.

[40] Yu Zhang, Quanqin Dai, Xinbi Li, Qingzhou Cui, Zhiyong Gu, Bo Zou, Yiding Wang, and William W. Yu. Formation of PbSe/CdSe Core/Shell Nanocrystals for Stable Near-Infrared High Photoluminescence Emission. *Nanoscale Research Letters*, 5(8):1279–1283, June 2010.

[41] W. Heiss, H. Groiss, E. Kaufmann, G. Hesser, M. Boberl, G. Springholz, F. Schaffler, K. Koike, H. Harada, and M. Yano. Centrosymmetric PbTeCdTe quantum dots coherently embedded by epitaxial precipitation. *Applied Physics Letters*, 88(19):192109, 2006.

[42] W. Heiss, E. Kaufmann, M. Böberl, T. Schwarzl, G. Springholz, G. Hesser, F. Schäffler, K. Koike, H. Harada, M. Yano, R. Leitsmann, L.E. Ramos, and F. Bechstedt. Highly luminescent nanocrystal quantum dots fabricated by lattice-type mismatched epitaxy. *Physica E: Low-dimensional Systems and Nanostructures*, 35(2):241–245, December 2006.

[43] Dominika Grodziska, Francesca Pietra, Marijn A. van Huis, Daniel Vanmaekelbergh, and Celso de Mello Donegá. Thermally induced atomic reconstruction of PbSe/CdSe core/shell quantum dots into PbSe/CdSe bi-hemisphere hetero-nanocrystals. *Journal of Materials Chemistry*, 21(31):11556, 2011.

[44] Ingmar Swart, Zhixiang Sun, Daniël Vanmaekelbergh, and Peter Liljeroth. Hole-induced electron transport through core-shell quantum dots: a direct measurement of the electron-hole interaction. *Nano Letters*, 10(5):1931–5, May 2010.

[45] Karel Lambert, Bram De Geyter, Iwan Moreels, and Zeger Hens. PbTe— CdTe core—shell particles by cation exchange, a HR-TEM study. *Chemistry of Materials*, 21:778–780, 2009.

[46] R. Leitsmann, L. Ramos, and F. Bechstedt. Structural properties of PbTeCdTe interfaces from first principles. *Physical Review B*, 74(8):1–8, August 2006.

[47] R. Leitsmann and F Bechstedt. Ab initio characterization of the electronic properties of PbTe quantum dots embedded in a CdTe matrix. *Semiconductor Science and Technology*, 26(1):014005, January 2011.

[48] Sara Bals, Marianna Casavola, Marijn A. van Huis, Sandra Van Aert, K. Joost Batenburg, Gustaaf Van Tendeloo, and Daniël Vanmaekelbergh. Three-dimensional atomic imaging of colloidal core-shell nanocrystals. *Nano Letters*, 11(8):3420–4, August 2011.

[49] Bram De Geyter, Yolanda Justo, Iwan Moreels, Karel Lambert, Philippe F. Smet, Dries Van Thourhout, Arjan J. Houtepen, Dominika Grodziska, Celso de Mello Donegá, Andries Meijerink, Daniel Vanmaekelbergh, and Zeger Hens. The different nature of band edge absorption and emission in colloidal PbSe/CdSe core/shell quantum dots. *ACS Nano*, 5(1):58–66, January 2011.

[50] Al Efros, M Rosen, M Kuno, M Nirmal, Dj Norris, and M Bawendi. Band-edge exciton in quantum dots of semiconductors with a degenerate valence band: Dark and bright exciton states. *Physical Review B*, 54(7):4843–4856, August 1996.

[51] H. H. von Grünberg. Energy levels of CdSe quantum dots: Wurtzite versus zinc-blende structure. *Physical Review B*, 55(4):2293–2302, January 1997.

[52] B. Zorman, M. V. Ramakrishna, and R. a. Friesner. Quantum Confinement Effects in CdSe Quantum Dots. *The Journal of Physical Chemistry*, 99(19):7649–7653, May 1995.

[53] Antonietta Tomasulo and Mushti V. Ramakrishna. Quantum confinement effects in semiconductor clusters. II. *The Journal of Chemical Physics*, 105(9):3612, 1996.

[54] Akiko Kobayashi, Otto F. Sankey, Stephen M. Volz, and John D. Dow. Semiempirical tight-binding band structures of wurtzite semiconductors: AlN, CdS, CdSe, ZnS, and ZnO. *Physical Review B*, 28(2):935, 1983.

[55] Denis Bertho, Jean-Marc Jancu, and Christian Jouanin. [001] strain-induced band mixing in zinc-blende semiconductors: Intravalence versus upper-conduction-valence band effects. *Physical Review B*, 50(23):16956, 1994.

[56] D Olguin and R Baquero. (001)-surface-induced bulk states and surface resonances in II-VI zinc-blende semiconductors. *Physical Review B*, 51(23):891–897, 1995.

[57] Nacir Tit and Ihab M Obaidat. Charge confinements in CdSeZnSe symmetric double quantum wells. *Journal of Physics: Condensed Matter*, 20(16):165205, April 2008.

[58] Jianxiao Si, Shuqiang Jin, Hanjie Zhang, Ping Zhu, Dongjiang Qiu, and Huizhen Wu. Experimental determination of valence band offset at PbTe/CdTe(111) heterojunction interface by x-ray photoelectron spectroscopy. *Applied Physics Letters*, 93(20):202101, 2008.

[59] Magorzata Bukaa, Piotr Sankowski, Ryszard Buczko, and Pera Kacman. Crystal and electronic structure of PbTe/CdTe nanostructures. *Nanoscale research Letters*, 6(1):126, January 2011.

[60] R. Leitsmann, F. Bechstedt, H. Groiss, F. Schäffler, W. Heiss, K. Koike, H. Harada, and M. Yano. Structural and electronic properties of PbTe (rocksalt)/CdTe (zinc-blende) interfaces. *Applied Surface Science*, 254(1):397–400, October 2007.

[61] R. Leitsmann and F. Bechstedt. Electronic-structure calculations for polar lattice-structure-mismatched interfaces: PbTeCdTe(100). *Physical Review B*, 76(12):1–11, September 2007.

[62] Yann-Michel Niquet and Christophe Delerue. Band offsets, wells, and barriers at nanoscale semiconductor heterojunctions. *Physical Review B*, 84(7):075478, August 2011.

[63] M. Schlüter, G. Martinez, and M. L. Cohen. Electronic charge densities in PbSe and PbTe. *Physical Review B*, 11(10):3808, 1975.

[64] G. Allan. Surface core-level shifts and relaxation of group-IV A-element chalcogenide semiconductors. *Physical Review B*, 43(12):9594–9598, 1991.

[65] T. Nguyen, J. Habinshuti, Y. Justo, R. Gomes, G. Mahieu, S. Godey, J. Nys, S. Carrillo, Z. Hens, O. Robbe, S. Turrell, and B. Grandidier. Charge carrier identification in tunneling spectroscopy of core-shell nanocrystals. *Physical Review B*, 84(19):1–8, November 2011.

[66] Jean-Marc Jancu, Reinhard Scholz, Fabio Beltram, and Franco Bassani. Empirical *spds** tight–binding calculation for cubic semiconductors: General method and material parameters. *Physical Review B*, 57(11):6493–6507, March 1998.

[67] Bram De Geyter, Arjan J. Houtepen, Sergio Carrillo, Pieter Geiregat, Yunan Gao, Sybren Ten Cate, Juleon M. Schins, Dries Van Thourhout, Christophe Delerue, Laurens D. A. Siebbeles, and Zeger Hens. Broadband and picosecond intraband absorption in lead-based colloidal quantum dots. *ACS Nano*, 6(7):6067–74, July 2012.

[68] V. I. Klimov and D W McBranch. Femtosecond high-sensitivity, chirp-free transient absorption spectroscopy using kilohertz lasers. *Optics Letters*, 23(4):277–9, February 1998.

[69] V. I. Klimov, D. W. McBranch, C. A. Leatherdale, and M. G. Bawendi. Electron and hole relaxation pathways in semiconductor quantum dots. *Physical Review B*, 60(19):13740, 1999.

[70] Alexander A. Mikhailovsky, Su Xu, and Victor I. Klimov. Femtosecond intraband modulation spectroscopy. *Review of Scientific Instruments*, 73(1):136, 2002.

[71] A. I. Ekimov, F. Hache, M. C. Schanne-Klein, D. Ricard, C. Flytzanis, I. A. Kudryavtsev, T. V. Yazeva, A. V. Rodina, and A. L. Efros. Absorption and intensity-dependent photoluminescence measurements on CdSe quantum dots: assignment of the first electronic transitions. *Journal of the Optical Society of America B*, 10(1):100–107, January 1993.

[72] Anshu Pandey and Philippe Guyot-Sionnest. Intraband spectroscopy and band offsets of colloidal II-VI core/shell structures. *The Journal of Chemical Physics*, 127(10):104710, September 2007.

[73] S. Schmitt-Rink, D. A. B. Miller, and D. S. Chemla. Theory of the linear and nonlinear optical properties of semiconductor microcrystallites. *Physical Review B*, 35(15):8113, 1987.

[74] A. Germeau, A. Roest, D. Vanmaekelbergh, G. Allan, C. Delerue, and E. Meulenkamp. Optical Transitions in Artificial Few-Electron Atoms Strongly Confined inside ZnO Nanocrystals. *Physical Review Letters*, 90(9):7–10, March 2003.

[75] J. M. An, A. Franceschetti, and A. Zunger. The Excitonic Exchange Splitting and Radiative Lifetime in PbSe Quantum Dots. *Nano Letters*, 7(7):2129–2135, July 2007.

[76] J. M. An, A. Franceschetti, and Alex Zunger. Pauli blocking versus electrostatic attenuation of optical transition intensities in charged PbSe quantum dots. *Physical Review B*, 76(16):1–4, October 2007.

[77] J. M. An, A. Franceschetti, and A. Zunger. Electron and hole addition energies in PbSe quantum dots. *Physical Review B*, 76(4):1–7, July 2007.

[78] M Tuan Trinh, Arjan J. Houtepen, Juleon M. Schins, Jorge Piris, and Laurens D. A. Siebbeles. Nature of the second optical transition in PbSe nanocrystals. *Nano Letters*, 8(7):2112–7, July 2008.

[79] Juleon Schins, M. Trinh, Arjan J. Houtepen, and Laurens Siebbeles. Probing formally forbidden optical transitions in PbSe nanocrystals by time- and energy-resolved transient absorption spectroscopy. *Physical Review B*, 80(3):8–13, July 2009.

[80] Jeffrey Harbold and Frank Wise. Photoluminescence spectroscopy of PbSe nanocrystals. *Physical Review B*, 76(12):1–6, September 2007.

[81] Brian L. Wehrenberg, Congjun Wang, and Philippe Guyot-Sionnest. Interband and Intraband Optical Studies of PbSe Colloidal Quantum Dots. *The Journal of Physical Chemistry B*, 106(41):10634–10640, October 2002.

[82] Timothy J. Pennycook, James R. McBride, Sandra J. Rosenthal, Stephen J. Pennycook, and Sokrates T. Pantelides. Dynamic fluctuations in ultrasmall nanocrystals induce white light emission. *Nano Letters*, 12(6):3038–42, June 2012.

[83] Yasuaki Masumoto and Fumio Sasaki. Intraband energy relaxation of hot carriers in CdSe. *Journal of Luminescence*, 48:189–192, 1991.

[84] L.M. Ramaniah and S.V. Nair. Optical absorption in semiconductor quantum dots: A tight-binding approach. *Physical Review B*, 47(12):7132, 1993.

[85] D. J. Norris, A. Sacra, C. B. Murray, and M. G. Bawendi. Measurement of the size dependent hole spectrum in CdSe quantum dots. *Physical Review Letters*, 72(16):2612–2615, 1994.

[86] D. J. Norris and M. G. Bawendi. Measurement and assignment of the size-dependent optical spectrum in CdSe quantum dots. *Physical Review B*, 53(24):16338–16346, June 1996.

[87] Dj Norris, Al Efros, M Rosen, and Mg Bawendi. Size dependence of exciton fine structure in CdSe quantum dots. *Physical Review B*, 53(24):16347–16354, June 1996.

[88] M Chamarro, C Gourdon, P Lavallard, O Lublinskaya, and A. I. Ekimov. Enhancement of electron-hole exchange interaction in CdSe nanocrystals: A quantum confinement effect. *Physical Review B*, 53(3):1336, 1996.

[89] P. Guyot-Sionnest and M. a. Hines. Intraband transitions in semiconductor nanocrystals. *Applied Physics Letters*, 72(6):686, 1998.

[90] Alex Zunger. High-Energy Excitonic Transitions in CdSe Quantum Dots. *The Journal of Physical Chemistry B*, 102(34):6449–6454, August 1998.

[91] V. Klimov, Ch. Schwarz, D. McBranch, C. Leatherdale, and M. Bawendi. Ultrafast dynamics of inter- and intraband transitions in semiconductor nanocrystals: Implications for quantum-dot lasers. *Physical Review B*, 60(4):R2177–R2180, July 1999.

[92] V. I. Klimov. Quantization of Multiparticle Auger Rates in Semiconductor Quantum Dots. *Science*, 287(5455):1011–1013, February 2000.

[93] D. S. Ginger, A. S. Dhoot, C. E. Finlayson, and N. C. Greenham. Long-lived quantum-confined infrared transitions in CdSe nanocrystals. *Applied Physics Letters*, 77(18):2816, 2000.

[94] C Wang, M Shim, and P Guyot-Sionnest. Electrochromic nanocrystal quantum dots. *Science (New York, N.Y.)*, 291(5512):2390–2, March 2001.

[95] Moonsub Shim, Congjun Wang, and P. Guyot-Sionnest. Charge-tunable optical properties in colloidal semiconductor nanocrystals. *The Journal of Physical Chemistry B*, 105(12):2369–2373, 2001.

[96] Clemens Burda, Stephan Link, Mona Mohamed, and M. El-Sayed. The relaxation pathways of CdSe nanoparticles monitored with femtosecond time-resolution from the visible to the IR: Assignment of the transient features by carrier quenching. *The Journal of Physical Chemistry B*, 105(49):12286–12292, 2001.

[97] Jesús Pérez-Conde and A. K. Bhattacharjee. Exciton states and optical properties of CdSe nanocrystals. *Physical Review B*, 63(24):1–9, June 2001.

[98] Roger Sakhel, Lars Jönsson, and John W. Wilkins. Far-infrared-driven electron-hole correlations in a quantum dot with an internal tunneling barrier. *Physical Review B*, 64(15):155322, September 2001.

[99] S. Xu, A. A. Mikhailovsky, J. A. Hollingsworth, and V. I. Klimov. Hole intraband relaxation in strongly confined quantum dots: Revisiting the phonon bottleneck problem. *Physical Review B*, 65(4):045319, 2002.

[100] Pingrong Yu, J. M. Nedeljkovic, P. A. Ahrenkiel, R. J. Ellingson, and A. J. Nozik. Size dependent femtosecond electron cooling dynamics in CdSe quantum rods. *Nano Letters*, 4(6):1089–1092, 2004.

[101] D Tonti, F. Van Mourik, and M Chergui. On the excitation wavelength dependence of the luminescence yield of colloidal CdSe quantum dots. *Nano Letters*, 4(12):2483–2487, 2004.

[102] A. W. Schill, C. S. Gaddis, Wei Qian, M.A. El-Sayed, Ye Cai, V. T. Milam, and Kenneth Sandhage. Ultrafast electronic relaxation and charge-carrier localization in CdS/CdSe/CdS quantum-dot quantum-well heterostructures. *Nano Letters*, 6(9):1940–1949, 2006.

[103] Yingli Qu, Wei Ji, Yuangang Zheng, and Jackie Y. Ying. Auger recombination and intraband absorption of two-photon-excited carriers in colloidal CdSe quantum dots. *Applied Physics Letters*, 90(13):133112, 2007.

[104] Jier Huang, Zhuangqun Huang, Shengye Jin, and Tianquan Lian. Exciton Dissociation in CdSe Quantum Dots by Hole Transfer to Phenothiazine. *The Journal of Physical Chemistry C*, 112(49):19734–19738, December 2008.

[105] Frank Van Mourik, Gérard Giraud, Dino Tonti, Majed Chergui, and Gert Van der Zwan. Linear dichroism of CdSe nanodots: Large anisotropy of the band-gap absorption induced by ground-state dipole moments. *Physical Review B*, 77(16):165303, April 2008.

[106] Florian Sotier, Tim Thomay, Tobias Hanke, Jan Korger, Suddhasatta Mahapatra, Alexander Frey, Karl Brunner, Rudolf Bratschitsch, and Alfred Leitenstorfer. Femtosecond few-fermion dynamics and deterministic single-photon gain in a quantum dot. *Nature Physics*, 5(5):352–356, 2009.

[107] Marco Califano. Electron Relaxation Following UV Excitation in CdSe Nanocrystals: Sub-Picosecond-Fast Population of the 1 P States Across a Gap Wider Than 10 Phonon Energies. *The Journal of Physical Chemistry C*, 113:19859–19862, 2009.

[108] K. Lantz and A. D. Stiff-Roberts. Calculation of Intraband Absorption Coefficients in Organic/Inorganic Nanocomposites: Effects of Colloidal Quantum Dot Surface Ligand and Dot Size. *IEEE Journal of Quantum Electronics*, 47(99):1420–1427, 2011.

[109] M. G. Bawendi, P. J. Carroll, William L. Wilson, and L. E. Brus. Luminescence properties of CdSe quantum crystallites: Resonance between interior and surface localized states. *The Journal of Chemical Physics*, 96(2):946, 1992.

[110] L. Biadala, Y. Louyer, Ph. Tamarat, and B. Lounis. Direct Observation of the Two Lowest Exciton Zero-Phonon Lines in Single CdSe/ZnS Nanocrystals. *Physical Review Letters*, 103(3):1–4, July 2009.

[111] Bram De Geyter and Zeger Hens. The absorption coefficient of PbSe/CdSe core/shell colloidal quantum dots. *Applied Physics Letters*, 97(16):161908, 2010.

[112] A. E. Neeves and M. H. Birnboim. Composite structures for the enhancement of nonlinear-optical susceptibility. *Journal of the Optical Society of America B*, 6(4):787–796, 1989.